

2009

Sidewall profiles and etching mechanisms in an inductively coupled plasma for silicon, silicon dioxide and lithium niobate

Lirong Sun
University of Dayton

Follow this and additional works at: https://ecommons.udayton.edu/graduate_theses

Recommended Citation

Sun, Lirong, "Sidewall profiles and etching mechanisms in an inductively coupled plasma for silicon, silicon dioxide and lithium niobate" (2009). *Graduate Theses and Dissertations*. 5866.
https://ecommons.udayton.edu/graduate_theses/5866

This Dissertation is brought to you for free and open access by the Theses and Dissertations at eCommons. It has been accepted for inclusion in Graduate Theses and Dissertations by an authorized administrator of eCommons. For more information, please contact mschlange1@udayton.edu, ecommons@udayton.edu.

SIDEWALL PROFILES AND ETCHING MECHANISMS IN AN INDUCTIVELY
COUPLED PLASMA FOR SILICON, SILICON DIOXIDE AND LITHIUM NIOBATE

Dissertation

Submitted to

The School of Engineering of the

UNIVERSITY OF DAYTON

in Partial Fulfillment of the Requirements for

The Degree

Doctor of Philosophy in Electro-Optics

By

Lirong Sun

UNIVERSITY OF DAYTON

Dayton, Ohio

December, 2009

SIDEWALL PROFILES AND ETCHING MECHANISMS IN AN INDUCTIVELY
COUPLED PLASMA FOR SILICON, SILICON DIOXIDE AND LITHIUM NIOBATE

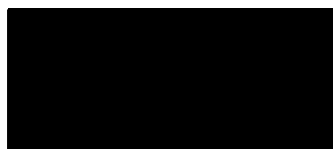
APPROVED BY:



Andrew M. Sarangan, Ph.D.
Associate Professor,
Electro-Optics Program
Committee Chairman



Joseph W. Haus, Ph.D.
Director and Professor,
Electro-Optics Program
Committee Member



Qiwen Zhan, Ph.D.
Associate Professor,
Electro-Optics Program
Committee Member



Guru Subramanyam, Ph.D.
Professor,
Department of Electrical and
Computer Engineering
Committee Member



Malcolm W. Daniels, Ph.D.
Associate Dean,
School of Engineering



Tony E. Saliba, Ph.D.
Dean, School of Engineering

ABSTRACT

SIDEWALL PROFILES AND ETCHING MECHANISMS IN AN INDUCTIVELY COUPLED PLASMA FOR SILICON, SILICON DIOXIDE AND LITHIUM NIOBATE

Name: Sun, Lirong
University of Dayton

Advisor: Dr. Andrew M. Sarangan

Current work on deep-RIE etching has been primarily focused on creating vertical sidewalls for MEMS and electronics applications. For micro-optical and MOEM structures, control of the sidewall angles other than vertical is as important as the ultimate depth. In this dissertation, we investigate the mechanisms of sidewall profile control using an inductively coupled plasma (ICP) reactor. The material systems being investigated are silicon, silicon dioxide and Lithium Niobate. Test structures are created by photolithography and different chemistries such as CF_4 , CF_4/Ar , CF_4/O_2 , CHF_3 , SF_6 and SF_6/O_2 have been explored to achieve a wide range of etch rates, etch profiles, sidewall angles, and surface roughness. The FDTD method is developed for the simulation and the analysis of V-grooved micro-optic designs. This research also includes the statistical experimental fractional factorial design for controlling the sidewall profiles by adjusting processing gas composition, the ICP power, processing pressure, bias power and etching time. The etch profiles are characterized by scanning electron microscopy (SEM), atomic force microscopy (AFM) and white light interferometer (WLI).

ACKNOWLEDGEMENTS

First, I praise and thank God for pouring his everlasting love and abundant blessing on me and for giving me strength.

This dissertation would not have been possible without the help from many people whom I would like to take this opportunity to thank here. First of all, I am greatly indebted to my advisor, Dr. Andrew M. Sarangan, and would like to acknowledge and thank him for his excellent advice and discussions during my PhD research. It has been my privilege to study under his guidance not only because he is a leading scientist in the fields of semiconductor, optoelectronics and nanofabrication technology, but also he is a kind and generous person and willing to teach and share his knowledge and experience. I have had this great experience and pleasure to work in his nanofabrication lab which he established over the past years. In addition, I would like thank him for arranging and taking us students to visit other universities, research labs and companies by his extra and valuable time. Those trips and experiences greatly benefit me and broad my mind.

I am grateful to my friend Dr. Yiyi Guan, who was a previous Electro-Optics Ph.D graduate. I thank her for encouraging and introducing me to this Electro-Optics Ph.D program.

I would like to thank my committees, Dr. Joseph W. Haus, who is the director of Electro-Optics Program for leading this fantastic Electro-Optics Program and providing a pleasant, great academic and research atmosphere, Dr. Qiwen Zhan for allowing me use the atomic force microscope and white light interferometer in his lab, and Dr. Guru Subramanyam, for all their continuous help and valuable advice throughout my study from dissertation proposal to defense.

I thank our group members for the past 5 years, Cijy E. Sunny, Dr. Jang Pyo Kim, Dr. Aziz Mahfoud Familia, Dr. Agus Widjaja, Mengshu Pan, Emily Fehrma, Benjamin Booso and Zhi Wu for their help and collaboration. It has been a great pleasure for working with all of them.

I would like to thank Weibin Chen for helping me with obtaining images from atomic force microscopy and White Light Interferometer.

I would like to thank all of the professors at the University of Dayton who taught me during my study. Furthermore, I would like to thank Nancy Wilson for her many help, assistance and support. Many thanks are due to Scott Streib for his help in NEST lab.

I would like to thank John Devitt, Dr. Phillip Henry and Dr. Mike Garter for their discussions, help and collaboration while I was working on the micro-optics project with them at L3-CE at Mason, Ohio.

I would like to thank Vincent Stenger from Srico for providing the patterned LiNbO_3 gratings and LiNbO_3 ridge waveguide samples.

I thank the Dayton Area Graduate Studies Institute (DAGSI) for providing me a financial scholarship from 2005 to 2008.

I would like to take this opportunity to thank my family. I am grateful to my parents, my sisters and brother for their love and patience and for having confident in me. I am grateful to my precious son Aaron and daughter Sarah for having brought so much love and joy to my life. Last but not least, I am grateful to my husband Frank Zhao, without his love, patience, sacrifice, fully support and constant encouragement, this work is impossible to finish.

TABLE OF CONTENTS

| | |
|---|--------------|
| ABSTRACT..... | iii |
| ACKNOWLEDGEMENTS..... | iv |
| LIST OF FIGURES..... | xi |
| LIST OF TABLES..... | xviii |
| CHAPTER | |
| I. INTRODUCTION..... | 1 |
| II. REVIEW OF RELATED RESEARCH | 3 |
| 2.1 Material Properties and Applications | 3 |
| 2.1.1 Silicon and Silicon Dioxide | 3 |
| 2.1.2 Lithium Niobate | 4 |
| 2.2 Etching Mechanisms | 4 |
| 2.3 Wet Etching | 5 |
| 2.4 Plasma (dry) Etching | 6 |
| 2.4.1 Ion Sputtering | 8 |
| 2.4.2 Chemical Etching | 8 |
| 2.4.3 Ion-enhanced Etching | 9 |
| 2.4.4 Ion-enhanced Protective-passivation | 9 |
| 2.5 Reactive Ion Etch (RIE) System | 9 |

| | | |
|--|--|-----------|
| 2.6 | ICP System | 10 |
| 2.7 | Fluorocarbon Plasma | 11 |
| 2.8 | Sidewall Profile | 13 |
| 2.8.1 | Mask Erosion | 14 |
| 2.8.2 | Balanced Polymer Deposition and Polymer Etch | 15 |
| 2.8.3 | Redeposition | 15 |
| III. V-GROOVED MICRO-OPTIC DESIGN AND FDTD SIMULATION..... | | 16 |
| 3.1 | Fill Factor | 17 |
| 3.2 | V-grooved Micro-Optic Design | 18 |
| 3.3 | The 3D Finite-Difference Beam Propagation Method | 19 |
| 3.4 | The Finite Difference Time Domain (FDTD) Simulations | 22 |
| IV. MICRO-OPTIC FABRICATION STEPS | | 29 |
| 4.1 | Mask Fabrications..... | 29 |
| 4.1.1 | Photoresist as the Etch Mask | 29 |
| 4.1.2 | Fabrication of Al ₂ O ₃ and Cr as Masks..... | 30 |
| 4.1.3 | Electron Beam Evaporation | 32 |
| 4.2 | Etching | 33 |
| V. INDUCTIVELY COUPLED PLASMA ETCHING TECHNIQUES AND RESULTS..... | | 34 |
| 5.1 | Introduction..... | 34 |
| 5.2 | ICP Etching of a Blank Silicon Wafer | 37 |
| 5.2.1 | RIE Bias Power. | 38 |
| 5.2.2 | Pressure | 45 |

| | |
|--|-----------|
| 5.2.3 ICP Source Power | 46 |
| 5.2.4 Substrate Temperature | 47 |
| 5.2.5 Conclusion | 48 |
| 5.3 ICP Etching of Micro-Optic Structures | 49 |
| 5.3.1 RIE Bias Power. | 49 |
| 5.3.2 Etching Time | 52 |
| 5.3.3 Ratio of Gas Flow Rates | 53 |
| 5.3.4 Pressure | 54 |
| 5.3.5 ICP Source Power | 55 |
| 5.4 Selectivity of Silicon Over Mask Materials | 55 |
| 5.5 Bosch Process | 57 |
| 5.6 Conclusions..... | 61 |
| VI. LITHIUM NIOBATE ICP ETCHING..... | 62 |
| 6.1 ICP Etching of a Blank LiNbO ₃ Wafer | 62 |
| 6.2 ICP Etching of LiNbO ₃ Gratings | 65 |
| 6.3 ICP Etching of LiNbO ₃ Ridge Waveguides | 70 |
| 6.4 Conclusions | 72 |
| VII. EXPERIMENTAL DESIGN AND MODELS..... | 73 |
| 7.1 Experimental Design..... | 73 |
| 7.2 Silicon Etch Rate | 74 |
| 7.3 The Sidewall Angle | 75 |
| 7.4 Conclusion..... | 78 |
| VIII. CONCLUSIONS | 79 |

| | |
|--|-----------|
| APPENDIX CHARACTERIZATION TECHNIQUES | 80 |
| A.1 Stylus Interferometer | 80 |
| A.2 High Resolution Scanning Electron Microscope | 81 |
| A.3 Atomic Force Microscope | 82 |
| A.4 White Light Interferometer | 83 |
| BIBLIOGRAPHY..... | 84 |
| VITA..... | 91 |

LIST OF FIGURES

| | |
|--|----|
| Figure 2.1: Silicon (100) 60% KOH wet etch (a) 20 minutes (b) 30 minutes at temperature 75C | 5 |
| Figure 2.2: Ions and neutrals react with the mask and the substrate | 14 |
| Figure 2.3: (a) Ideal straight wall etch, no lateral etch, (b) isotropic etch with undercut, (c) mask erosion, steady-state sidewall angle with decreased linewidth (d) eroded mask redeposition (e) sputtered product redeposition with increase linewidth | 15 |
| Figure 3.1: Schematic of IR FPA (Ref. 51) | 17 |
| Figure 3.2: Micro-lenses on a reticulated FPA..... | 17 |
| Figure 3.3: Fill factor of the focal plane array..... | 17 |
| Figure 3.4: Micro-Optic structures on a reticulated FPA..... | 18 |
| Figure 3.5: The cross-sectional view of the micro-optic geometry used for a numerical simulation..... | 20 |
| Figure 3.6: The notch structure, the field distribution and the field intensity plot at the detector | 20 |
| Figure 3.7: The BPM simulations | 22 |
| Figure 3.8: Comparison of BPM and FDTD Simulations..... | 23 |

| | |
|--|----|
| Figure 3.9: The FDTD simulations (a) $w = 2\mu\text{m}$ and (b) $w = 5\mu\text{m}$ at 54° . | 24 |
| Figure 3.10: The FDTD simulation of $w = 5\mu\text{m}$ and $\theta = 80^\circ$. | 25 |
| Figure 3.11: The reflectance and the fill factor as functions of the width w at the different wavelengths and the notch angles. | 27 |
| Figure 4.1: (a) Fabrication of Photoresist as a mask and (b) Fabrication of Al_2O_3 or Cr as a mask by a lift-off process | 30 |
| Figure 4.2: LOR thickness vs. Spin speed (Ref. 52). | 31 |
| Figure 4.3: SPR955-CM thickness vs. Spin speed (Ref. 53). | 31 |
| Figure 4.4: The SEM cross-sectional view of Cr mask by E-Beam Evaporation. | 31 |
| Figure 4.5: Torr Electron beam evaporation system. | 33 |
| Figure 5.1: (a) Unaxis ICP Shuttleline in our nanofabrication lab and (b) Schematic drawing of ICP. | 35 |
| Figure 5.2: ICP Diagram. | 36 |
| Figure 5.3: Turbo pump (Ref. 50). | 36 |
| Figure 5.4: The etch rates (left) and DC bias voltage (right) of Si $\langle 100 \rangle$ and $\langle 111 \rangle$, SiO_2 as functions of RIE bias power in SF_6 plasma. | 38 |
| Figure 5.5: The etch rate (left) of Si and SiO_2 and the selectivity (right) of Si over SiO_2 as functions of the RIE bias power in SF_6 plasma. | 39 |
| Figure 5.6: The etch rates (left) and DC bias voltage (right) of Si $\langle 100 \rangle$, $\langle 111 \rangle$ and SiO_2 as functions of RIE bias power in CF_4 plasma. | 40 |
| Figure 5.7: The selectivity (right) of Si over SiO_2 as a function of RIE bias power in CF_4 plasma. | 41 |

| | |
|--|----|
| Figure 5.8: The etch rates (left) and DC bias voltage (right) of Si <100> as functions of RIE bias power in CHF ₃ plasma | 42 |
| Figure 5.9: The selectivity (right) of Si over SiO ₂ as a function of RIE bias power in CHF ₃ plasma. | 42 |
| Figure 5.10: The etch rates (left) and DC bias voltage (right) of Si <100> in CHF ₃ and in CF ₄ plasma as functions of RIE bias power..... | 43 |
| Figure 5.11: DC bias voltages of different substrates in each of SF ₆ , CF ₄ and argon plasma as functions of RIE bias power. | 44 |
| Figure 5.12: The etch rate (left) and DC bias voltages (right) of Si in CHF ₃ plasma as a function of the operating pressure. | 45 |
| Figure 5.13: The etch rate (left) and DC bias voltage (right) of Si in SF ₆ plasma as a function of ICP source power. | 46 |
| Figure 5.14: The etch rate (left) and DC bias voltage (right) of Si in CHF ₃ plasma as a function of ICP source power. | 47 |
| Figure 5.15: The etch rate (left) and DC bias voltage (right) of Si in CHF ₃ plasma as a function of the substrate temperature. | 47 |
| Figure 5.16: The polymer deposition rate on Si substrate in CHF ₃ plasma as a function of the substrate temperature. | 48 |
| Figure 5.17: The Si etch rate (left) and the sidewall angle in CHF ₃ plasma as a function of the RIE power. | 49 |
| Figure 5.18: The Si etch rate (left) and the sidewall angle in CF ₄ /Ar plasma as a function of the RIE power. | 50 |

| | |
|--|----|
| Figure 5.19: The cross-sectional view of etched micro-optic structures at (a) 5mTorr, RIE 200W (b) 15 mTorr, 200W and (c) 15mTorr, RIE 50W | 51 |
| Figure 5.20: The cross-sectional view of etched micro-optic structure at 5mTorr with (a) RIE ramping up from 50W to 200W and (b) RIE ramping down from 200W to 50W | 52 |
| Figure 5.21: Micro-Optic V-groove structures | 52 |
| Figure 5.22: The Si etch rate (left) and the sidewall angle in CF ₄ /Ar 10/50 plasma as a function of the etching time. | 53 |
| Figure 5.23: The Si etch rate (left) and the sidewall angle in CF ₄ /Ar plasma as a function of the ratio of CF ₄ flow rate over Argon flow rate. | 53 |
| Figure 5.24: The Si etch rate (left) and the sidewall angle (right) in CHF ₃ plasma as a function of the operating pressure. | 54 |
| Figure 5.25: The Si etch rate (left) and the sidewall angle in CF ₄ /Ar 5/50 plasma as a function of the ICP power. | 55 |
| Figure 5.26: (a) The Si etch rates, (b) the etch rate of mask materials and (c) the selectivity of Si over the mask materials as a function of the RIE power | 56 |
| Figure 5.27: Schematic diagram of Bosch process | 58 |
| Figure 5.28: The SEM photograph of (a) a top view and a cross-sectional view of an Al ₂ O ₃ mask with the thickness of 5000A | 58 |
| Figure 5.29: The SEM photograph of (a) a top view and (b) a cross-sectional view of a Cr mask with the thickness of 5500A | 58 |

| | |
|--|----|
| Figure 5.30: The SEM photograph of a cross-sectional view Bosch process run B1 with a SU8 mask..... | 59 |
| Figure 5.31: The SEM photograph of a top view and two cross-sectional views of Bosch process run B2 | 59 |
| Figure 5.32: The SEM photograph of a top view and two cross-sectional views of Bosch process run B3 with an Al ₂ O ₃ mask | 59 |
| Figure 5.33: The SEM photograph of a cross-sectional view of Bosch process run B4 with a Cr mask | 60 |
| Figure 5.34: The SEM photograph of a top view and a cross-sectional view of Bosch process run B5 with a Cr mask | 60 |
| Figure 5.35: The SEM photograph of a cross-sectional view of Bosch process run B6 with a PR mask | 60 |
| Figure 6.1: The etch rates of LiNbO ₃ as a function of RIE power in (a) CHF ₃ , at 15mTorr (b) SF ₆ at 5mTorr and (c) CF ₄ plasma at 5mTorr while the ICP power was set to 400 W | 63 |
| Figure 6.2: The etch rates of Si, SiO ₂ and LiNbO ₃ as a function of RIE power in CHF ₃ plasma while the ICP power was set to 400 W, and the operating pressure at 5mTorr | 64 |
| Figure 6.3: The etch rate (left) and DC bias voltage (right) of y-cut LiNbO ₃ as a function of ICP source power in SF ₆ plasma | 65 |
| Figure 6.4: The SEM photography of patterned photoresist on the substrate LiNbO ₃ before etching | 66 |

| | |
|---|----|
| Figure 6.5: Before the sample (run 1) was cleaned by acetone (a)SEM, after the sample was cleaned by acetone (b) AFM 3D and (c) AFM line profile, (d) WLI cross-sectional view, (e) WLI line profile and (f) line profile by Ambios stylus profiler | 67 |
| Figure 6.6: The sample (run 3) before PR removal (a) AFM 3D, (b) AFM line profile and (c) SEM. After PR removal (d) WLI 3D view, (e) WLI cross section view, (f) WLI line profile and (g) Ambios profiler | 67 |
| Figure 6.7: The sample (run 2) before PR removal (a) AFM (b) SEM (c) Profiler line profile, after PR removal (d) 3D by WLI, (e) WLI lineprofile and (f) line profile by Ambios profiler | 68 |
| Figure 6.8: The sample (run 4) before PR removal (a) AFM (b) SEM, and after PR removal (c) Profiler line profile | 69 |
| Figure 6.9: The sample (run 5) was etched with SF_6/CHF_3 before PR removal (a) SEM and (b) SEM, after PR removal by (c) White light interferometer | 69 |
| Figure 6.10: LiNbO_3 ridge waveguide (a) the SEM cross-sectional view and (b) the schematic graph of the ridge waveguide | 70 |
| Figure 6.11: The sidewall angle as a function of the nominal width of etched LiNbO_3 ridge waveguides | 71 |
| Figure 7.1: The predicted etch rate as function of RIE power and operating pressure (a) 3D and (b) contour plot | 75 |
| Figure 7.2: The predicted sidewall angle as functions of RIE power and operating pressure (a) 3D and (b) contour plot | 76 |

| | |
|---|----|
| Figure 7.3: The contour plots of the predicted etch rate (a) 15 mTorr and (b) 5 mTorr and the sidewall angle (c) 15 mTorr and (d) 5mTorr as functions of RIE power and etching time | 77 |
| Figure 7.4: The 3D plot of the predicted sidewall angle as functions of RIE power and etching time (a) 15mTorr and (b) 5mTorr | 77 |
| Figure A.1: Ambios Stylus Interferometer..... | 81 |
| Figure A.2: The Hitachi S-4800 HRSEM | 81 |
| Figure A.3: Park System NSOM..... | 82 |
| Figure A.4: Veeco Wyko NT9100 White Light Interferometer..... | 83 |

LIST OF TABLES

| | |
|--|----|
| Table 3.1: A relation between angle θ and α | 23 |
| Table 5.1: Processing parameters and the selectivity of Si over Masks | 57 |
| Table 5.2: Bosch processing parameters | 59 |
| Table 6.1: Processing parameters of LiNbO ₃ ICP etching | 66 |
| Table 6.2: The sidewall angle of ICP etching LiNbO ₃ ridge waveguides | 71 |
| Table 7.1: The coefficients of the equation | 74 |
| Table 7.2: The coefficients of the equation (7-3)..... | 75 |

CHAPTER I

INTRODUCTION

For the realization of micro- and nano-optical structures that employ reflective surfaces, the control of the sidewall profiles other than vertical is as important as the depth. Fluorocarbon plasma etching with arbitrary depth and profile independent of crystal orientation opens up significant capabilities for micro and nano-optical waveguides, imprinting mold fabrication, micro fluidic and MOEMS devices. In this work, a micromachining technique has been developed by using Inductively Coupled Plasma (ICP) for achieving optical structures with arbitrary side wall profiles. The evolution of profiles in various masks under different plasma conditions is investigated. The profiles from V-groove to straight sidewall are realized by adjusting gas composition, ICP power, pressure, bias power and etching time. The processes of one-step and multiple steps as well as Bosch process of alternating deposition and etching steps have been explored to achieve a wide range of etch rates, etch selectivity and sidewall angles. The materials being investigated are silicon, silicon dioxide and lithium niobate.

This dissertation is organized as follows. In Chapter II, the previous researches of plasma etching are reviewed. In chapter III, one application of the V-grooved micro-optics structures is discussed. The V-grooved micro-optics design is developed and

simulated by the finite difference time domain (FDTD) method. The result of the simulation demonstrates a deep sidewall angle up to 80°, greatly enhances the fill factor of detectors. The realization of the V-grooved micro-optics waveguides will be presented in chapter VI. The fabrication steps are described in chapter V. In chapter VI, the inductively coupled plasma etching technique is illustrated, the fabrication processes are developed, the results and discussion are presented. Chapter VII includes the statistical experimental factorial design for controlling the sidewall profiles by adjusting processing gas composition, ICP power, processing pressure, bias power and etching time. Finally, conclusion and future work are summarized in chapter VIII. In addition, the characterization tools for this research are discussed in Appendix.

CHAPTER II

REVIEW OF RELATED RESEARCH

2.1 Material Properties and Applications

In this dissertation, the materials used in ICP etching are silicon, silicon dioxide and lithium niobate. In the next two sections, their properties and applications will be discussed.

2.1.1 Silicon and Silicon Dioxide:

Silicon is an essential material for micro- and nano-scale optoelectronic and microelectronic devices. It is widely used for the fabrication of microelectronic circuits (chips) and optoelectronic devices, micro-electromechanical system (MEMS), micro-optics devices, and silicon-based photonic integrated circuits. Pressure sensors, actuators, resonators gyroscopes, switches and other mechanical and electromechanical devices utilize the excellent mechanical properties (strength and flexibility) of silicon. Silicon surfaces can be used as micro-mirrors or as support for metallic or dielectric mirrors in micro-optics by its extremely flat and smooth surface. Silicon dioxide and silicon nitride can be deposited, or grown, and etched to form waveguides with graded or stepped refractive indices like optical fibers. Silicon optical modulators, optical routers and

optical switching systems have all been integrated into Si waveguides. Silicon can form stable and water insoluble oxide. The SiO_2 layer could act as a diffusion mask as well as an electrical isolation.

Optical absorption of silicon in the visible spectrum makes it suitable for photo detectors and solar cells. Since silicon is highly transparent from about $1.1\mu\text{m}$ to well into the THz region, it is widely used as window in IR cameras and photonics devices. Silicon crystal can grow rapidly. Its available wafer size has steadily grown, with 300 mm diameter wafers now in production.

2.1.2 Lithium Niobate:

Lithium Niobate (LiNbO_3) is a crystalline dielectric material and very useful for integrated optical devices such as tunable optical filters, frequency converters and wideband electro-optical modulators due to its excellent electro-optical, acousto-optical, and nonlinear optical properties. Lithium Niobate ridge waveguides and Lithium Niobate photonic crystal waveguides require anisotropic etching techniques. Current work on lithium niobate etching is primarily on wet etching using HF and HNO_3 ^{11, 12, 13}. Some work on plasma etching has been done in the past^{13, 14}, but very little literature exists on high density plasma or profile control of lithium niobate¹³. LiNbO_3 is a material hard to be etched.

2.2 Etching Mechanisms

In general, there are two classes of etching processes, wet etching and plasma (dry) etching. In wet etching, the material is immersed in a chemical solution and dissolved

through pure chemical reactions. Plasma (dry) etching, the material is physically sputtered by ion bombardments or dissolved using reactive radicals or the combination of physical and chemical reactions in the gas phase.

2.3 Wet Etching

Wet etching is a purely chemically driven etching and can be isotropic or anisotropic, depending on the chemical solution used and the materials being etched. Silicon substrate etching has been anisotropically patterned in KOH (potassium hydroxide). If (100)-oriented silicon wafers are used, anisotropic profiles can be achieved. But this technique gives a fixed etch angle of 54.7° ^{2, 3, 15} due to the crystallographic orientation of silicon as shown in Figure 2.1. The sidewall profile of the etched patterns cannot be arbitrarily controlled in KOH etch. For different sidewall profiles, especially vertical or other deep sidewall angles, wet etching could not achieve the goal. Wet etching can not provide precise critical dimension control and also creates contaminations. However, it is inexpensive to implement and has a fast etch rate and high selectivity, so it still has many practical uses.

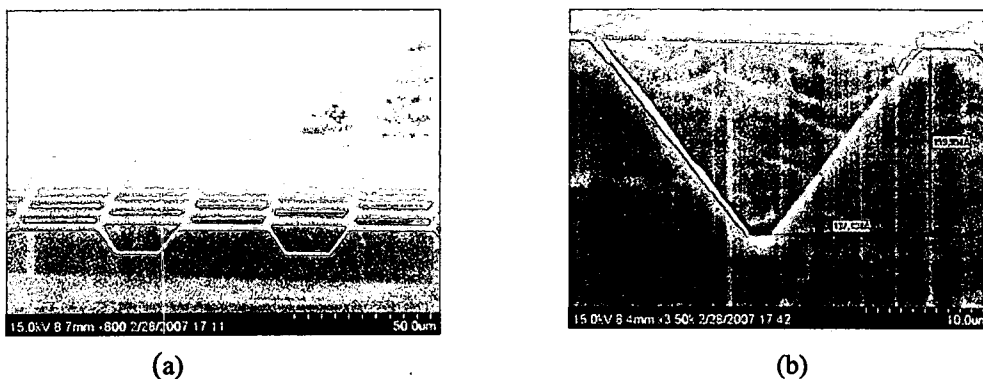


Figure 2.1: Silicon (100) 60% KOH wet etch (a) 20 minutes (b) 30 minutes at temperature 75C.

Silicon dioxide is typically wet etched by hydrogen fluoride (HF). Wet etching of Lithium niobate utilizes the proton-exchange technique. The Lithium niobate substrate is immersed in the H_2SO_4 , HF and HNO_3 at an elevated temperature for a period of time sufficient to provide the requisite exchange location of the lithium present in the substrate with the hydrogen from the acid as the proton donor. The shape of the etched region in the LiNbO_3 substrate can be controlled by using a mixture of HF/ HNO_3 acids ^{11, 13}. The etch rate depends on the composition of the etchant solution and exponentially depends on temperature.

2.4 Plasma (dry) Etching

Plasma etching is an important technology and widely used in the fabrication of large-scale integrated circuits¹⁶⁻¹⁸ with smaller feature sizes and highly anisotropic structures. Without the assistance of the plasma, much higher temperature would be required. The low processing temperature is possible because the plasma generates atoms, molecular radicals and positive ions that are more chemically reactive than the normal molecular gases from which the species are created. The gas molecules are dissociated into ions and free radicals which are very chemical reactive. For example, CF_4 in gas phase will not etch Si, but CF_4 in a plasma will etch silicon. The amount of energy need to break a C-F bond in CF_4 is 105 kcal/mole, the amount of energy necessary to break a Si-Si bond is 42.2 kcal/mole. For CF_4 to etch silicon, the sum of these two energies (147 kcl/mole) must be less than the energy of the Si-F (130 kcal/mole). Plasma etching is the combination of chemical etching (free radicals react with the materials being etched) and

physical etching (ion bombardment) by using plasma consisting of ions, free electrons, free radicals and neutral molecules.

The positive ions can be guided to the wafer surface in a directional manner, and especially at low pressures it provides highly anisotropic etch profiles. Plasma etching provides excellent critical dimension control and the ability to etch high aspect-ratio patterns. For the fabrication of ultra large-scale integrated (ULSI) circuits, fluorocarbon plasma etching has been established as one of the most important processes¹⁷⁻²¹. Many researchers have studied the selective etching of SiO₂/Si in fluorocarbon plasmas^{19, 23, 24, 39-42} to better understand the etch mechanism. Mechanism⁴⁵ of Si and SiO₂ etching have been studied in considerable details about the relevant plasma chemistries and plasma characteristics in recent years using plasma diagnostics to measure ions and neutrals in the plasma by a quadrupole mass spectrometer (QMS)^{31, 45} and by optical emission spectroscopy (OES)^{23, 39}, surface characterization techniques such as x-ray photoelectron spectroscopy (XPS)^{25, 39, 42} and ellipsometry³⁹, and scanning electron microscopy (SEM). Fluorocarbon gases are fragmented into many species as neutrals and ions. Using XPS and ellipsometry, Oehrlein et al.²⁵ found that C_xF_y plasmas generate a C-F polymer on the substrate surface and a reaction layer that is chemically composed of the substrate material and elements coming from the plasma. The formative stages of surface reaction and surface polymerization layers have also been quantitatively analyzed using XPS, time-resolved infrared spectroscopy, and transmission electron microscopy.

The following types of processes occur in the plasma when a gas contains molecule AB made from atoms A and B:

Dissociation:
$$e^* + AB \leftrightarrow A + B + e$$

Atomic ionization: $e^* + A \leftrightarrow A^+ + 2e$

Molecular ionization: $e^* + AB \leftrightarrow AB^+ + 2e$

Molecular excitation: $e^* + AB \leftrightarrow AB^* + e$

where the superscript * refers to a specie whose energy is higher than the ground state.

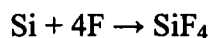
Dissociated atoms or molecular fragments are called radicals which have an incomplete bonding, therefore they are extremely reactive. With ions, electrons and radicals in the plasma, four basic etching mechanisms take place.

2.4.1 Ion Sputtering

Ions move directionally towards the substrate due to the potential difference of the plasma region and the substrate. Ion sputtering is a physical etching by ions bombarding on the substrate. The bombardment knocks out the atoms on the substrate. It has high anisotropic due to the high direction of ions, but low selectivity because ions sputter both mask material and the substrate. Argon gas is a good example of purely physical sputtering, since Argon is an inert gas.

2.4.2 Chemical Etching

The neutral radicals chemically react with substrate atoms and form volatile products, which are desorbed from the surface and are pumped out of the chamber. Such as Fluorine atoms can spontaneously react with silicon and form volatile SiF_4 gas.



Chemical etching is the most selective kind of process. However, the process is usually isotropic. It etches in both vertical and horizontal directions, forming a round profile and an undercut.

2.4.3 Ion-enhanced Etching

Ion enhanced etching is a combination of ion sputtering and chemical reaction. Ions dislodge the bond of substrate atoms and assist chemical reaction. The neutral radicals react with the substrate atoms and form volatile byproducts. Etch rate is enhanced in the ion direction due to bond dissociations. It produces anisotropic profile.

2.4.4 Ion-enhanced Protective-passivation

The neutral radicals react with the substrate atoms and form a non-volatile byproduct, polymer film, which coats on the surface forming a protective barrier. On vertical surfaces which protected by the thin film see little or no ion bombardment and the film prevents chemical attack of the feature sidewalls, thereby making the process anisotropic.

2.5 Reactive Ion Etch (RIE) System

In conventional RIE system, plasma is generated in a vacuum system between two parallel plates powered by an RF supply. The common frequency of operation of the RF power source is 13.56 MHz, chosen by the Federal Communications Commission (FCC) for industrial and scientific use. The ion and radical densities are 0.01% and 1% of total density. Therefore RIE system is referred as low density plasma. In this system, the ion density and ion energy are coupled and can not be controlled independently. Increasing

RF power will increase ion density, but at the same time it increases the ion energy which causes the damage on the mask and the substrate due to high energy ion sputtering.

The magnitude of DC bias depends on the plasma characteristics, the mobility of electron and the rate of secondary electron emission. Generally, lower pressure and larger RF power result in higher DC bias, which will lead to a higher sputtering rate.

2.6 ICP System

High density plasma sources at low pressure systems such as electron cyclotron resonance (ECR)^{23, 40, 42} plasma and inductively coupled plasma (ICP)^{34, 39, 43} have been developed to achieve high anisotropy and high etch rate. The plasma, generated by a surrounding coil, accelerates electrons to move in circular motions, thereby increases the path of the electrons, causing more collisions which induce more ionization and dissociation. Hence the ion density and radical density in such system can be large. The advantage of ICP is that one RF power source is used to generate a high-density plasma source (high ion current density, high plasma density and high ion flux), and the acceleration energy of the ions towards the substrate can be independently controlled by a second RF power supply used exclusively to generate the substrate bias voltage. So the energy of ions arriving at the substrate can be independently controlled without substantially affecting the chemistry of the plasma, e.g. the densities of ions and of other chemically active species, and at the same time avoid the damage associated with high energy processes such as ion beam milling (IBM) and conventional reactive ion etch (RIE). Therefore high etch rates may be maintained without damage to the substrate. The x-ray photoelectron spectroscopy (XPS)^{23, 39} surface analysis of the etched silicon and

SiO₂ gives more detailed surface information. The anisotropic and selective etching²¹ of SiO₂/Si is performed in various fluorocarbon (C_xF_y and CHF₃^{21, 42}) gas plasmas. The etching mechanism³⁹ of these materials in fluorocarbon (C_xF_y and CHF₃) gas plasmas is better understood now. It is now known that the etching and deposition are caused by the surface interaction between the substrate material and fluorocarbon radicals and fluorine atoms in the plasma. The polymer films are simultaneously deposited on the wafer surface during etching. When etching SiO₂ in fluorocarbon plasma, the carbon and oxygen form volatile CO and CO₂ instead of forming nonvolatile fluorocarbon polymers, leading to plasma that is rich in fluorine. Therefore, fluorocarbon gases etch SiO₂ faster than Si. The addition of oxygen to fluorocarbon plasma suppresses the formation of polymer film and increases the silicon etch rate, resulting in increased Si/ SiO₂ etching selectivity. A few articles have been devoted to modeling^{20, 29, 30, 39, 30, 46} the etching mechanisms in order to predict the etching process^{16, 17}.

2.7 Fluorocarbon Plasma

In a fluorocarbon plasma, the substrate simultaneously experiences polymer deposition, ion bombardment and free radical chemical etching. The passivation caused by the fluorocarbon polymer protects the sidewalls from any lateral etching, and an anisotropic profile is achieved.

The mechanisms for etching silicon dioxide and silicon are different. For SiO₂, three regimes^{18, 23, 39} can be distinguished: (i) a fluorocarbon deposition regime for low ion energy, (ii) an intermediate regime when increasing the ion energy called "suppression of the fluorocarbon film on oxide", where the etching is limited by the thickness of the

fluorocarbon blocking layer, (iii) for higher ion energy, a regime of ionic and reactive sputtering is reached. In this regime, the thickness of the fluorocarbon layer is less than 1 nm, and the penetration depth of ions is about 1 nm, so SiO_2 can be sputtered directly by ion impact. For silicon etching, there are only two regimes: (i) a deposition regime at low bias voltage and (ii) an etching regime for higher voltages where silicon etch rate depends on a fluorocarbon-blocking layer at the surface. The fluorocarbon layer on silicon is relative thick, about 2-7 nm, so the silicon cannot be sputtered directly by the ion impact. The silicon etch in fluorocarbon plasma is determined by a fluorocarbon layer which protects the silicon from direct ion impact^{36, 37, 39}. C_xF_y plasmas generate a CF_y polymer on the substrate surface and sidewall¹⁷. It is generally believed that CF_x ($x=1-3$) radicals are the major polymer deposition precursors. The formation of fluorocarbon film by CF_x radical deposition on the silicon surface prevents silicon from being etched and reduces the silicon etch rate¹⁶. So silicon etch rate depends on the atomic fluorine concentration in the plasma, on the fluorocarbon-blocking layer at the surface and on the ion energy controlled by the substrate bias power. The thickness of this blocking layer is related to the plasma species through the $(\text{C}+\text{H})/\text{F}$ ratio. Neither atomic fluorine gas (spontaneous etch) nor the ion flux (sputtering) alone will etch fluorocarbon layer significantly. The proper combination of fluorine species and ion bombardment is necessary. When the silicon is exposed to fluorocarbon ions and neutrals, its surface is fluorinated with SiF_y layer on the bulk silicon and the fluorocarbon film forms and stacks on the SiF_y layer. The atomic fluorine diffuses through the CF_x layer and reacts with CF_x layer and etches the CF_x layer with volatile $\text{C}_x\text{H}_y\text{F}_z$ and diffuses to the SiF_y layer right on the silicon substrate to etch silicon by desorbing volatile SiF_4 . The ions do not directly sputter the

substrate material, but the process is enhanced by the energy transferring from ion impact (ion-enhanced etching reaction). The thickness of the polymer is dependent on the bias voltage. With a negligible substrate bias, only net deposition takes place. Increasing the bias voltage, the polymer thickness decreases, though the deposition rate of polymer also increases. Above a certain threshold of the bias voltage, where the etch rate of polymer is larger than the polymer deposition rate, the net etching of the substrate takes place. The etching mechanism of silicon and fluorocarbon are similar. Their etch rates increase with bias voltage. The thickness of fluorocarbon layer varies as the bias voltage changes.

2.8 Sidewall Profile

Only a few articles ^{5, 25, 26, 34} have reported on the silicon etch profile. Oehrlein et al.²⁵ demonstrated the mechanism of etched sidewall profile due to the horizontal and vertical portions experiencing different etch regimes. On the bottom surface, the etching takes place at net etching regime by a biased power, ions remove polymer, make free radicals react with the material to be etched. The sidewalls experience almost no or fewer ion bombardments than the bottom surface does. The polymers on the sidewall surface protect it from the lateral etching. If the polymer etching balances the polymer deposition, the process leads to a vertical profile. The net lateral polymer deposition (more polymer deposition than polymer etching) leads to a tapered profile and the net lateral etching on sidewall leads to an undercut. I. Amirov et al.²¹ has reported that selective etching of SiO₂/Si in fluorocarbon plasma of CHF₃ or CHF₃ / H₂ in low-pressure ICP and the effect of etching conditions on the formation of a submicron groove in SiO₂. The character of

processes in narrow grooves is different from that occurring in an open area (micro loading). The etch rates are different for the blanket surface and for the sloped surface.

When plasma etch processes are used to define the microscopic features of integrated circuits, the differences in the surface-chemical processes occurring on the surface portions in line-of-sight of the plasma and at the sidewalls of the microstructures being etched as shown in figure 2 are of utmost importance in determining the surface profile of the final microstructure²⁵. If perfectly straight sidewalls are desired, either no reaction should occur at the sidewall or the deposition and etching rates need to balance exactly. Three kinds of processes form a sloped profile are shown in Figure 2.3.

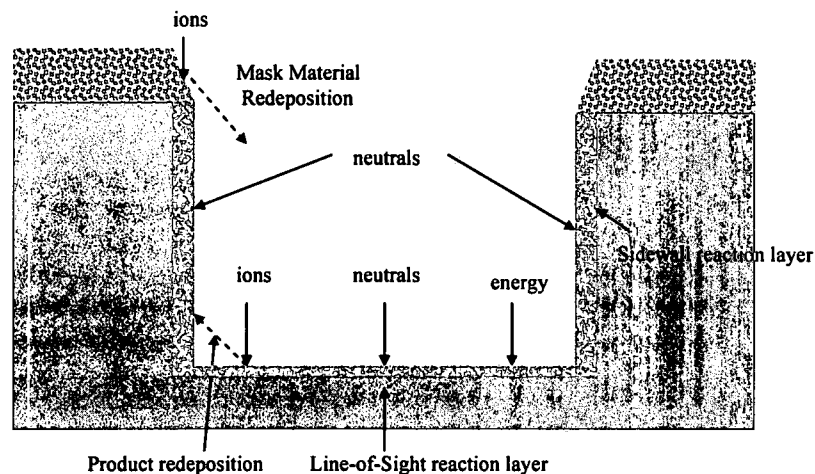


Figure 2.2: Ions and neutrals react with the mask and the substrate (Ref. 25).

2.8.1 Mask Erosion

The mask lateral etching in Figure 2.3(c) results the faceting of the photoresist mask edge, which transfers to the top of silicon sidewall.

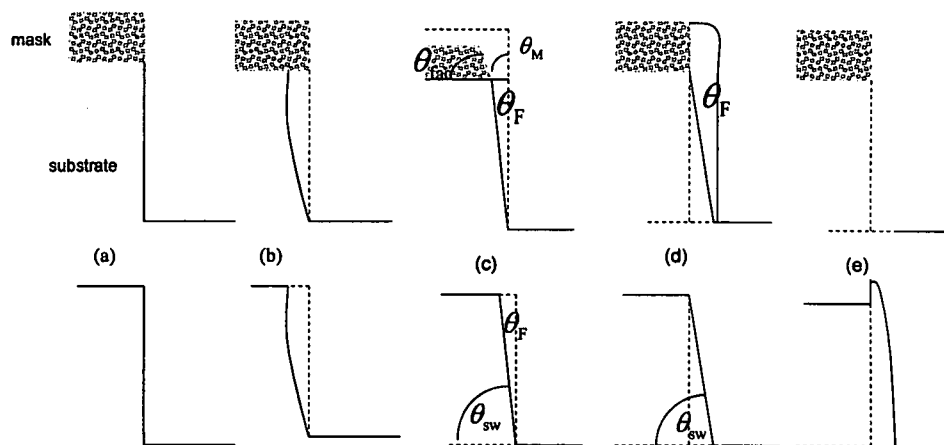


Figure 2.3: (a) Ideal straight wall etch, no lateral etch (b) isotropic etch with undercut (c) mask erosion, steady-state sidewall angle with decreased linewidth (d) eroded mask redeposition (e) sputtered product redeposition with increase linewidth. (Ref. 25)

2.8.2 Balanced Polymer Deposition and Polymer Etch

The polymer deposition rate is conformal on the bottom surfaces, the sidewalls, and the mask surfaces. But the polymer etch rate depends on the sidewall angle. A steady state sidewall angle is formed in Figure 2.3(c) under conditions when the polymer etch rate is equal to the polymer deposition rate.

2.8.3 Redeposition

The redeposition of the photoresist mask erosion is seen in Figure 2.3(d) and the redeposition of the etched (non-volatile) by-products is seen in Figure 2.3(e).

The etching mechanisms of silicon and oxide in a fluorocarbon environment are quite complex and still far from being completely understood at the present time. For lithium niobate, there are just few papers on the etching mechanisms¹⁴.

CHAPTER III

V-GROOVED MICRO-OPTIC DESIGN AND FDTD SIMULATION

Infrared focal plane arrays (IRFPAs) detectors are widely used in military, space, electro-optics applications. Basically an Infrared focal plane array (IRFPA) has two major parts, a detector array and a readout circuit as shown in Figure 3.1. In order to achieve a high resolution, technologies have evolved from the original one-pixel detector in 1970s to now available large format arrays, including 1024x1024 and even 2Kx2K large format arrays. The pixel size in the mean time has been reduced to 15 μ m.

As pixel pitch decreases, fill factor becomes extremely hard to maintain, particularly in reticulated focal plane arrays. The gaps between detectors must be minimized within the limits of current state of the art etching techniques in order to maximize fill factor. Adding micro-optic structure allows relief from this constraint for maintaining high fill factor while allowing flexibility in pixel architecture.

Traditional micro-optical structure utilizes focusing lenses at the top of the detector substrate that are physically separate from the detector, as shown in Figure 3.2. Although this technique can increase fill factor, but the focusing effect brings with it several limitations. Firstly, the effect of the micro-lens depends on optical system F# due to the distance from the micro-lens to the actual detector. Secondly, extremely small lens size

has small focusing effect. In addition, complex lens geometries are difficult to maintain uniformly across a large FPA. The ultimate goal is to avoid the gap between detectors. Meanwhile the metal grids encountered in some situations have to be avoided also, and so sometimes it is necessary not to focus the light to the center of pixels.

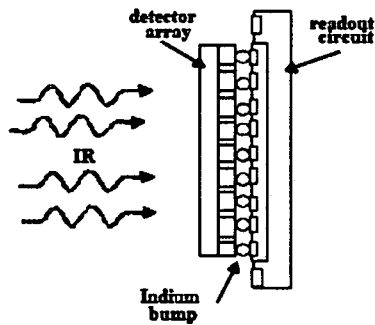


Figure 3.1: Schematic of IR FPA (Ref. 51)

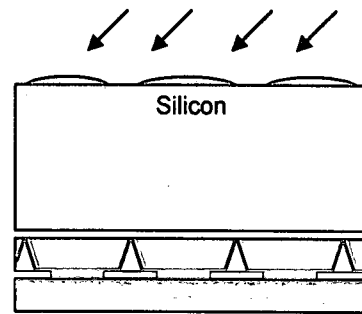
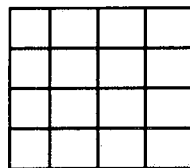


Figure 3.2: Micro-lenses on a reticulated FPA

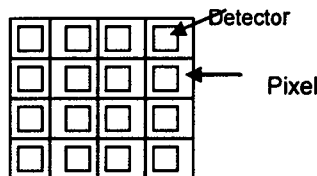
3.1 Fill Factor

Fill factor is defined as the percentage of light that falls on the useful part of the detector on each pixel compared to the total incident light on each pixel area. It becomes very hard to maintain a high fill factor as pixel pitches decrease. Reducing the pixel area, but keeping the area of gap or the area of the metal grids the same, the percentage of responsive area over non-responsive area decreases, therefore the fill factor decreases.

$$\text{Fill Factor} = \frac{A_{\text{detector}}}{A_{\text{pixel}}} \quad (3-1)$$



Fill Factor = 100%
Full focal plane array



Fill Factor = $A_{\text{detector}}/A_{\text{pixel}}$
Low Fill Factor focal plane array

Figure 3.3: Fill factor of the focal plane array

3.2 V-grooved Micro-Optic Design

A micro-optic waveguide was proposed which is comprised of a simple V-grooved notch directly above each detector gap to deflect incoming radiation towards the detector material and away from the gaps. The purpose of a micro-optic waveguide is to guide radiation away from non-responsive areas to the responsive areas within each pixel to increase the fill factor for a small pixel pitch. A simple notched micro-photonic waveguides above each detector gap can guide energy away from any gap area or metal contacts of a complex FPA geometry.

The light incidents on the silicon substrate and will reflect on the metal contact. If a V-groove is on the top of the metal contact, the light will be guided away from the notch. This approach is very well suited for extremely small pixel pitch. As the feature size becomes smaller than the wavelength, performance is actually increased.

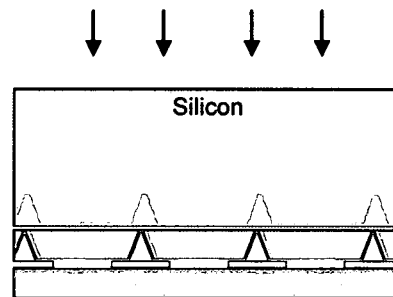


Figure 3.4: Micro-Optic structures on a reticulated FPA

This design has several advantages over the traditional micro-lens method. First, this is a very simple design, only a straight notch over the gap or metal grid. The notch can be designed and located directly at any location and can fit to any geometry. This approach is very well suited for an extremely small pixel pitch as discussed above. It demonstrates a good tolerance of system optical F#.

To predict the performance of the proposed micro-optic design, a number of simulations were developed. Since the micro-optics structures are of the same order of magnitude as the wavelength in the medium, conventional ray tracing algorithms are no longer suitable to predict its performance. The diffraction effect has to be considered in the simulations. Two main methods are used in these simulations. The first method was a finite-difference beam propagation method (BPM). This method is widely used in integrated optics to simulate the performance of waveguide-based devices. It is essentially a beam-tracing algorithm, similar in many ways to the conventional ray-tracing algorithm. The wave propagates in the forward direction depending on the local index of refraction. Numerically it simulates this process in a series of small steps, but in each small step, the phase correction is added to the diffracted wave. It is a very efficient and versatile technique. However, beam propagation simulations do not take backscatter into account. It is a one-way beam tracing model. In order to accurately model the backscatter, a finite-difference time-domain model was developed. This technique directly solved Maxwell's equations by integrating in both time and space. It considers diffractions and accurately captures reflections on all interfaces. However it requires intensive computational resources. So the simulations are carried out in BPM first, and then the reflectance and the fill factor are calculated in 2D FDTD.

3.3 The 3D Finite-Difference Beam Propagation Method

Applying 3D finite-difference beam propagation method, it is traced and simulated for the light passing through the micro-optic structures.

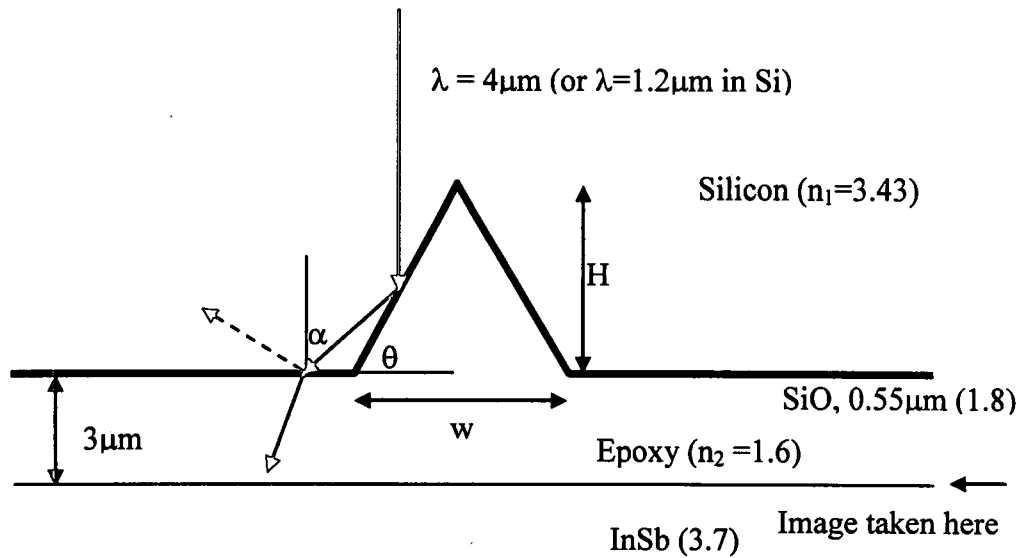


Figure 3.5: The cross-sectional view of the micro-optic geometry used for a numerical simulation

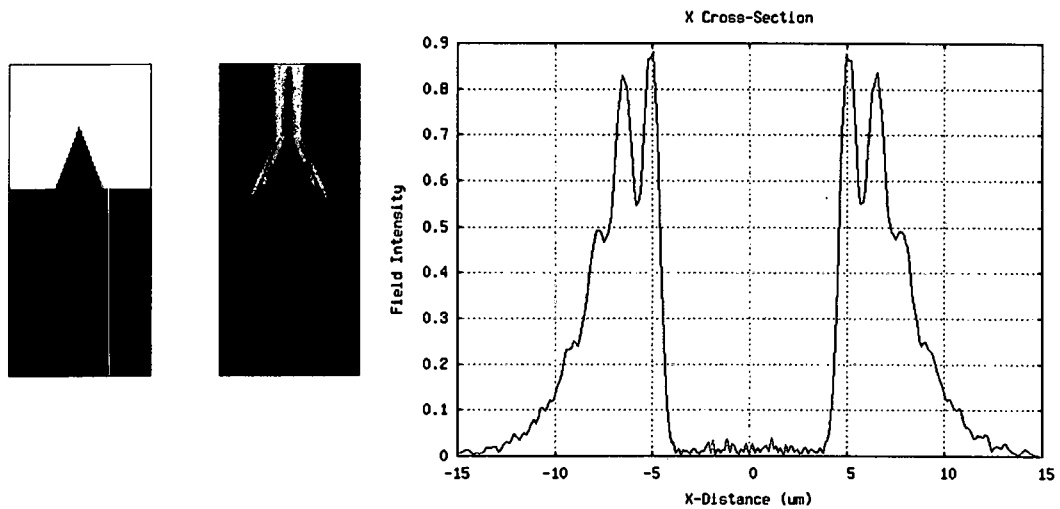


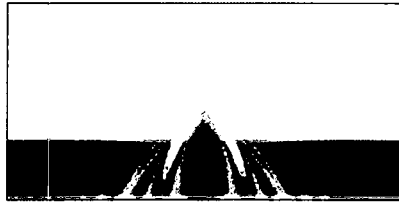
Figure 3.6: The notch structure, the field distribution and the field intensity plot at the detector.

As a Gaussian beam, its waist is approximately the same dimension as the notch dimension, propagates down from the top towards the notch. The image is taken at the detector surface which is at a fixed distance below the silicon surface, with several intervening anti-reflection films and a bond line in between the micro-optic element and the detector.

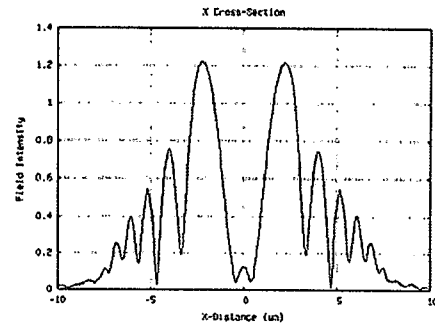
The simulation shows that the notch repels the incident radiation, redistributes energy that would otherwise be confined to the center, outward to the side of the notch. It redirects the input energy away from the gap or metal contact and into regions that are highly responsive as show in Figure 3.6.

The notch repels the incoming wave to the sides of the notch due to the low refractive index of the epoxy than silicon. If the notch is of the same order of magnitude as the wavelength, the field becomes mainly accumulated to the edge of the silicon/epoxy interface and propagates downwards along the notch sidewall instead of being reflected sideways away from the notch. At the silicon/epoxy interface, along the bottom surface of the notch, the beam is mainly guided downwards, with a small amount of reflection away from the notch. The amount of the reflection depends on the notch angle, and the antireflection coating on that surface.

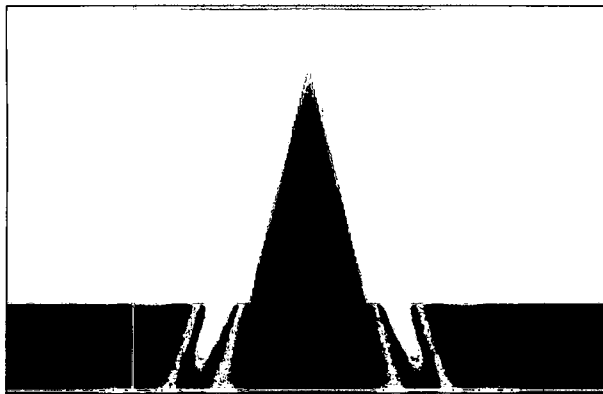
The Figure 3.7 (a) shows the BPM simulations of $2\mu\text{m}$ wide notch at an etch angle of 54.6° deg, which corresponds to the crystal planes of an anisotropic wet-etch (KOH) on (100) silicon. The plot (b) is the field distribution below the notch. The simulation clearly demonstrates the effect of the notch dividing the incident field into two components and guiding them sideways. The Figure 3.7 (c) and (d) show the BPM simulation of $4\mu\text{m}$ notch wide at a notch angle of 76° .



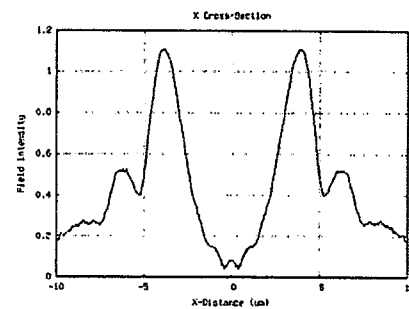
(a) Cross-sectional field distribution in a 2μm micro-optic at 54.6° etch angle



(b) Cross-sectional field distribution in a 2μm micro-optic at 54.6° etch angle



(c) Cross-sectional field distribution in a 4μm micro-optic at 76° etch angle



(d) Cross-sectional field distribution in a 4μm micro-optic at 76° etch angle

Figure 3.7: The BPM simulations

3.4 The Finite Difference Time Domain (FDTD) Simulations

FDTD is a fully-numerical technique that has the least number of approximations compared to any other simulation technique. This technique directly solves Maxwell's equations by integrating in both time and space.

The relationships of the notch height H , the opening width W , the notch angle θ and angle α in Figure 3.5 are shown in equations (3-2) and (3-3), and Table 3.1 shows 3 notch angles θ and the corresponding angle α :

$$H = \frac{w}{2} \tan \theta \quad (3-2)$$

$$\alpha = 180 - 2\theta \quad (3-3)$$

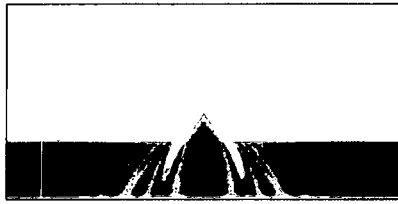
The critical angle of total internal reflection (TIR) is

$$n_1 \sin \theta = n_2 \quad (3-4)$$

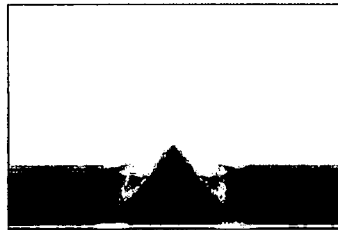
The critical angle at the interface of Si and epoxy is 27.8° .

Table 3.1: A relation between angle θ and α

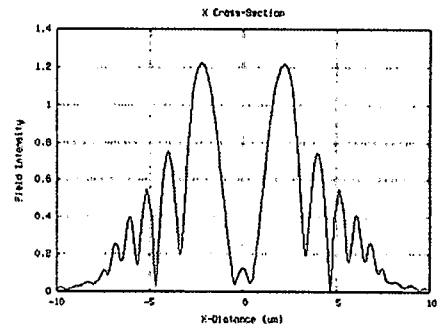
| θ | α |
|----------|----------|
| 54 | 72 |
| 76 | 28 |
| 45 | 90 |



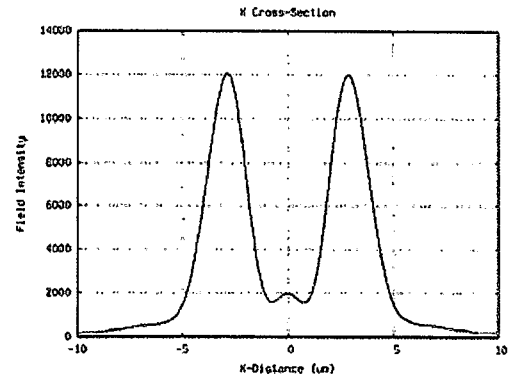
Cross-sectional field distribution in a $2\mu\text{m}$ micro-optic at 54.6° etch angle using BPM simulation



Cross-sectional field distribution in a $2\mu\text{m}$ micro-optic at 54.6° etch angle using FDTD simulation



Cross-sectional field distribution from BPM simulation



Cross-sectional field distribution from FDTD simulation

Figure 3.8: Comparisons of BPM and FDTD simulations.

Comparing the results of FDTD method with the BPM, they show very similar profiles. But small ripples on the beam due to the standing waves can be seen to show that the FDTD is able to accurately capture the reflected beam.

The integrated intensity at the incident plane $|E_i|^2$ and the transmitted plane $|E_T|^2$ are calculated through the simulation, and transmission and reflectance of the micro-optic structures can be calculated with equations (3-5) to (3-8):

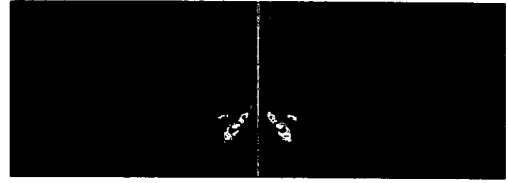
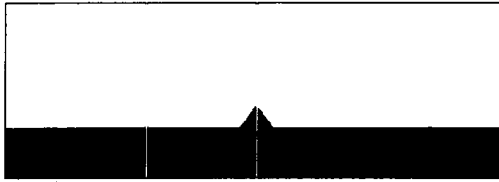
$$P_i = n_1 |E_i|^2 \quad (3-5)$$

$$P_T = n_2 |E_T|^2 \quad (3-6)$$

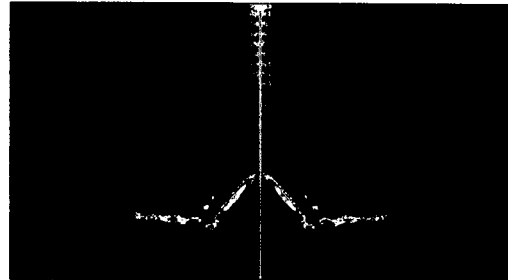
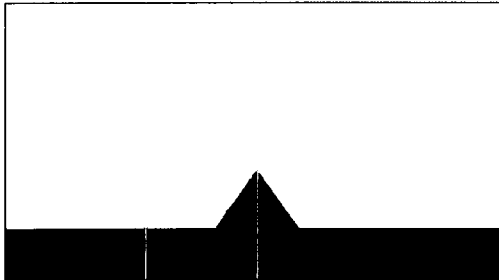
$$T = \frac{P_T}{P_i} = \frac{n_2}{n_1} \frac{|E_T|^2}{|E_i|^2} = \frac{n_2}{n_1} \quad (3-7)$$

$$R = 1 - T \quad (3-8)$$

where P_i is the incident energy, n_1 is the refractive index of the incident medium, P_T is the transmitted energy, n_2 is the refractive index of the transmitted medium, T is the transmittance and R is reflectance.

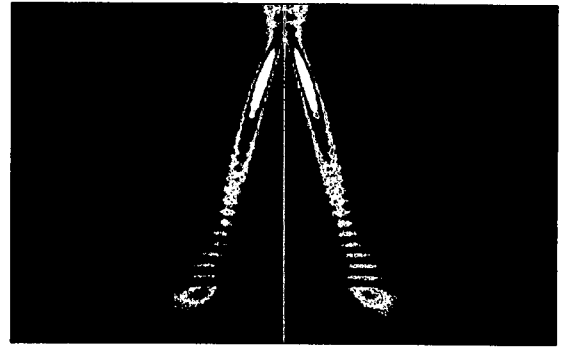
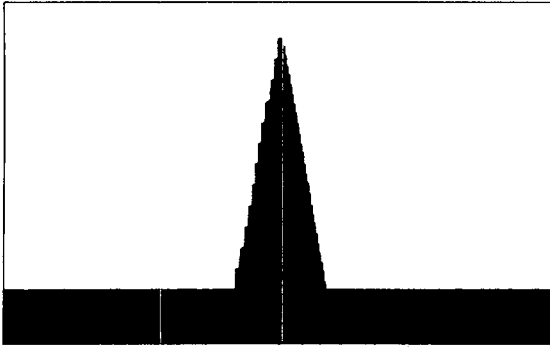


(a) $w = 2 \mu\text{m}, \theta = 54^\circ$



(b) $w = 5 \mu\text{m}, \theta = 54^\circ$

Figure 3.9: The FDTD simulations (a) $w = 2 \mu\text{m}$ and (b) $w = 5 \mu\text{m}$ at 54° .

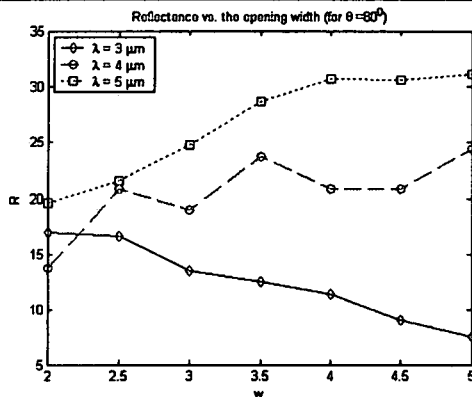


$$5\mu\text{m}, \theta = 80^\circ$$

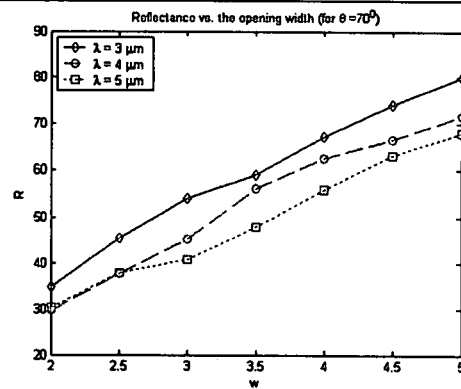
Figure 3.10: The FDTD simulation of $w = 5\mu\text{m}$ and $\theta = 80^\circ$.

From Figure 3.10, it shows the large width w has a higher reflection at the same notch angle. Figure 3.11(a) –(c) show the reflectance as a function of the open width of the notch at the notch angles 80° , 70° and 54° for wavelength 3, 4 and 5 μm . The reflectance increases significantly as the width increases from 2 to 5 μm for the angles of 70° and 54° , and it increases with the decreases of wavelength. The fill factor decreases with the increase of the width and the decrease of the wavelength as in Figure 3.11 (d) to (i). But at the large notch angle 80° , the reflectance changes very small, and the fill factor is about independent of the notch opening width and the wavelength.

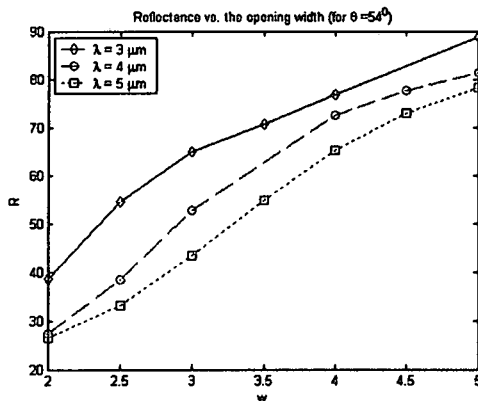
When the dimensions are larger compared to the wavelength in the material, ie 5 μm , the geometrical limit applies. Most of the radiation will be reflected back into the Si at the Si/SiO/epoxy interface due to total internal reflection. So the large openings will require large etch angles (76°) to have a high fill factor. Increasing the width w has a same effect as decreasing wavelength; both cases approach to the geometrical limit, so the fill factor decreases.



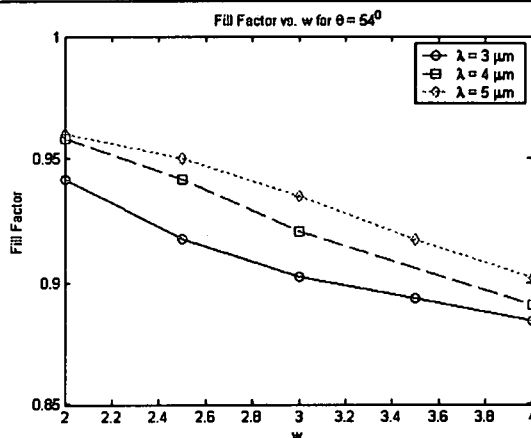
(a) Reflectance vs. the notch width. The smaller reflectance at deep etch angle 80° with different wavelengths



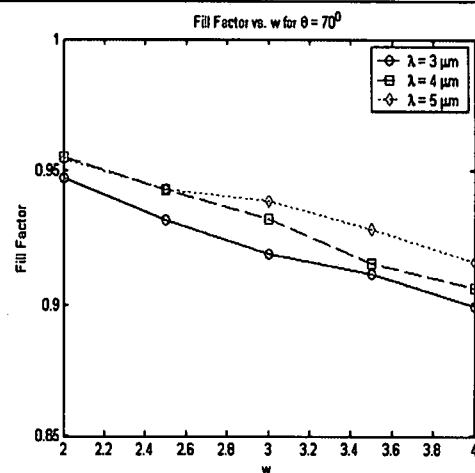
(b) The reflectance increases as the notch width increases for an etch angle 70° with different wavelengths.



(c) The reflectance increases as the width of opening increase for an etching angle 54° with different wavelength



(d) The fill factor increases as the notch width decreases for an etch angle 54° with different wavelengths.



(e) The fill factor increases as the notch width decreases for an etch angle 70° with different wavelengths.

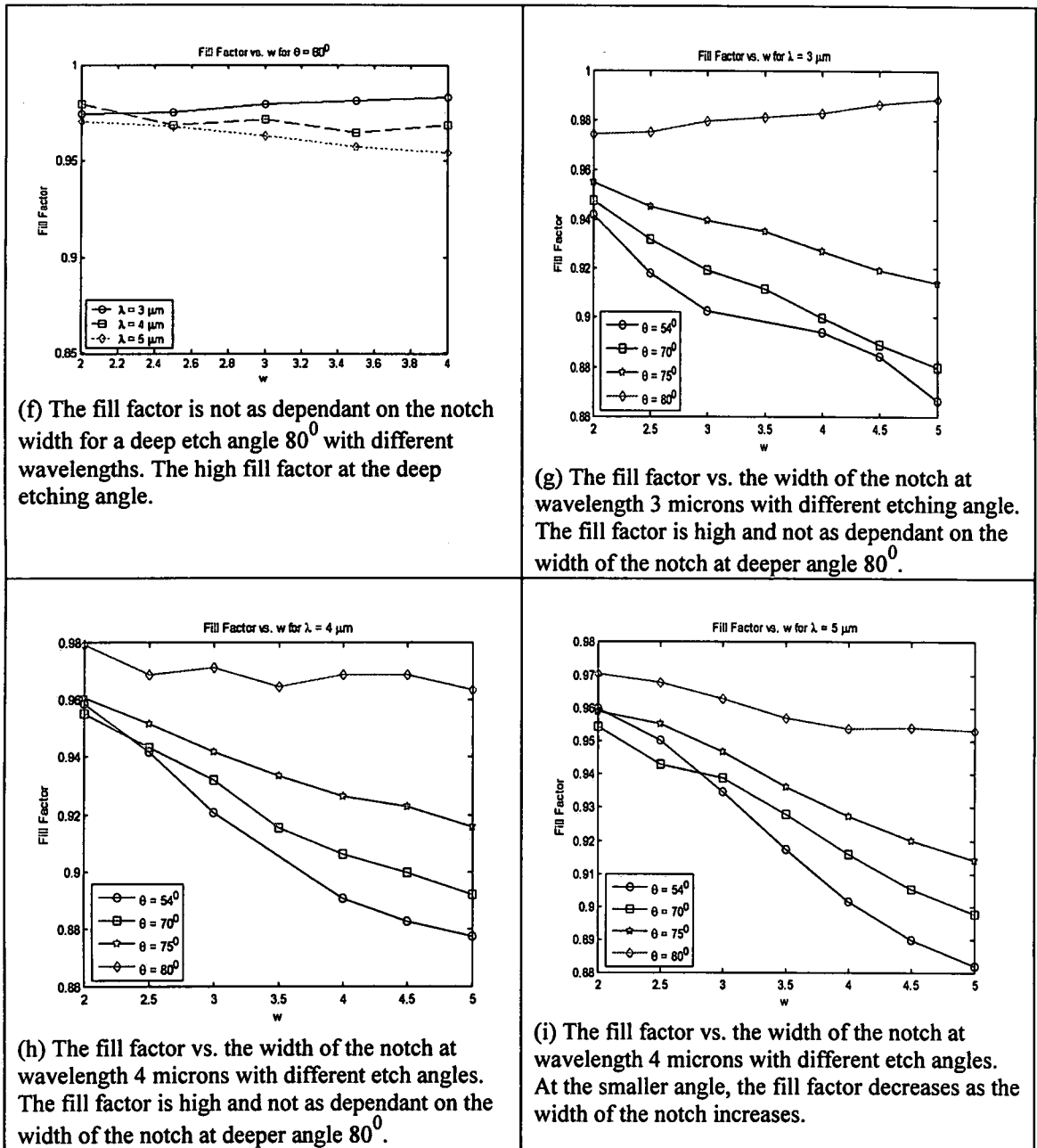


Figure 3.11: The reflectance and the fill factor as functions of the width w at the different wavelengths and the notch angles.

The reason of a high fill factor at the large notch angle, is that the incoming light incidents at an angle larger than the critical angle, the light is total internal reflected (TIR) on the notch sidewall. No light is transmitted to the inside of the notch, which area has a smaller refractive index. The FDTD result shows that there is extremely low intensity,

nearly zero under the notch. On the bottom of the notch, the light reflected from the notch continuously propagates and incidents at an angle α on the interface surface. When the notch angle θ is larger than 76° , the angle α is smaller than the critical angle 28° , the beam is dominantly transmitted downwards, with a small amount of reflection away from the micro-optics. This amount of reflection can be further reduced by an antireflection coating on that surface.

From above plots, the fill factor is increasing with decreasing of w , the opening of the notch. The fill factor strongly depends on the height or the etching angle θ . As the angle θ increases, the fill factor increases. So the deeper etching improves the performance. At a deep etching angle as 80° , the fill factor is not as dependent on width as it is at low etching angle, so the larger etching opening width can be chosen to achieve accurate alignment of the micro-optic structures. Simulations predict that steep groove angles are necessary to gain significant improvements in performance. So for the micro-optic structures on the FPAs, it is aimed to fabricate V-groove structures at a deep sidewall angle larger than 80° based on the prediction of the simulations. The fabrication of the micro-optic structures and its result will be shown and discussed in chapter V.

CHAPTER IV

MICRO-OPTIC FABRICATION STEPS

4.1 Mask Fabrications

Three different etch masks (photoresist, Al_3O_2 and Chromium) have been fabricated and used for ICP etching. Figure 5.1 shows the process steps of two mask fabricating methods.

4.1.1 Photoresist as the Etch Mask

The steps for making photoresist as the etch mask on a silicon substrate wafer are as shown in figure 5.1. The wafer is first cleaned with a sequence of acetone, methanol and isopropanol, and followed by nitrogen dry clean. The photoresist is coated on a spin coater. The thickness of photoresist depends on the speed of spinning and the type of resist. The wafer is soft baked at 100°C for 90 seconds. The UV light is used to expose the photosensitive resist-covered wafer with a photomask containing the design. Suss Mask Aligner MA6 is used for UV exposure at the wavelength 365nm. After the exposure step the wafer is post-baked at 110°C for 60 seconds for stabilizing and hardening the exposed photoresist and for getting smoother sidewalls after developing. The wafer is put in a developer solution for removing soluble photoresist. In the case of a positive resist, the

exposed areas become more soluble in a developer, and a negative resist unexposed area becomes soluble in a developer. The remaining photoresist will be used as mask in ICP etching process.

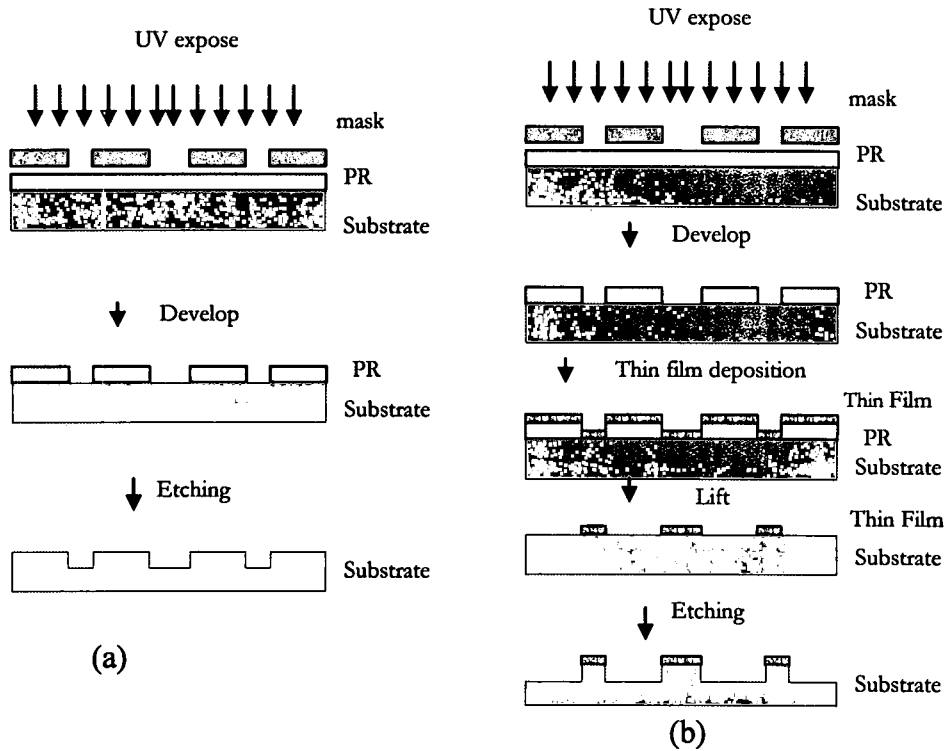


Figure 4.1: (a) Fabrication of Photoresist as a mask and (b) Fabrication of Al₂O₃ or Cr as a mask by a lift-off process.

4.1.2 Fabrication of Al₂O₃ and Cr as Masks

Al₂O₃ or Cr thin film is chosen to be masks for ICP etching silicon due to a very high selectivity of Si over Al₂O₃ or Si over Cr. The wafer is first cleaned with a sequence of acetone, methanol and isopropanol, followed by nitrogen dry clean. A resist called lift-off resist (LOR) type 10B is coated onto the substrate prior to applying the photoresist. The purpose of LOR is to create an undercut after developing the resist that will help during the lift-off process. Figure 4.1 (b) shows the mechanism of the lift-off process. The LOR

is spin coated at 2000 rpm to get a thickness of approximately 12500Å. The wafer is soft baked at 180°C for 5 minutes. Figure 4.2 shows the relation between LOR spin speed and its thickness. SPR955-CM type 1.4 is used for the positive photoresist. It is spin coated at 3000 rpm. The wafer is then exposed by an UV light through the designed mask to transfer the pattern. The wafer is post baked at 100°C for 90 seconds. Figure 4.3 shows the relation between SPR955-CM spin speed and its thickness.

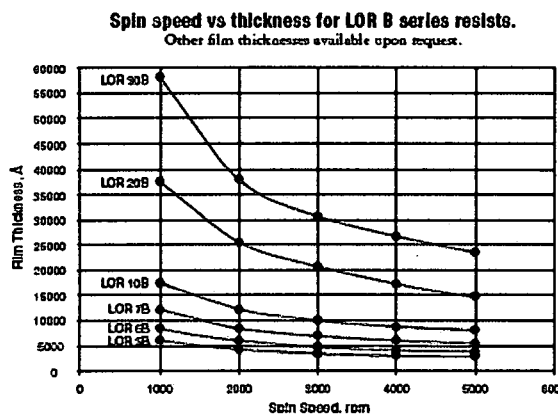


Figure 4.2: LOR thickness vs. Spin speed (Ref. 52)

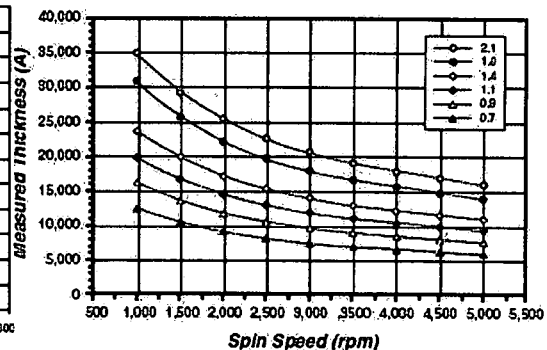


Figure 4.3: SPR955-CM thickness vs. Spin speed (Ref. 53)

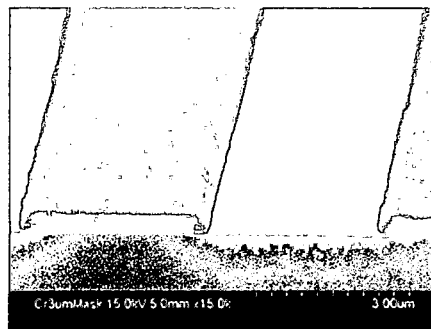


Figure 4.4: The SEM cross sectional view of Cr mask by E-Beam Evaporation.

After exposure to UV light, the wafer is then developed in a developer bath (containing MF-319) where the exposed photo-resist is removed. A thin film of Al_2O_3 or Cr is deposited on the wafer by E-Beam evaporation. The thin film, together with

photoresist below the film are removed or lifted-off with a solvent, called edge bead remover (EBR) in an ultrasonic clean. The wafer is again cleaned with acetone, methanol and isopropanol and is blown with nitrogen. The remaining thin film Al_2O_3 or Cr such as in figure 4.4 will be used as mask in the ICP etching process.

4.1.3 Electron Beam Evaporation

In electron beam evaporation, the electron beam from a tungsten filament is generated and accelerated by a high voltage 6KW DC power supply. A high intensity electron beam is directed by a magnetic field and focused towards the source material that is placed in a water cooled graphite crucible. The source material in the crucible is bombarded by the high energy electron beam, causing it to sublime or evaporate. In a high vacuum chamber, the vapor from the molten source travels in a straight line with a long mean free length and deposits only on the line of the sight on the substrate which is held on the top of the chamber. The mean free path is very long when the chamber pressure is in a few of μTorr , the molecules from the vapor are highly directional to reach to the substrate, the deposited film only cover the line of the sight, leaves the vertical sidewall uncovered. The thin film deposition by E-beam evaporation is especially suitable for the lift-off. The TORR International Inc Electron Beam Evaporation System as shown in figure 5.4 is used in this work and it consists of a vacuum system including a 500 l/s turbo-molecular pump and a dry mechanical pump, a quartz crystal thickness monitor, a stainless steel chamber, one electron beam source, one power supply, and a deposition control system.



Figure 4.5: Torr Electron beam evaporation system.

4.2 Etching

The patterned sample is transferred to the chamber of the ICP tool and placed on the cathode terminal electrode. The selected gas is fed into the chamber. Under an RF ICP source power and a RF bias power, the unprotected sample is removed by a synergy of physical sputtering by ion bombardment and chemical reaction by reactive radicals. The detail of the ICP etching will be discussed in chapter V.

After etching, the remaining photoresist is removed in acetone with an ultra sonic vibration. The Al_2O_3 or Cr mask is cleaned by wet etching.

The etched sample is examined and characterized with the characterization techniques described in Appendix, and thickness and profile are measured using an appropriated characterization tool. The objective is to optimize the process, to have high etch rate, the desired sidewall profile and smooth surface.

CHAPTER V

INDUCTIVELY COUPLED PLASMA ETCHING TECHNIQUES AND RESULTS

5.1 Introduction

In this research, an inductively coupled plasma etching technique is employed using the Unaxis Shuttleline Inductively Coupled Plasma reactor as shown in Figure 5.1. In Figure 5.1 (b), the top coil is supplied a 2 MHz RF power variable up to 1500 watts and the substrate electrode is supplied 13.56 MHz RF power variable up to 600 watts. This allows separate control of the plasma density at the top coil and sheath bias at the lower electrode. Electrons are heated by an electric field that exists at right angles to the induced magnetic field. High plasma densities can be achieved because power can be transferred into the bulk plasma via the magnetic field resultant from inductive coupling. The ICP Shuttleline reactor is based on a cylindrical coil configuration. In this configuration, the RF energy is introduced by an inductive coil to an Alumina (Al_2O_3) dielectric vessel. A strong magnetic field is induced in the center of the chamber. This coil configuration is very efficient at coupling RF power into the low-pressure gaseous medium. Due to the low operating pressure, the excited plasma species are less susceptible to collisional recombination so a high density is maintained at reasonable power levels. A 3 inch or 4 inch wafer is mechanically clamped to the substrate holder

which is connected to the second RF electrode. Helium gas is applied to the backside of the wafer to maintain good thermal contact between the temperature-controlled holder and the wafer. The chamber is first pumped by a rough pump to the turbo crossover pressure of around 30 mTorr. Then the turbo molecular pump as shown in Figure 5.3 starts and pumps chamber to a base pressure typically around 1×10^{-6} Torr. When the process gases are introduced into the chamber, the chamber pressure can be controlled by a throttle valve that can be set to any value. Substrates are loaded via a load lock so that the process chamber can be kept under permanent vacuum to keep out moisture and contaminants. This assures consistent and repeatable results. The load lock is separated from the chamber by a slit. The sample is automatically transferred by a belt-driven shuttle arm automatically from the load lock into the chamber. The processing gases are introduced to the chamber via individually calibrated mass flow controllers and fed into the chamber via a single line at the top of the chamber wall.

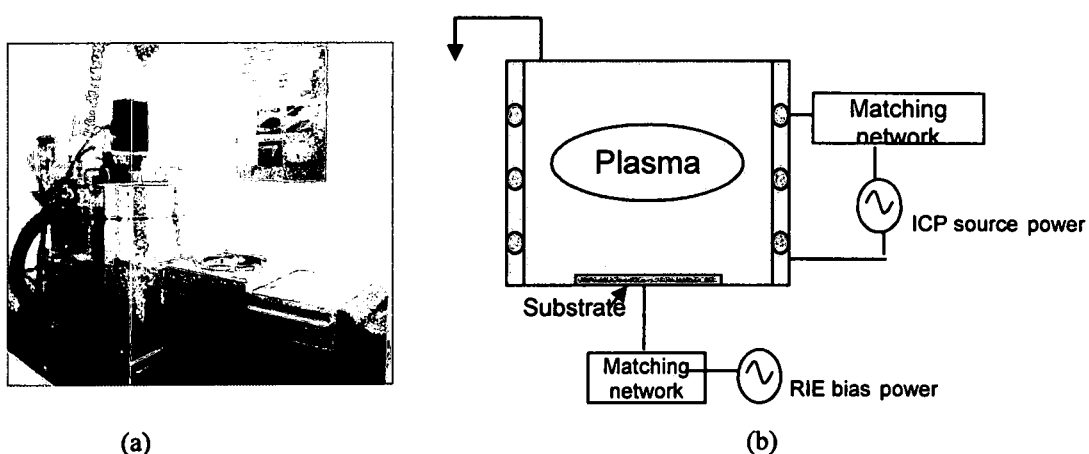


Figure 5.1: (a) Unaxis ICP Shuttleline in our nanofabrication lab and (b) Schematic drawing of ICP.

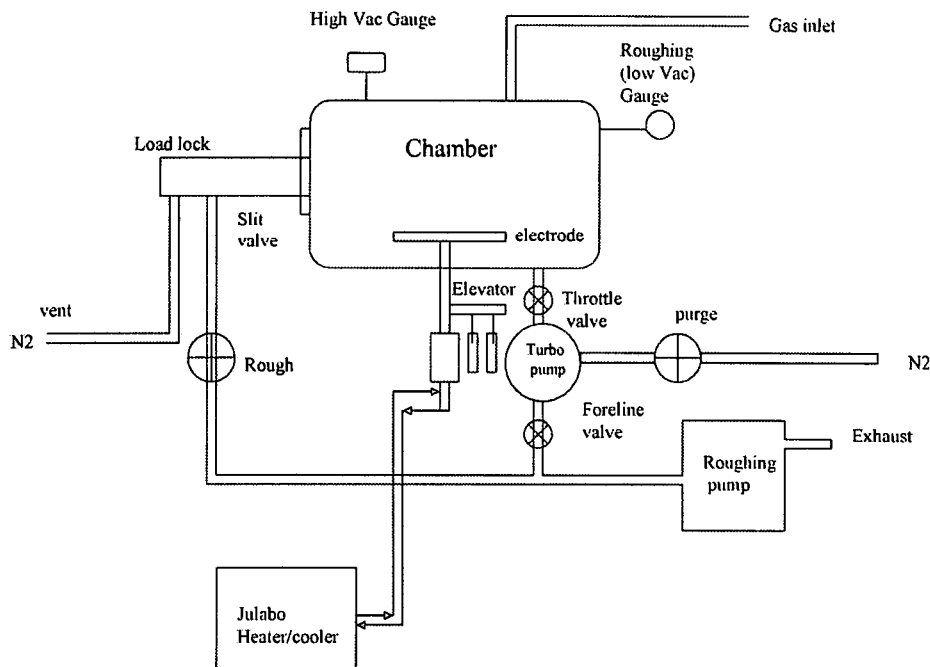


Figure 5.2: ICP Diagram

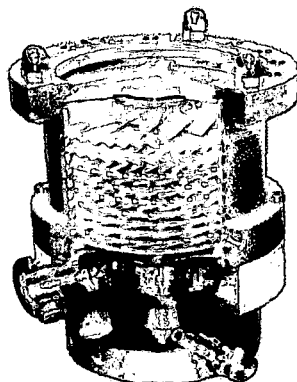


Figure 5.3: Turbo pump (Ref. 50)

In this research, the effect of gases CF_4 , CHF_3 , SF_6 and gas mixtures with argon, oxygen were studied on silicon, silicon dioxide and lithium niobate with the photoresist, Al_2O_3 and chromium acting as the etching masks.

The CF_4 gas is dissociated into ion species CF_3^+ , free radicals CF_3 , CF_2 , C , and F atoms by electron impact processes. The ions are accelerated towards the substrate by the

substrate RF power. The free radicals chemically react with the substrate material. So the fluorocarbon plasma etching of silicon is a combination of chemical (reactive) and physical (ion bombardment) processes. The fluorocarbon films form on the substrate surface and the sidewalls. The sidewalls experience fewer ion bombardments. Therefore, the film formation and etching reactions are different for horizontal surfaces and vertical sidewalls.

The effect of gases CF_4 , CHF_3 , SF_6 and gas mixtures with argon, oxygen were studied on blank silicon and micro-optic structures with the photoresist, Al_2O_3 and chromium acting as the etch masks. The etch rate of blank silicon wafer, silicon dioxide film deposited on silicon substrate by plasma enhancement chemical vapor deposition (PECVD) method, and the etched sidewall profile of micro-optics structures are fully investigated as functions of RIE bias power, ICP source power, operating pressure and substrate temperature.

5.2 ICP Etching of a Blank Silicon Wafer

The part of a blank substrate was covered with a high temperature tape, and the back side of the sample is mounted with thermal grease on the silicon wafer carrier which is held on the cathode. The silicon wafer was maintained at a setting temperature by flowing cooled helium to the back side of the wafer. After processing, the tape is removed; the height of etched steps is measured by an Ambios Stylus Profilometer and the etch rate was determined.

5.2.1 RIE Bias Power

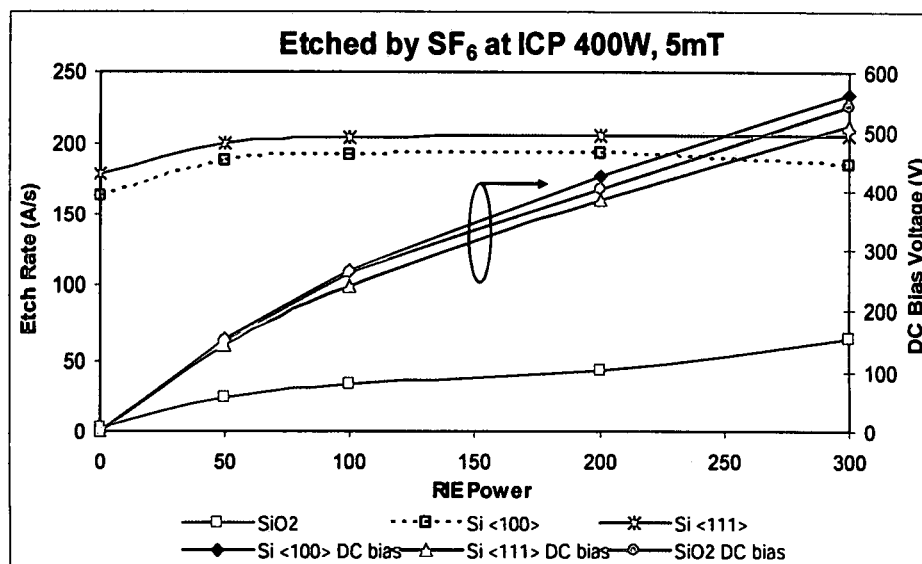


Figure 5.4: The etch rates (left) and DC bias voltage (right) of Si <100>, <111> and SiO₂ as functions of RIE bias power in SF₆ plasma.

Figure 5.4 shows the etch rates (left) and DC bias voltage (right) of Si <100>, <111>, and SiO₂ as functions of RIE bias power in SF₆ plasma. The ICP power is set at 400 W, the operating pressure at 5 mTorr and the substrate temperature at 25⁰C. At the same RIE bias power, a lower DC bias means a higher ion flux to the substrate. The DC bias of Si <111> is lower than that of Si <100> at the same RIE bias power, therefore a higher ion flux to the substrate of Si <111>, results in a higher etch rate of Si <111> than that of Si <100>. The DC bias of SiO₂ is between those of Si <100> and Si <111>, but the etch rate is much lower than Si <100> and <111>. This is because the contribution of chemical reaction of fluorine atoms with SiO₂ is much lower than that with Si.

It is clear to see that SiO₂ is significantly affected by RIE power in SF₆ plasma, while Si is almost independent of RIE power. Silicon can spontaneously react with fluorine atoms without activation energy from ion bombardments. The contribution from its

chemical reaction is much higher than the physical ion bombardment, and the contribution from the physical sputtering did not affect the overall etch rate. So the etch rate is not significantly affected by RIE power. That is why silicon etching by SF_6 is isotropic, resulting in the same etch rate in both vertical and horizontal directions. But the SiO_2 bond is very strong, and at no bias power the etch rate is almost zero. The activation energy from ion bombardment is needed to break the bond of Si and Oxygen, and then the free fluorine atom can chemically react with Si. The etch rate of SiO_2 increases with the RIE bias power. So the etch rate of SiO_2 is significantly influenced by the ion bombardment. SiO_2 etching is thus anisotropic by SF_6 . The selectivity of Si over SiO_2 is very high, so SiO_2 is a good mask to etch Si in SF_6 . This is shown on the left side of Figure 5.5.

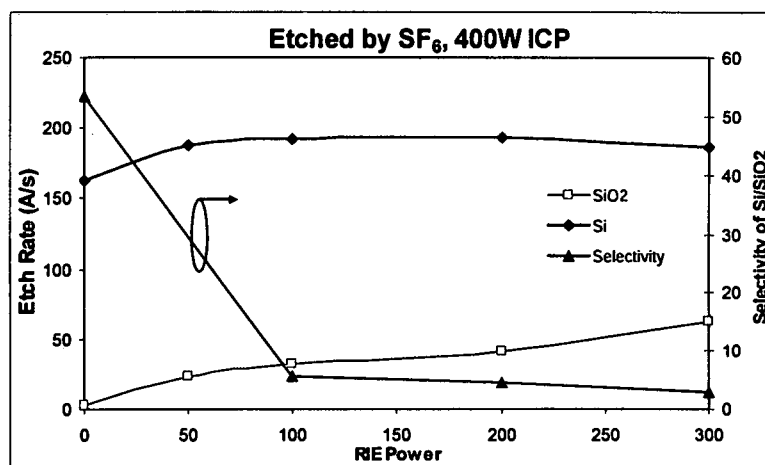


Figure 5.5: The etch rate (left) of Si and SiO_2 and the selectivity (right) of Si over SiO_2 as functions of the RIE bias power in SF_6 plasma.

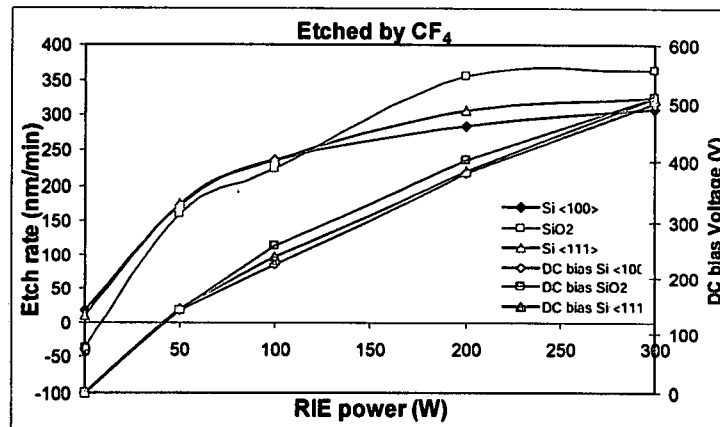


Figure 5.6: The etch rates (left) and DC bias voltage (right) of Si <100>, <111> and SiO₂ as functions of RIE bias power in CF₄ plasma.

In Figure 5.6, the etch rate of SiO₂ in CF₄ is higher than those of Si<100> and Si <111> at the bias power higher than 120W. Carbon atoms dissociated from CF₄ plasma and oxygen atoms knocked out from the substrate by ion bombardments form a volatile product CO₂. This result in a high density of fluorine atoms, thereby increasing etch rate of SiO₂. At the zero bias or bias power lower than 15 W, the net polymer film deposits on the SiO₂ substrate at the operating pressure of 5 mTorr. Again the activation energy from ion bombardment is needed to break the SiO₂ bond. But the etch rates of both silicon and SiO₂ increase with the RIE power and they are significantly affected by the RIE power in CF₄ plasma. The selectivity of Si over SiO₂ is close to 1 as shown on the right axis of Figure 5.7.

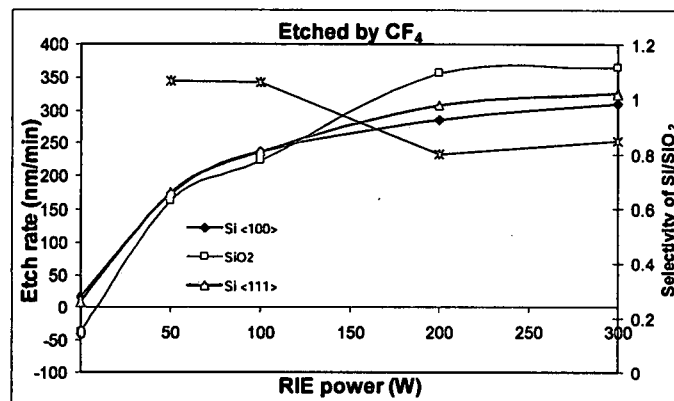


Figure 5.7: The selectivity (right) of Si over SiO₂ as a function of RIE bias power in CF₄ plasma.

In Figure 5.8 the etch rate and DC bias increase with the RIE bias power in CHF₃ plasma. The etch rate is higher at lower pressure of 5 mTorr than 15 mTorr, while the DC bias at 5 mTorr is lower than that at 15mTorr at the same bias power. The lower DC bias voltage at 5mTorr indicates a higher ionization rate and a higher ion flux. With a longer mean free length at a lower pressure, the ions experience less scattering, therefore the directional ion flux to the substrate is higher. For both pressures when RIE is at zero bias, the net polymer deposition on silicon was observed. Activation energy is needed to start etching silicon in CHF₃ plasma. The threshold bias power is little higher at 15 mTorr than that of 5mTorr due to a lower directional ion flux at a higher pressure. The polymer film is not observed on silicon by CF₄ gas at 5mTorr. So later on we chose CHF₃ to fabricate the micro-optic structures in order to utilize polymers passivating sidewalls.

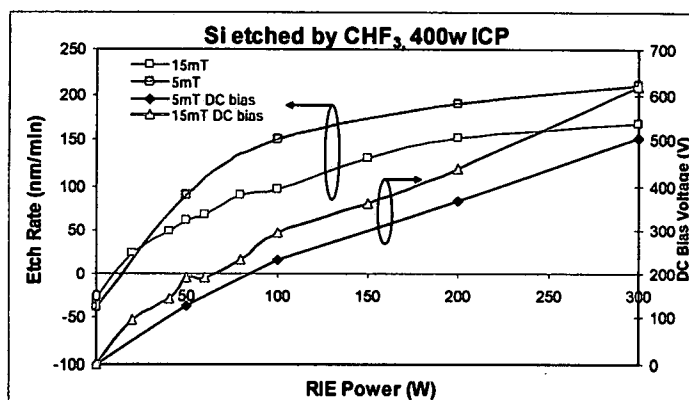


Figure 5.8: The etch rates (left) and DC bias voltage (right) of Si <100> as functions of RIE bias power in CHF_3 plasma.

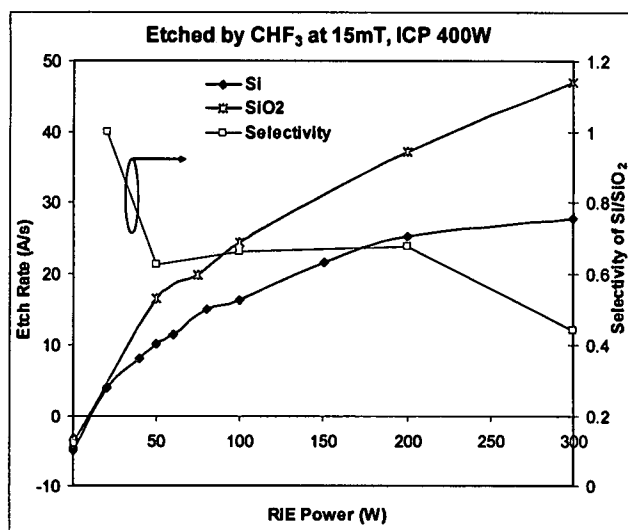


Figure 5.9: The selectivity (right) of Si over SiO_2 as a function of RIE bias power in CHF_3 plasma.

The selectivity of Si over SiO_2 in CHF_3 plasmas is 1 at the bias power of 20W. It decreases to 0.6 as the bias power increases to 50W. It stays at a constant as the bias power is between 50 to 200W, where both the etch rates of Si and SiO_2 increase in the same slope. It decreases again to 0.44 when the bias power increases from 200W to 300W, where the SiO_2 continuously increases in the same rate, but the etch rate of Si starts to saturate as shown in the right of Figure 5.9.

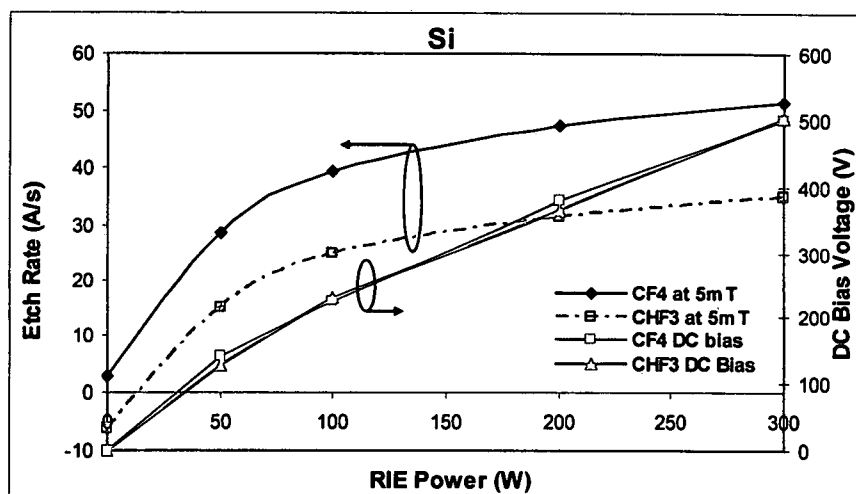


Figure 5.10: The etch rates (left) and DC bias voltage (right) of Si <100> in CHF₃ and in CF₄ plasma as functions of RIE bias power.

The DC bias voltages are almost the same in CF₄ and in CHF₃ plasma at the same bias power as shown in Figure 5.10. This means the ion flux to the substrate are the same in these two gases. The substrate experiences the same ion sputtering. The etch rate in CF₄ is higher than that in CHF₃ plasma basically because of a higher contribution of chemical etching by CF₄ than by CHF₃. Hydrogen atoms and fluorine atoms in CHF₃ form a volatile product HF, making fluorine radicals deficient. Thus results in a lower etch rate in CHF₃. The net polymer film is deposited on the substrate in CHF₃ plasma while the RIE power is lower than 15W, the ICP power is set at 400W, the operating pressure at 5mTorr and the substrate temperature at 25°C. There is no net polymer film deposit on the substrate in CF₄ plasma at the zero bias with the same operating parameters. In these two gases, the polymer deposition and polymer etch take place simultaneously. It was reported²³ that the thickness of the polymer film deposited on the substrate by CHF₃ is thicker than that by CF₄. The polymer film blocks the fluorine radicals penetrate and diffuse into the interface of the polymer film and the silicon substrate at the low bias

power. The polymer thickness in CF_4 is thinner at about 2nm, through which the fluorine radicals can penetrate and diffuse into the interface of the polymer and silicon substrate, the chemical reaction in turn takes place. So even at the zero bias, silicon is etched by CF_4 . In CHF_3 plasma, as the bias increases above a threshold, where the polymer removal rate is same as the polymer deposition rate, fluorine radicals starts to etch the silicon substrate. The silicon etch rate increases with continuously increasing of the bias power.

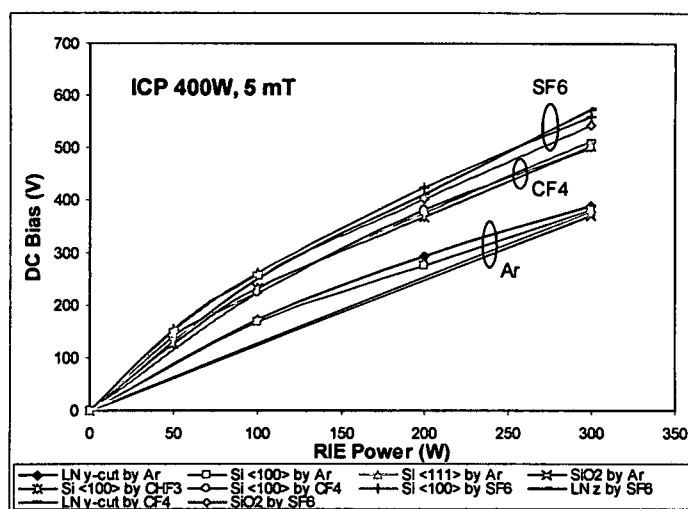


Figure 5.11: DC bias voltages of different substrates in each of SF_6 , CF_4 and argon plasma as functions of RIE bias power.

Figure 5.11 shows the DC bias voltages of different substrates ($\text{Si}<100>$, $\text{Si}<111>$, SiO_2 and Lithium Niobate) under different gases (SF_6 , CF_4 and Ar). The DC bias voltage is significantly affected by gases, and less affected by the substrates. All substrates experience about the same ion flux from the same gas, but a different ion flux from a different gas. At the same RIE power, low DC bias voltage indicates a high ionization rate and high ion flux. Therefore SF_6 has the lowest ion flux, CF_4 the intermediate and argon the highest.

5.2.2 Pressure

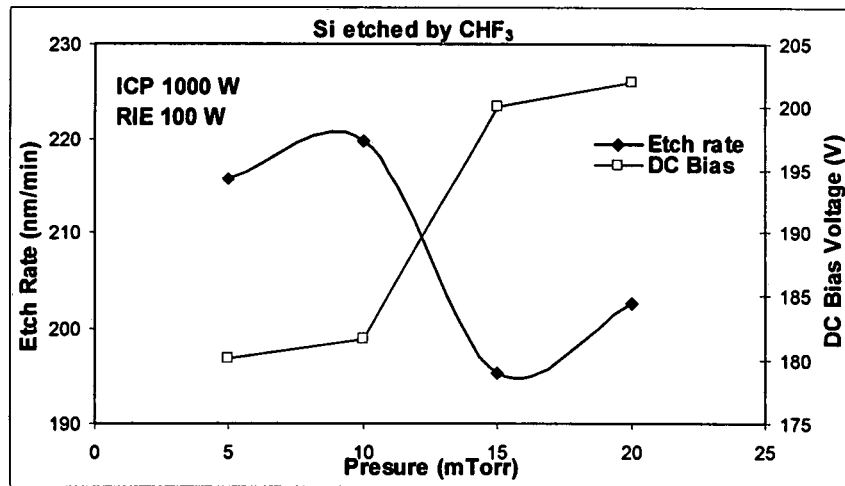


Figure 5.12: The etch rate (left) and DC bias voltages (right) of Si in CHF_3 plasma as a function of the operating pressure.

The DC bias voltage increases with the operating pressure while the ICP source power and the bias power are fixed at 1000W and 100W. Between 10mTorr to 15mTorr, a big increasing of the DC bias voltage means the ionization rate and ion flux to the substrate decreases, results in the decreasing etch rate. The free mean path decreases with the increase of the pressure. The shorter free mean path means more ion collisions, and it results in less directional ion flux to the substrate, therefore the etch rate decreases. A small increase of the DC bias voltage at the low pressure range from 5mTorr to 10mTorr and the high pressure range from 15mTorr to 20 mTorr, the etch rate increases a little bit. This is because that the mechanism of dissociation and recombination of etchant species are in competition, with dissociation being dominant at low pressure. So the etch rate increases. Also the initial increase of the etch rate with the increasing pressure is the result of an increasing F concentration and ion density that leads to a larger ion flux

towards the substrate. In the high pressure regime, the plasma density is high, this dominates which results in the increase of the etch rate.

5.2.3 ICP Source Power

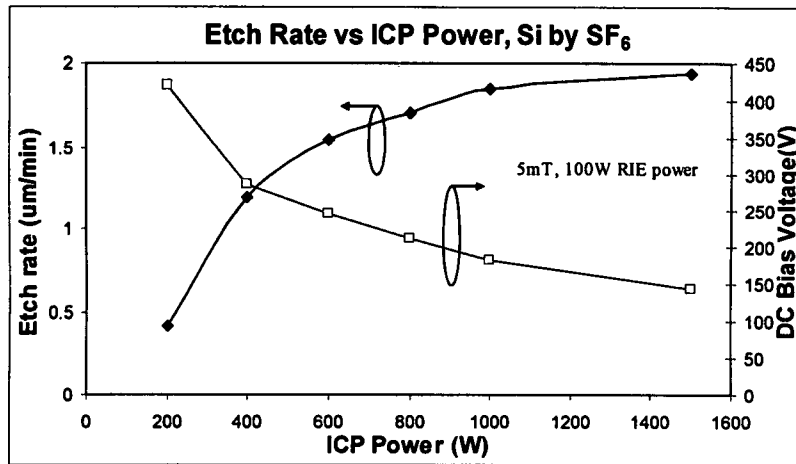


Figure 5.13: The etch rate (left) and DC bias voltage (right) of Si in SF_6 plasma as a function of ICP source power.

Figure 5.13 and Figure 5.14 show the etch rate of Si increases with the ICP source power, while the DC bias voltage decreases with the ICP source power in SF_6 and CHF_3 plasma. The RIE bias power is set at 100W, the operating pressure at 5mTorr, and the substrate temperature at 25°C . The high RF ICP source power couples its high energy to the gases and induces a high ionization rate, and results in a high ion density and high neutral radical density. The DC bias voltage decreases means the ion flux to the substrate increases, and the sheath Debye length decreases. The etch rate reaches almost $2 \mu\text{m}/\text{min}$ at the ICP power of 1500W in SF_6 plasma.

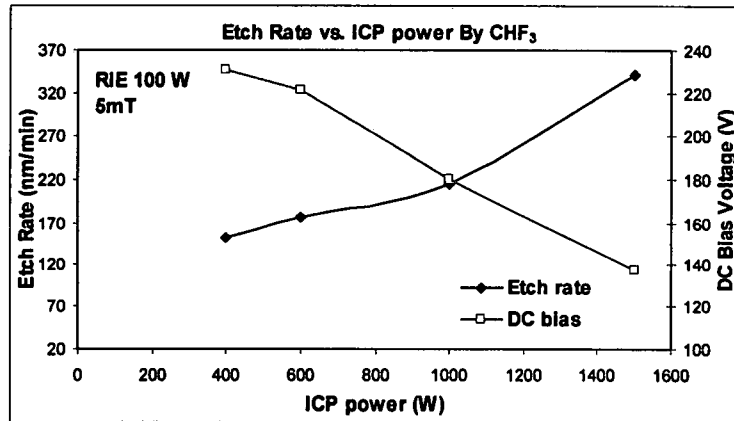


Figure 5.14: The etch rate (left) and DC bias voltage (right) of Si in CHF_3 plasma as a function of ICP source power.

5.2.4 Substrate Temperature

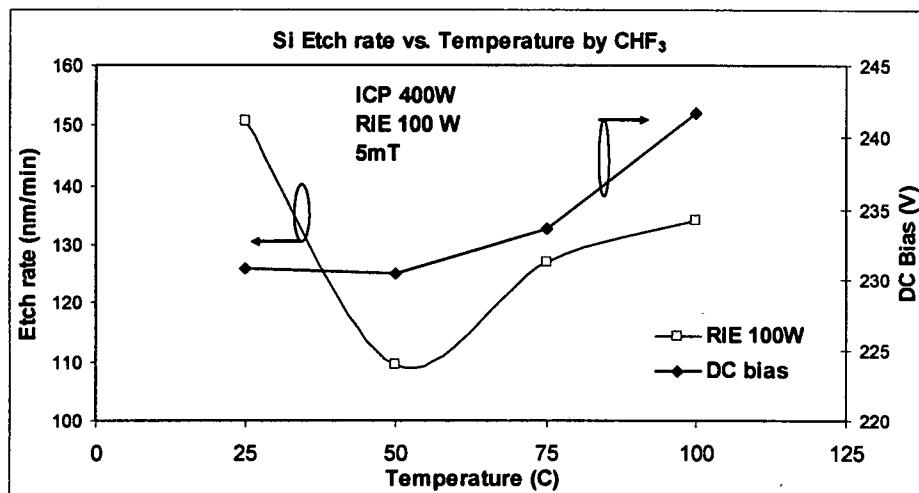


Figure 5.15: The etch rate (left) and DC bias voltage (right) of Si in CHF_3 plasma as a function of the substrate temperature.

Figure 5.15 shows that the DC bias increases with the substrate temperature, therefore less ion flux to the substrate. Ions experience more collisions and scatterings with increasing substrate temperature from 25 to 50°C, results in less directional bombardments, therefore the etch rate decreases initially. As the temperature continuously increases, the polymer deposition rate also decreases as shown in Figure

5.16, and the thickness of the polymer on the substrate becomes thinner. It makes fluorine atoms easy to penetrate to the Si substrate and react to Si atoms. The effect of a thinner polymer deposition dominates as the temperature is higher than 50°C, therefore the etch rate increases in higher temperature.

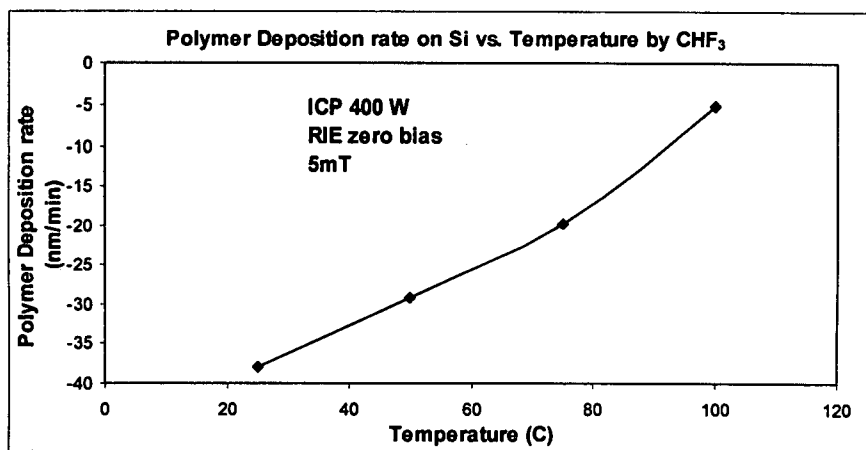


Figure 5.16: The polymer deposition rate on Si substrate in CHF_3 plasma as a function of the substrate temperature.

5.2.5 Conclusion

The etch rates of Si and Silicon dioxide in SF_6 , CHF_3 , and CF_4 plasma are fully investigated as a function of RIE bias power, operating pressure, ICP source power and substrate temperature. The polymer deposition rate in fluorocarbon gases such as CHF_3 and CF_4 are also studied. The etch rate increases with RIE bias power and ICP source power, but it increases first as the pressure increases from 5 to 10 mTorr, then decreases from 10 to 15 mTorr, then increases again from 15 mTorr to 20mTorr while the ICP power is fixed at 1000W, the RIE power at 100W.

5.3 ICP Etching of Micro-Optic Structures

Next, the ICP etching of the micro-optics structures patterned with 20um photoresist on silicon substrate were employed. Its etch rate and sidewall profile as functions of RIE bias power, operating pressure, ICP source power and etching time are investigated and characterized by SEM.

5.3.1 RIE Bias Power

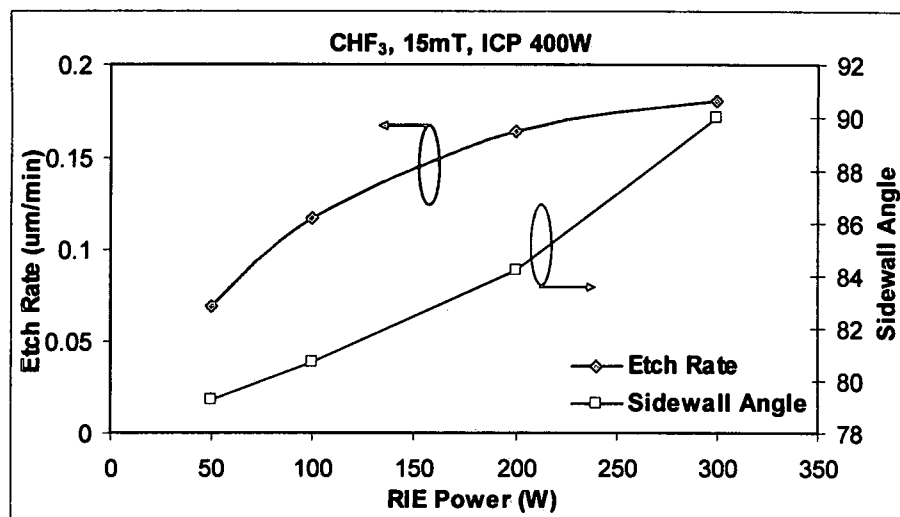


Figure 5.17: The Si etch rate (left) and the sidewall angle in CHF_3 plasma as a function of the RIE power.

In CHF_3 , the etch rate and sidewall angle increases with the RIE bias power as seen in Figure 5.17. The etch rate increase from 0.07um/min to 0.18um/min and the sidewall increases from 80° to 90° in the range of 50W to 300W RIE power. In CHF_3 gas, the fluorocarbon film passivates on all surfaces. Ions bombards on the line of the sight, remove the polymer from the bottom of trench, the fluorine atoms react with silicon to form volatile SiF_4 . The sidewall of the trench experiences no ion bombardment or very few off normal scattering ions, the sidewall surface is passivated with the polymer film.

At low bias power, fluorine atom cannot remove all polymers on the bottom, so the polymers build up on the bottom of the sidewall, the sidewall become taped. More polymers on the bottom of the trench are cleaned with the increase of RIE power, so the sidewall angle increases. The straight trench of 90° sidewall is achieved at 300W RIE power. In a mixture of 5sccm CF_4 and 50sccm Ar, the etch rate increases with the bias power, but the sidewall angle decreases from 90° to 80° as shown in Figure 5.18.

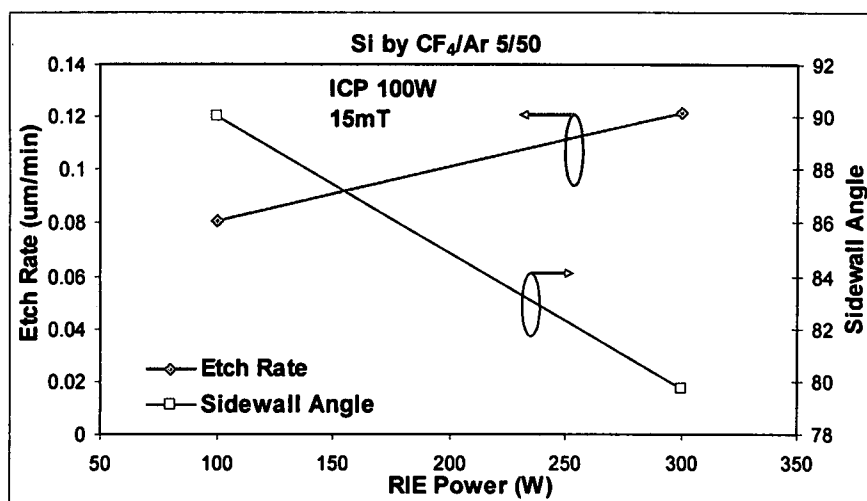


Figure 5.18: The Si etch rate (left) and the sidewall angle in CF_4/Ar plasma as a function of the RIE power.

A higher bias power of 200W at a low operating pressure of 5mTorr increases the mask sputter rate in the beginning of the process, results in the damage on the top of the trench. The etched depth is $15.3 \mu\text{m}$ for 60 minutes, the etch rate is $0.255 \mu\text{m}/\text{min}$ and the sidewall has double slopes. At a high operating pressure of 15mTorr, a low etch rate of $0.165 \mu\text{m}/\text{min}$ at the same bias power of 200W leaves no damage on the top of the trench as shown in Figure 5.19 (b). The sidewall angle is 86° . A lower bias power of 50W at the operating pressure of 15mTorr, the etched depth is $4.15 \mu\text{m}$ for 60 minutes, and there is no damage on the top of the trench. The etch rate is only $0.069 \mu\text{m}/\text{min}$. The bottom of

the trench is round due to not enough transport of species into the trenches as seen in Figure 5.19 (c).

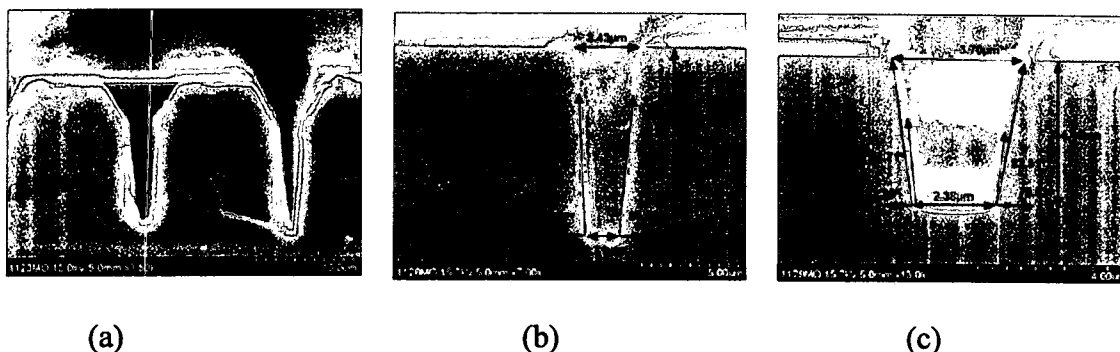


Figure 5.19: The cross-sectional view of etched micro-optic structures at (a) 5mTorr, RIE 200W, (b) 15 mTorr, RIE 200W and (c) 15mTorr, RIE 50W.

In order to avoid damage on the top of the trench and have a reasonable high etch rate, we start a low bias power to reduce the damage on the mask at the beginning of the process, and then gradually ramp up the bias power. Later on, with the increase of the aspect- ratio, increasing RF bias power maintains transport of species into the trenches. This helps to maintain overall etch rate and quality of the sidewall profile. Figure 5.20 shows the cross-sectional SEM of an etched trench with the RF bias power ramping from 50W to 200W 10 minutes for each step while the ICP power is set at 400W, and the operating pressure at 5mTorr in CHF_3 plasma. The sidewall is smooth. The etched depth is 5.9 μm , the etch rate is 0.148 $\mu\text{m}/\text{min}$ and the sidewall angle is about 85 degree. To ramp down RIE power from a higher power of 200W to a lower power of 50 W results in an asymmetrical profile as shown in Figure 5.20 (b). There is a micro trench at the bottom of one side. The etched depth is 6.43 μm for a total etching time of 40 minutes and the etch rate is 0.16 $\mu\text{m}/\text{min}$. Ramping up the bias power can reduce damage to the mask, results a smooth sidewall profile. Varying the power increment and the time can adjust the sidewall angle.

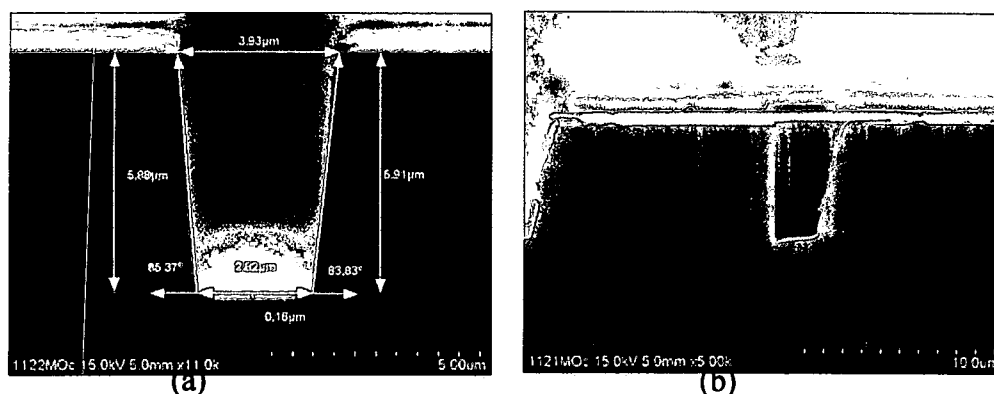


Figure 5.20: The cross-sectional view of etched micro-optic structure at 5mTorr with (a) RIE ramping up from 50W to 200W and (b) RIE ramping down from 200W to 50W.

In order to fabricate V-groove micro-optic structures, the polymers build up on the sidewalls of trenches are desired. As shown in Figure 5.21, 83° V-groove structures are achieved at 400W ICP power, 150W RIE power and 15mTorr working pressure.

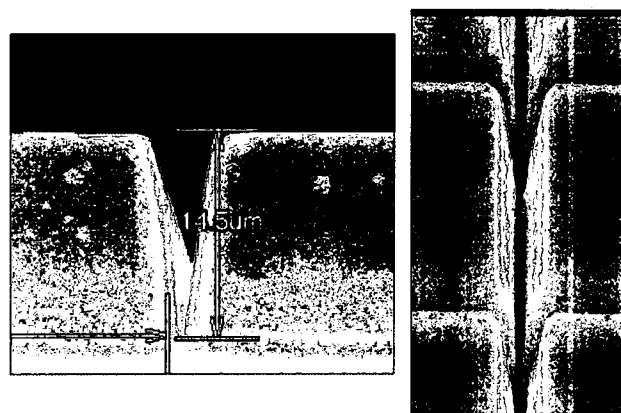


Figure 5.21: Micro-Optic V-groove structures.

5.3.2 Etching Time

To increase etching time from 20 to 40 minutes, the etch rate increases first while the sidewall angle stays at a constant of 84° , and then the etch rate decreases after 40 minutes while the sidewall increases to 90° .

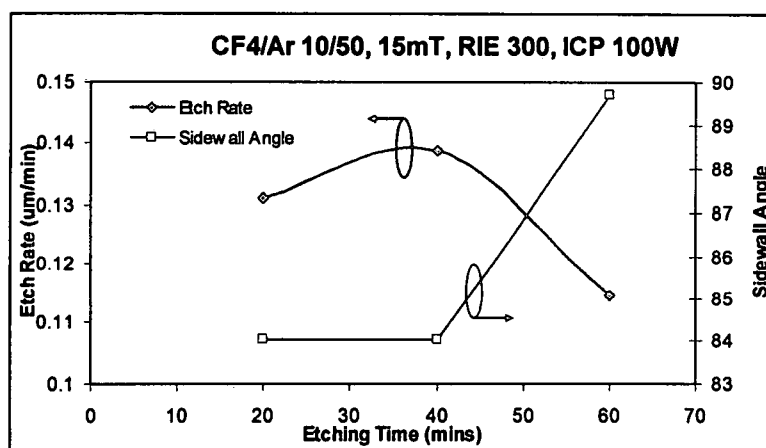


Figure 5.22: The Si etch rate (left) and the sidewall angle in CF₄/Ar 10/50 plasma as a function of the etching time.

5.3.3 Ratio of Gas Flow Rates

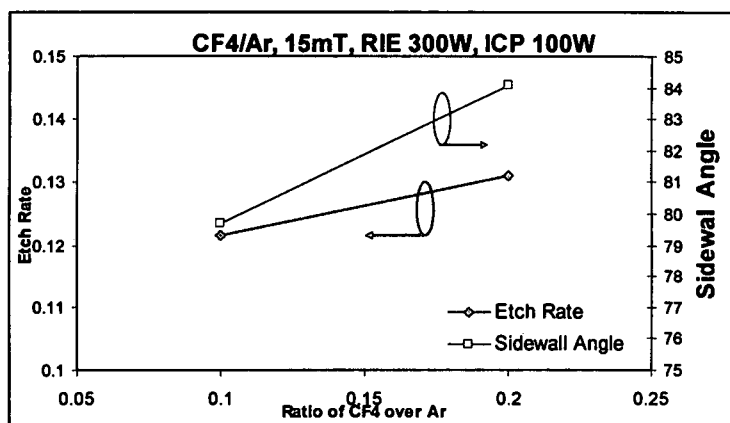


Figure 5.23: The Si etch rate (left) and the sidewall angle in CF₄/Ar plasma as a function of the ratio of CF₄ flow rate over Argon flow rate.

To increase ratio of CF₄ flow rate over Argon flow rate, both etch rate and sidewall angle increase. Since argon is an inert gas, its contribution to the etching is via sputtering. The density of fluorine increases with the ratio of CF₄ flow rate over Argon flow rate, so the etch rate increases. The high etch rate removes the polymer buildup, therefore the sidewall angle increases.

5.3.4 Pressure

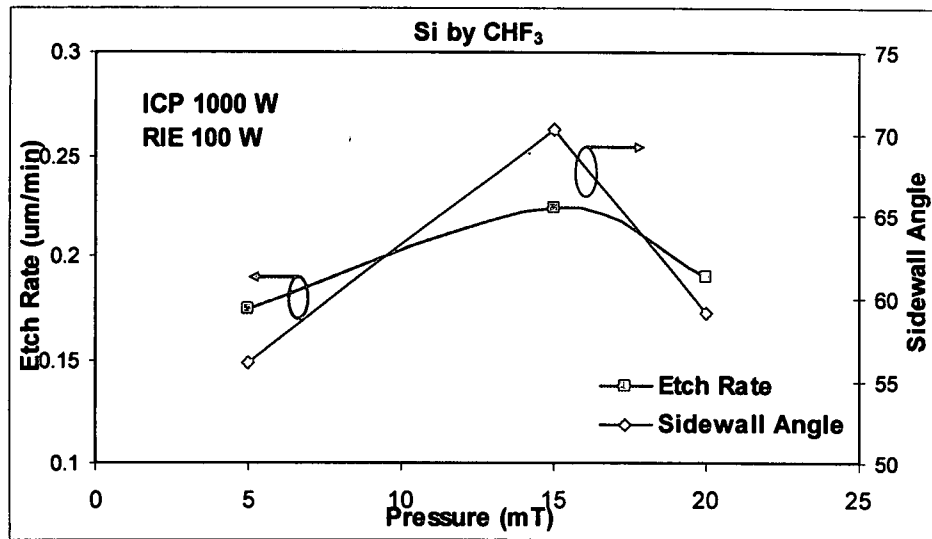


Figure 5.24: The Si etch rate (left) and the sidewall angle (right) in CHF₃ plasma as a function of the operating pressure.

Both of etch rate and sidewall angle increase initially when the pressure increases from 5 to 15mT, then they decrease when the pressure increases further from 15mT to 20mT. At a lower pressure, the ion current density is higher. Gas molecules at low pressure collide less frequently and hence, are inherently more directional on the material etched. At a higher pressure, the etch rate is smaller. The increased deposition of polymers takes place on the surface and the sidewall. Simultaneously, the ion energy decreases due to the reduced mean free path of gas molecules. Therefore the passivation layer cannot be completely removed during the etching step. This results in the sloped sidewall with narrower trench on the bottom due to the net deposition buildup.

5.3.5 ICP Source Power

To increase ICP power, the etch rate decreases a little from 100W to 150W, and then increases from 150W to 200W, correspondingly the sidewall angle decreases from 80° to 71° when ICP changes from 150W to 200W.

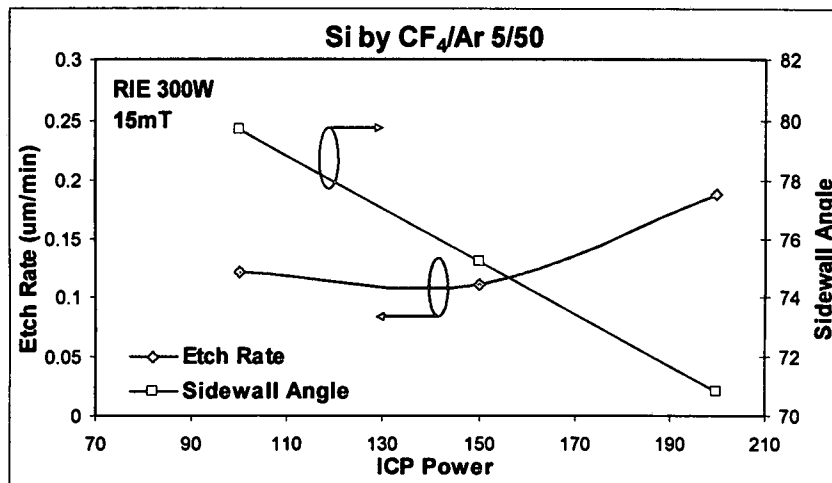


Figure 5.25: The Si etch rate (left) and the sidewall angle in CF₄/Ar 5/50 plasma as a function of the ICP power. The operating pressure is set at 15mTorr and RIE at 300W.

5.4 Selectivity of Silicon Over Mask Materials

Etch rates of silicon and the masks are presented in Figure 5.25 (a) and (b). The mask materials used are photoresist, Al₂O₃ and Cr. The selectivity of Si over mask materials is shown in Figure 5.25 (c). Table III lists the operating parameters of the corresponding processes. The selectivity is extremely high for silicon over Al₂O₃ and Cr at lower RIE bias power due to reduced mask sputtering at the lower bias power.

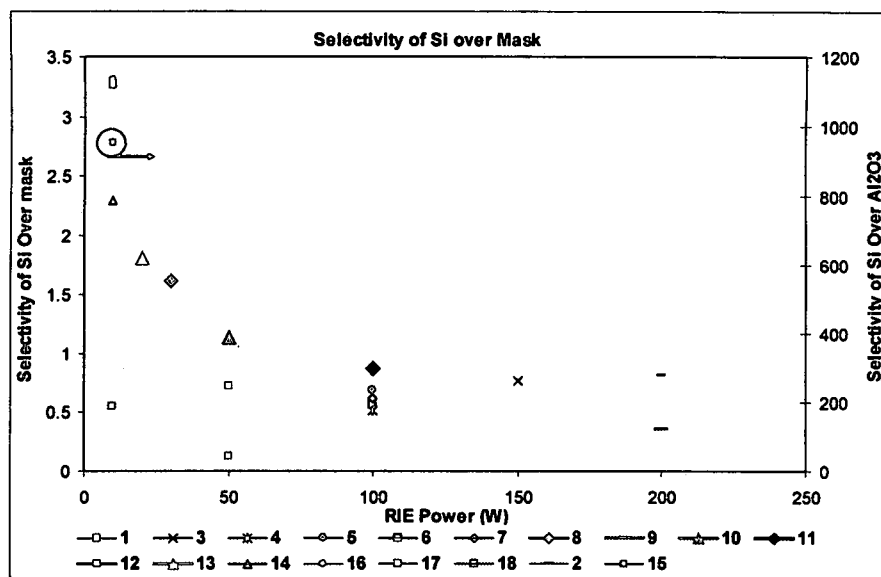
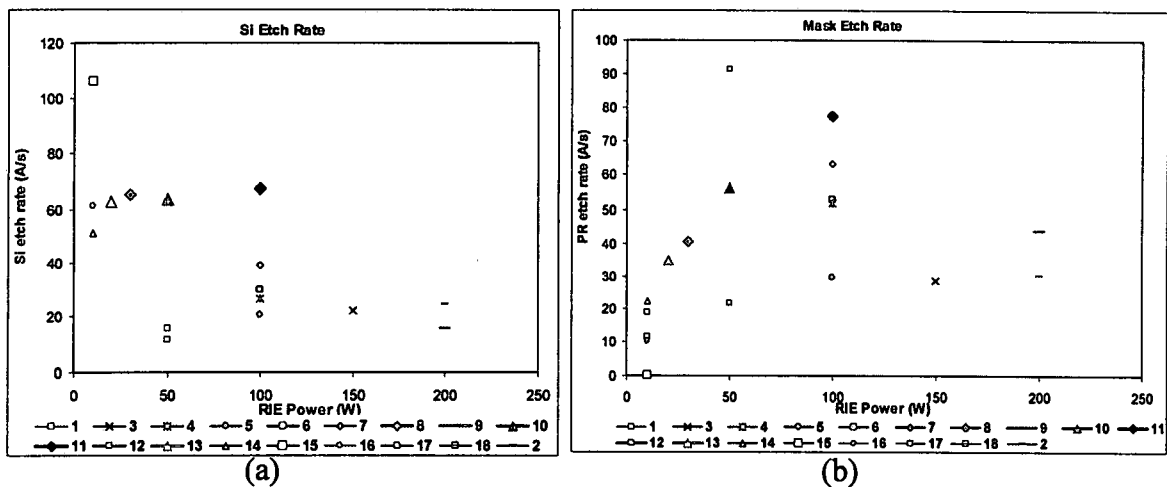


Figure 5.26: (a) The Si etch rates, (b) the etch rate of mask materials and (c) the selectivity of Si over the mask materials as a function of the RIE power.

Table 5.1: Processing parameters and the selectivity of Si over Masks

| Run # | Gases | Pressure | RIE | ICP | time | Si ER | Mask ER | Selectivity | Mask |
|-------|-----------------------------------|----------|-----|------|------|-------|---------|-------------|--------------------------------|
| | CHF ₃ /SF ₆ | mT | W | W | s | A/s | A/s | Si/Mask | |
| 1 | 25/0 | 5 | 50 | 400 | 3600 | 15.6 | 21.6 | 0.72 | PR |
| 2 | 25/0 | 5 | 200 | 400 | 2400 | 24.5 | 30.2 | 0.81 | PR |
| 3 | 25/0 | 15 | 150 | 600 | 3900 | 22.0 | 28.8 | 0.76 | PR |
| 4 | 25/0 | 5 | 100 | 600 | 600 | 26.7 | 51.8 | 0.51 | PR |
| 5 | 25/0 | 15 | 100 | 400 | 3600 | 20.4 | 29.7 | 0.69 | PR |
| 6 | 25/0 | 5 | 100 | 1000 | 2700 | 29.8 | 52.7 | 0.57 | PR |
| 7 | 25/0 | 5 | 100 | 600 | 2400 | 39.3 | 63.3 | 0.62 | PR |
| 8 | 50/25 | 5 | 30 | 800 | 3600 | 65.0 | 40.4 | 1.61 | PR |
| 9 | 25/0 | 5 | 200 | 800 | 1800 | 15.6 | 43.6 | 0.36 | PR |
| 10 | 50/25 | 5 | 50 | 800 | 2400 | 63.3 | 56.0 | 1.13 | PR |
| 11 | 50/25 | 5 | 100 | 800 | 2400 | 67.1 | 77.6 | 0.86 | PR |
| 12 | 25/0 | 5 | 50 | 800 | 1800 | 11.6 | 91.2 | 0.13 | PR |
| 13 | 50/25 | 5 | 20 | 800 | 3600 | 62.8 | 34.8 | 1.81 | PR |
| 14 | 50/25 | 5 | 10 | 800 | 3600 | 51.1 | 22.2 | 2.30 | PR |
| 15 | 50/25 | 5 | 10 | 800 | 1800 | 105.9 | 0.1 | 953.5 | Al ₂ O ₃ |
| 16 | 60/15 | 5 | 10 | 800 | 3600 | 33.3 | 10.1 | 3.31 | PR |
| 17 | 40/35 | 5 | 10 | 800 | 3600 | 60.8 | 18.7 | 3.25 | PR |
| 18 | 70/5 | 5 | 10 | 800 | 3600 | 6.1 | 11.1 | 0.55 | PR |
| 19 | 70/5 | 5 | 10 | 800 | 3600 | 10.1 | 0.2 | 48.4 | Al ₂ O ₃ |
| 20 | 50/25 | 5 | 10 | 800 | 3600 | 112.2 | 0.02 | 6733 | Cr |

5.5 Bosch Process

The Bosch process consists of a sequence of alternating etch and passivation cycles in Figure 5.26. In this work, the gases for etch and passivation cycles are SF₆ and CHF₃, respectively. In the passivation phase a fluorocarbon polymer deposits over all surfaces of the wafer and trenches in Figure 5.10 (a). During each etch cycle, the polymer film is removed from the bottom of the etched features with the assistance of a directional ion energy in Figure 5.10 (b). The rest of the etch cycle is a short isotropic etch of the exposed Si in Figure 5.10 (c). As the vertical etch rate is much faster than the lateral etch rate, highly anisotropic profiles can be achieved. The process is suitable to fabricate various MEMS devices, deep micro fluid devices and high aspect ratio applications.

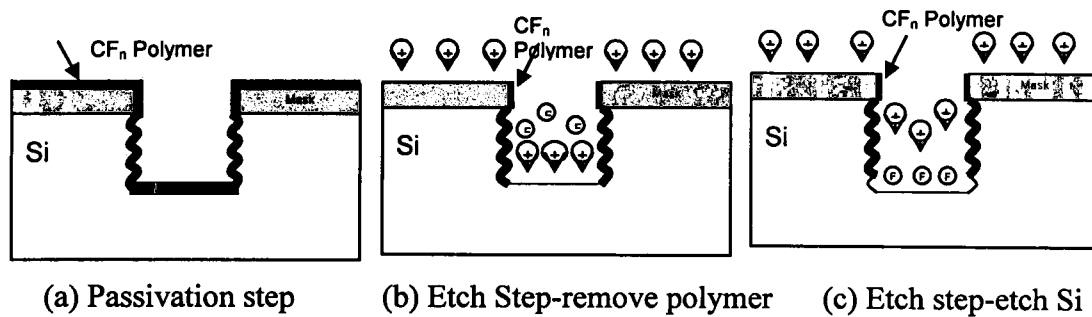


Figure 5.27: Schematic diagram of Bosch process

The masks we used for the Bosch processes are 5000A thick of Al_2O_3 film and 5500A thick of Cr film deposited with E-beam evaporator by using the lift off method mentioned in Chapter 4.1.2 and 20 μm thick of positive photoresist and 7 μm thick of SU8 mask using photo lithography described in Chapter 4.1.1.

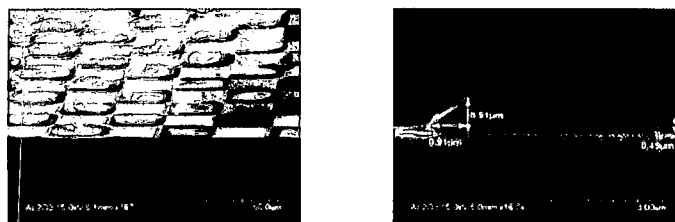


Figure 5.28: The SEM photograph of (a) a top view and a cross-sectional view of an Al_2O_3 mask with the thickness of 5000A.

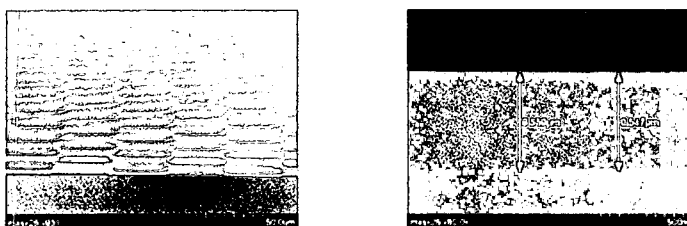


Figure 5.29: The SEM photograph of (a) a top view and (b) a cross-sectional view of a Cr mask with the thickness of 5500A.

Table 5.2: Bosch processing parameters

| Run | Passivation | | | | | Etch | | | | | n cycles | Depth um | Vertical nm | Lateral nm |
|-----|-------------------------|---------|----------|----------|-----------|--------------------------------|---------|----------|----------|-----------|-------------|-------------|----------------|---------------|
| | Gas CHF ₃ | P mT | ICP W | RIE W | Time s | Gas SF ₆ / Ar | P mT | ICP W | RIE W | Time s | | | | |
| B1 | 25 | 24 | 800 | 2 | 120 | 50/0 | 12 | 800 | 150 | 15 | 15 | 6.27 | 500 | 200 |
| B2 | 25 | 24 | 800 | 2 | 90 | 50/0 | 12 | 800 | 50 | 30 | 40 | 29.4 | 660 | 170 |
| B3 | 25 | 24 | 800 | 2 | 90 | 50/0 | 12 | 800 | 50 | 30 | 10 | 6.76 | 725 | 240 |
| B4 | 50 | 15 | 800 | 2 | 120 | 50/0 | 5 | 800 | 50 | 45 | 10 | 4.52 | 520 | 200 |
| B5 | 25 | 24 | 800 | 2 | 120 | 50/0 | 12 | 800 | 100 | 45 | 40 | 23.6 | | |
| B6 | 25 | 12 | 800 | 2 | 10 | 40/10 | 12 | 800 | 50 | 8 | 20 | 6 | | <28 |

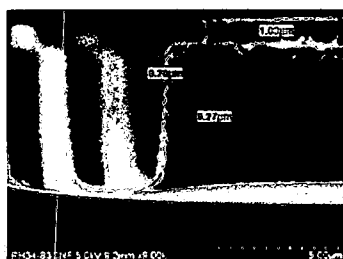


Figure 5.30: The SEM photograph of a cross-sectional view Bosch process run B1 with a SU8 mask.

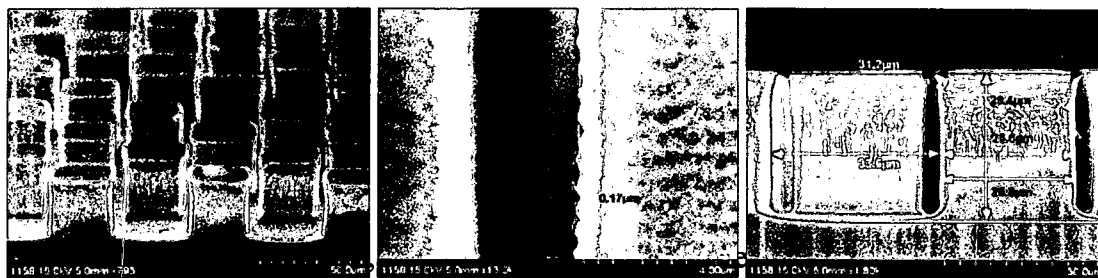


Figure 5.31: The SEM photograph of a top view and two cross-sectional views of Bosch process run B2.

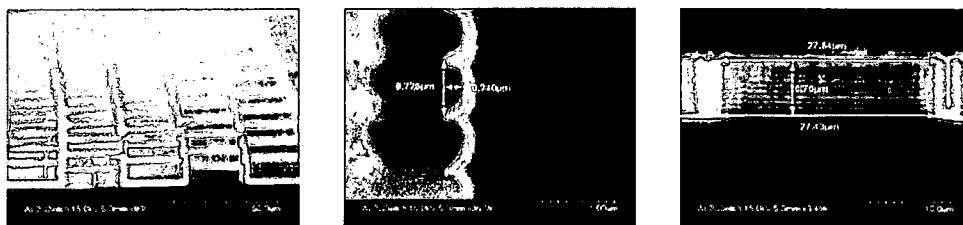


Figure 5.32: The SEM photograph of a top view and two cross-sectional views of Bosch process run B3 with an Al₂O₃ mask.

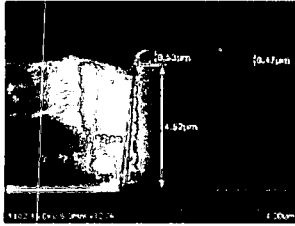


Figure 5.33: The SEM photograph of a cross-sectional view of Bosch process run B4 with a Cr mask.

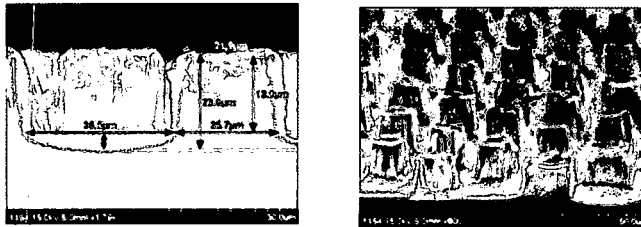


Figure 5.34: The SEM photograph of a top view and a cross-sectional view of Bosch process run B5 with a Cr mask.

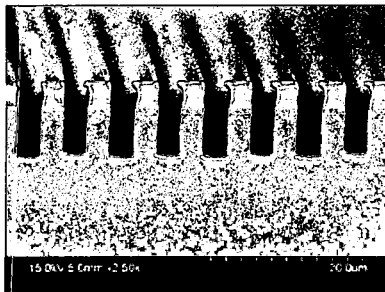


Figure 5.35: The SEM photograph of a top view and a cross-sectional view of Bosch process run B6 with a PR mask.

From Run 1 to Run 4, the scallop on the sidewall can be seen. Keeping the operating pressure same for deposition step and etching step can make the switching fast. So we chose a short deposition time of 10s and a short etching time of 8s in Run B6. This process greatly smoothes the sidewall surface. Actually the scallop on the sidewall is not observed. A very thin layer of polymer deposits on all of the surfaces during the deposition step, only the bottom polymer is removed by ion bombardment. The fluorine can etch silicon on the bottom very fast while the polymer on the sidewall is not removed.

The Cr mask was eroded by the high RIE power of 100W in run B5 and the structure was damaged. The mask is sputtered by ion bombardment, and the selectivity decrease greatly with the increase of RIE power. But with ICP technique, we can choose high ICP source power and low bias power to reduce the damage on the mask and structures.

5.6 Conclusions

The profiles from v-groove to straight sidewall are realized by adjusting gas composition, ICP power, pressure, bias power and etching time. The processes of one-step and multiple steps as well as Bosch process of alternating deposition and etching steps have been explored to achieve a wide range of etch rates, etch selectivity and sidewall angles. Decreasing bias power can increase the polymer build up on the sides of bottom trench, therefore results a V-groove profile.

CHAPTER VI

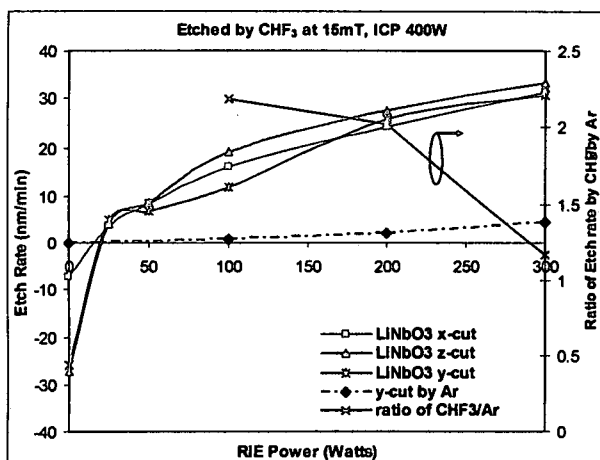
LITHIUM NIOBATE ICP ETCHING

In this chapter, the results of the ICP etching of x-cut, y- cut and z-cut of the blank LiNbO_3 wafers, z-cut LiNbO_3 gratings and z-cut LiNbO_3 ridge waveguides that were fusion bonded to LiTaO_3 substrates are presented.

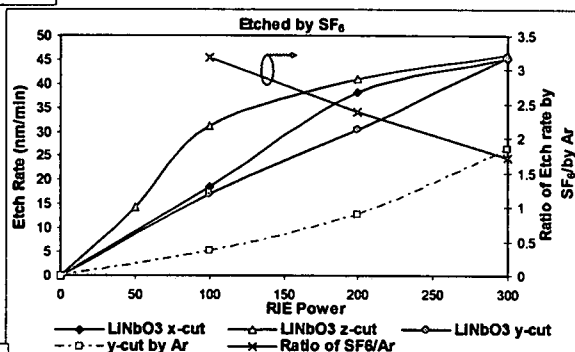
6.1 ICP Etching of a Blank LiNbO_3 Wafer

Ambios stylus profiler was used to measure the etched depth of the blank LiNbO_3 sample. The etch rates of LiNbO_3 wafer in x-cut, y- cut and z-cut as a function of RIE power are shown in Figure 6.1 in (a) CHF_3 plasma, the operating pressure of 15 mTorr, (b) SF_6 plasma, at 5 mTorr and (c) CF_4 plasma at 5mTorr at 400W ICP source power. The etch rates are compared with the etch rate by argon plasma. The etch rate is 2 time higher than the etch rate by argon gas, which is purely physical sputtering. The contribution from the chemical reaction is very small comparing with that of silicon etches by the same gas at the same processing conditions. The etch rate increases with the RIE bias power, which increases the ion energy to enhance ion bombardment on the substrate. At zero bias or below 20 Watts, the negative etch rate by CHF_3 means there is a net accumulation of polymer deposition on LiNbO_3 . The deposition rate is lower for x-cut

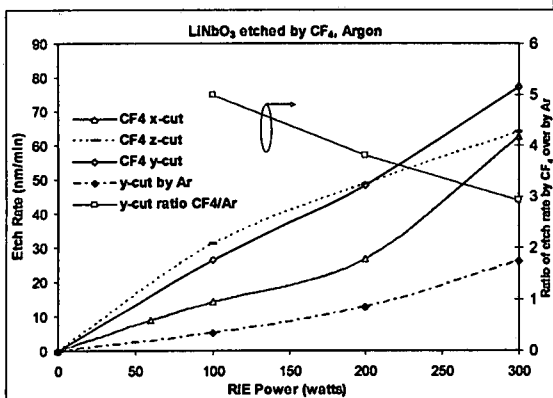
LiNbO_3 by 74% than those of other two cuts at zero bias power. At a high bias power of 300 Watts, CF_4 gives the highest etch rate, SF_6 the intermediate etch rate and CHF_3 the lowest etch rate. But they are all higher than the etch rate by inert gas.



(a)



(c)



(c)

Figure 6.1: The etch rates of LiNbO_3 as a function of RIE power in (a) CHF_3 , at 15mTorr (b) SF_6 at 5mTorr and (c) CF_4 plasma at 5mTorr while the ICP power was set to 400 W.

Lithium niobate is a crystal material which is hard to etch. Figure 6.2 (a), (b) and (c) show that the etch rate ratio of LiNbO_3 by CHF_3 over argon is 1.2 to 2.2, by SF_6 over argon is 1.7 to 3.2, and 3 to 5 by CF_4 over argon.

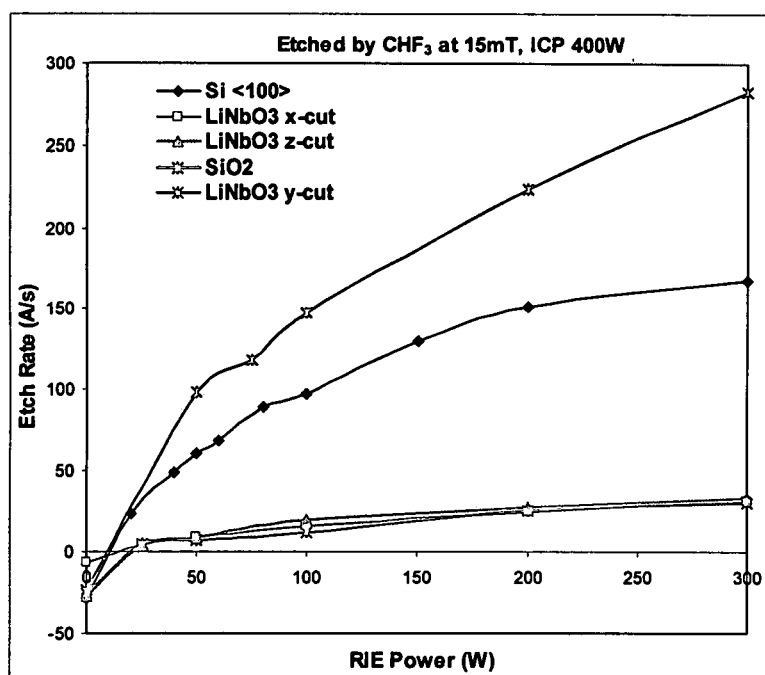


Figure 6.2: The etch rates of Si, SiO_2 and LiNbO_3 as a function of RIE power in CHF_3 plasma while the ICP power was set to 400 W, the operating pressure at 5mTorr.

Figure 6.2 shows the etch rates of LiNbO_3 in all three cuts are much smaller comparing to those of Si and SiO_2 in CHF_3 plasma when the bias power is between 50 and 300 Watts. The etch rate increases and DC bias voltage decreases with the ICP power as seen in figure 6.3. The polymer deposition rate on LiNbO_3 at zero bias in CHF_3 plasma is about same as that on silicon. The activation energy for etching to take place is higher than that of silicon. It was observed that the polymer on LiNbO_3 substrate can be easily removed by acetone. The formation of lithium fluoride (LiF) compounds during the etching process is relatively nonvolatile⁵⁵, but NbF is volatile.

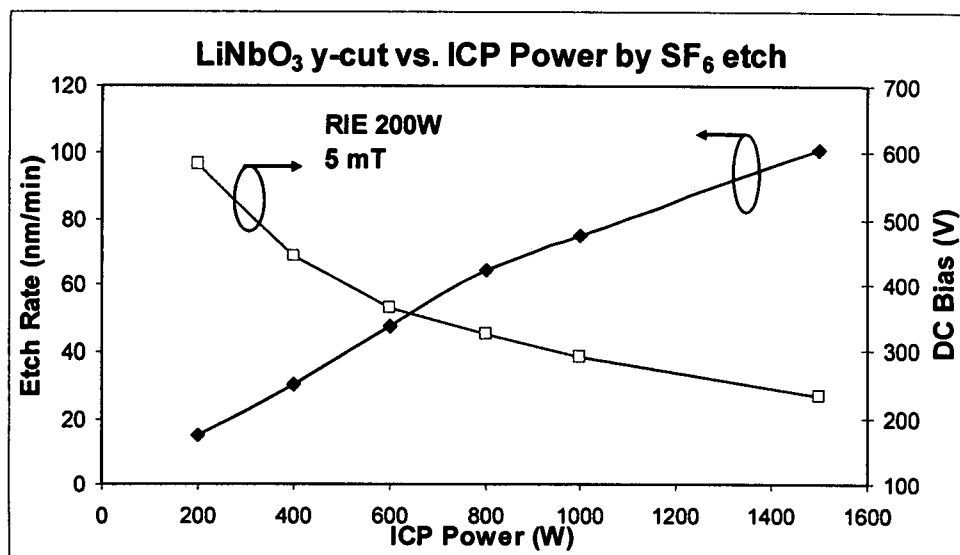


Figure 6.3: The etch rate (left) and DC bias voltage (right) of y-cut LiNbO₃ as a function of ICP source power in SF₆.

6.2 ICP Etching of LiNbO₃ Gratings

A stylus profilometer was used to measure etched depth. It is an easy and fast method to measure depth, but it is limited by the stylus tip angle, so it is not suitable for measuring a deep trenched structure with high aspect ratios or to get an accurate sidewall profile. Atomic Force Microscopy (AFM) of Park System NSOM and White Light Interferometer (WLI) of Veeco Wyko NT9100 were used to measure the etched depth and profile of LiNbO₃ gratings. One of the advantages of using a white light interferometer is that there is no need to cleave samples to get a profile view, which can cause damage to the samples for a SEM cross-sectional view. It is especially good for LiNbO₃ samples, since LiNbO₃ wafer is not easy to scribe like Si and a special dicing saw is needed to cut LiNbO₃ for a SEM cross-sectional view. Furthermore, LiNbO₃ can not be imaged on an SEM without a conductive coating. The WLI of Veeco Wyko NT 9100 is also very fast to have one scan to get all images in 1D line profile, 2D and 3D.

The LiNbO_3 samples used before etching in the SEM view of figure 6.5 were patterned with a photoresist of $8.5\ \mu\text{m}$ and hard baked. The period of the gratings is $29\ \mu\text{m}$ and the linewidth is $14.5\ \mu\text{m}$. The etching parameters, etch rates, selectivity and etched sidewall angle are listed in Table I.

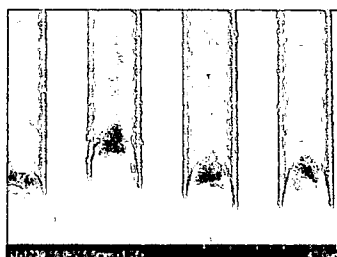


Figure 6.4: The SEM photography of patterned photoresist on the substrate LiNbO_3 before etching.

Table 6.1: Processing parameters of LiNbO_3 ICP etching.

| | | | | | | | | AFM | profiler | profiler | WLI | | | |
|-----|----------------|---------|-----|-----|-------|--------|------|-------------------|----------|----------|--------|----------|----------|-------|
| | CHF_3 | | | | | | | | depth | Depth | | | | Side |
| | /SF6 | P | RIE | ICP | DC | time | temp | depth | before | after | depth | | | wall |
| Run | sccm | (mTorr) | W | W | V | (mins) | C | (μm) | clean | clean | after | (nm/min) | (nm/min) | Angle |
| 1 | 25/0 | 5 | 100 | 800 | 176.3 | 40 | 25 | 1.786 | | 2 | 2.3942 | 50 | | 81 |
| 2 | 25/0 | 5 | 100 | 400 | 230 | 60 | 25 | 1.452 | | 1.654 | 1.6971 | 27.5667 | | 83.5 |
| 3 | 25/0 | 5 | 100 | 400 | 243.9 | 40 | 25 | 3.006 | 3.95 | 1.4 | 1.3829 | 35 | 148.75 | 80.5 |
| 4 | 25/0 | 5 | 100 | 400 | 250.8 | 40 | 15 | 2.852 | 3.77 | 1.336 | | 33.4 | 151.65 | |
| 5 | 50/25 | 15 | 50 | 800 | 161.2 | 40 | 25 | | | | 0.4 | | | |

Figure 6.6 shows the images of the gratings at the process of run 1 at an ICP source power of 800 Watts. The top surface of the gratings is flat after the photoresist removal. The etch rate of LiNbO_3 is $50\ \text{nm/min}$, and the sidewall angle is 81° .

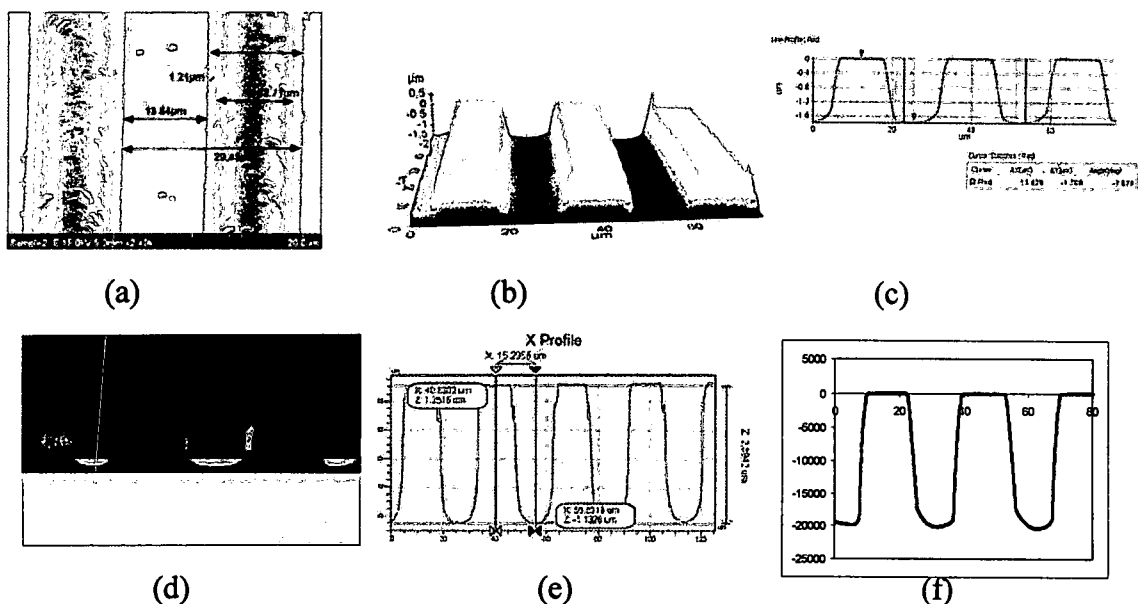


Figure 6.5: Before the sample (run 1) was cleaned by acetone (a) SEM, after the sample was cleaned by acetone (b) AFM 3D and (c) AFM line profile, (d) WLI cross-sectional view, (e) WLI line profile and (f) line profile by Ambios stylus profiler.

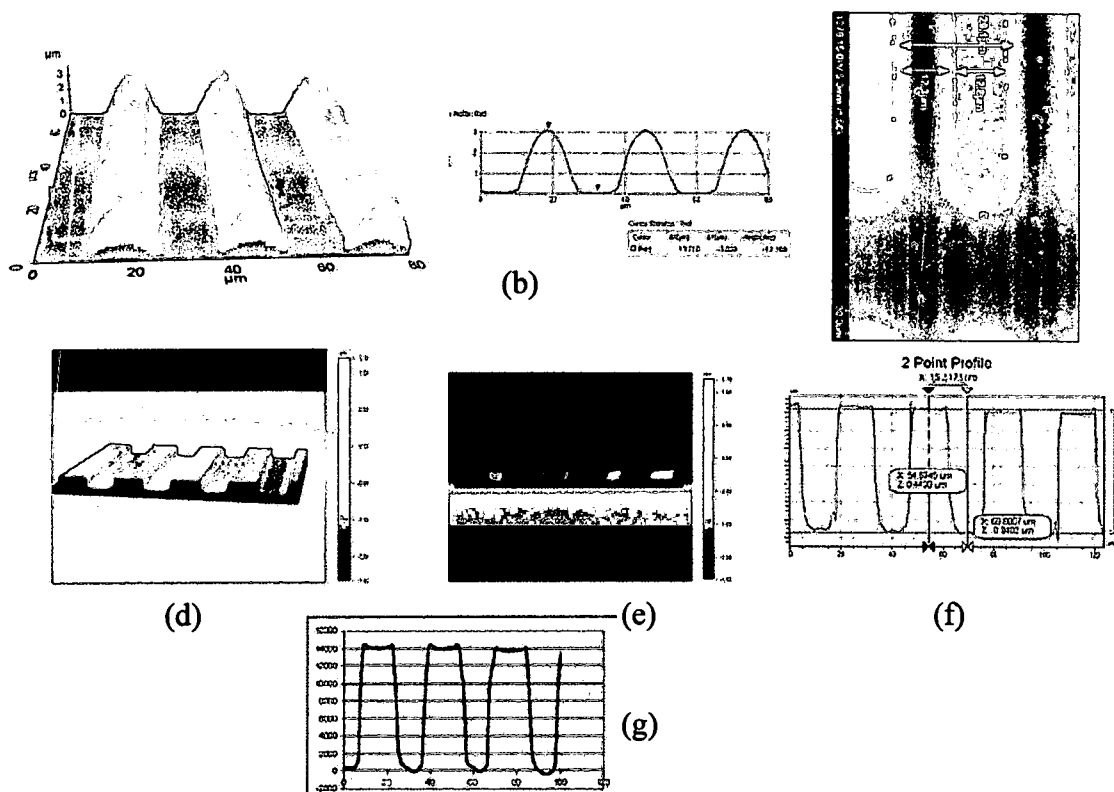


Figure 6.6: The sample (run 3) before PR removal (a) AFM 3D, (b) AFM line profile and (c) SEM. After PR removal (d) WLI 3D view, (e) WLI cross section view, (f) WLI line profile and (g) Ambios profiler.

The run 3 is the same process as the run 1 except at a lower ICP source power of 400 Watts. The etch rate of LiNbO_3 is 35 nm/min, the etch rate of the photoresist is 148.8 nm/min, and the selectivity of PR over LiNbO_3 is 4.25. The sidewall angle is 80.5° as shown in Figure 6.6, is about the same angle as from run 1.

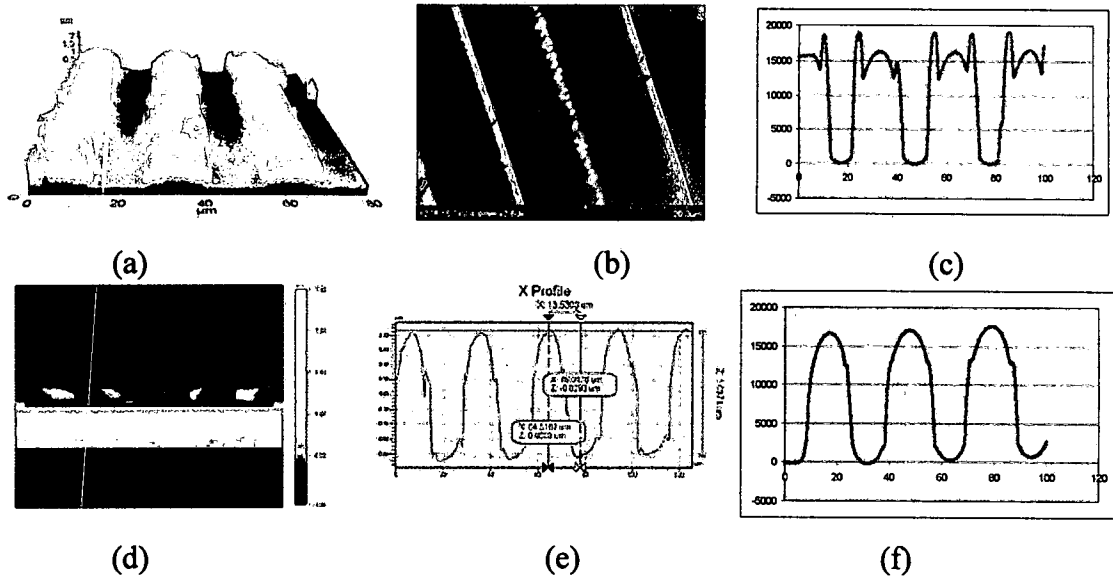


Figure 6.7: The sample (run 2) before PR removal (a) AFM (b) SEM (c) Profiler line profile, after PR removal (d) 3D by WLI, (e) WLI lineprofile and (f) line profile by Ambios profiler.

The run 2 is the same process as the run 3, except the 20 minutes longer etching time. The polymer film is easily seen on the sidewall in Figure 6.7. After an acetone clean, the photoresist and the polymer on the sidewall are removed as shown in Figure 6.7 (e) and (f). The top surface has a round surface, since the photoresist was all gone before the process was finished for the run 2 of 60 minutes process; therefore the round shape of the photoresist has been transferred to the top surface of the gratings.

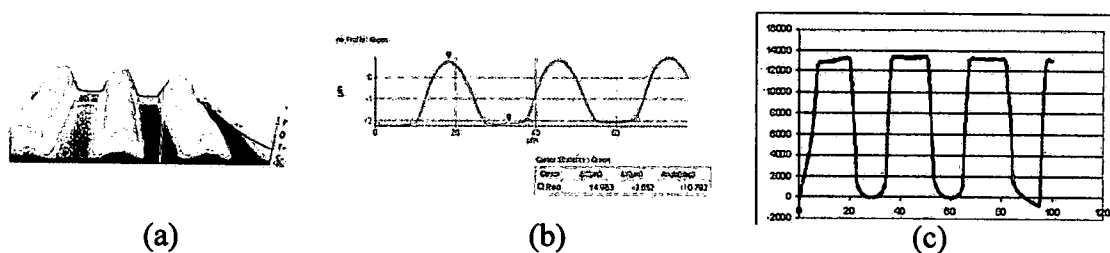


Figure 6.8: The sample (run 4) before PR removal (a) AFM, (b) SEM, and after PR removal (c) Profiler line profile.

The run 4 is the same process as the run 3 except the substrate is helium cooled at 15°C . The profile is presented in Figure 6.8

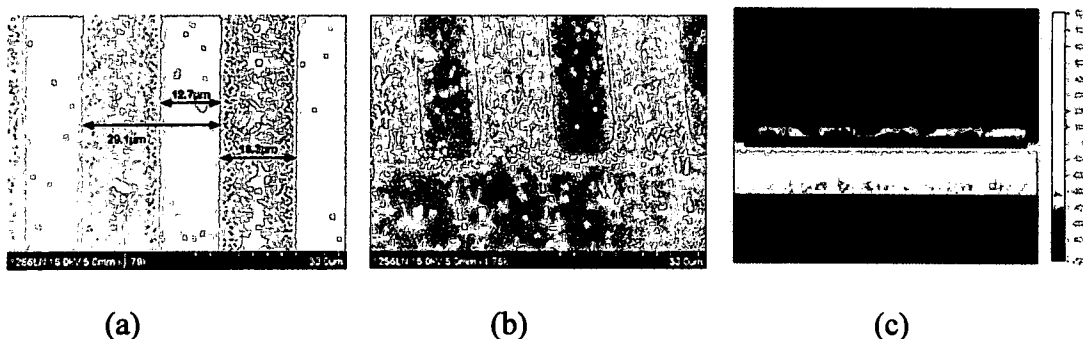


Figure 6.9: The sample (run 5) was etched with SF_6/CHF_3 before PR removal (a) SEM and (b) SEM, and after PR removal by (c) White light interferometer.

The re-deposition of etched byproduct is observed at a higher ICP source power of 800W, a RIE bias power of 50W, a operating pressure of 15 mTorr with a mixed chemistry of 50sccm CHF_3 and 25sccm SF_6 as presented in Figure 6.9. The surface is very rough with a lot of re-deposition product of LiF as micro-masks. After an acetone clean the etching profile was not uniform as shown in Figure 6.9 (c) in the cross-sectional view from the white light interferometer. The etched depth is only $0.4\mu\text{m}$ for 40 minute etching. It is believed that more fluorine from adding SF_6 causes large size grain particles

of LiF absorbed on the surface as the LiF precipitates were found to be crystalline in the CF_4 etching, while amorphous in the CHF_3 etching⁵⁴.

The optimized process is run 1. The sidewall angle is about 81° , and the etched depth is about $2.4\text{ }\mu\text{m}$.

6.3 ICP Etching of LiNbO_3 Ridge Waveguides

The LiNbO_3 wafer is patterned with $8.5\text{ }\mu\text{m}$ photoresist and fusion bonded to a LiTaO_3 substrate.

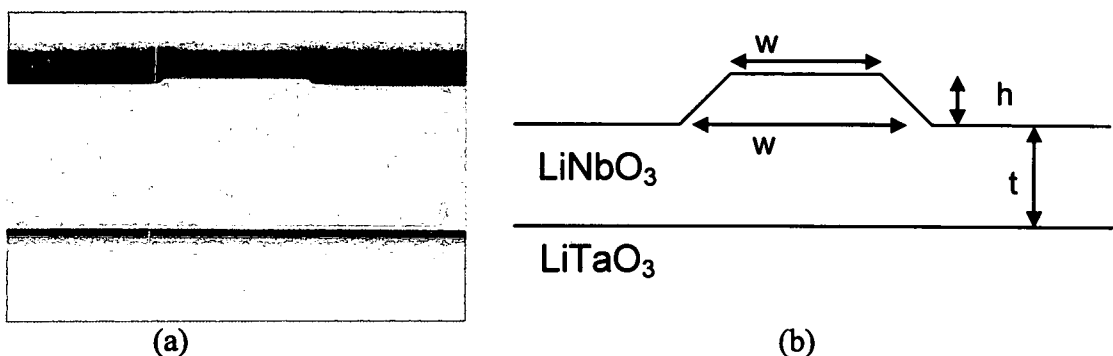


Figure 6.10: LiNbO_3 ridge waveguide (a) the SEM cross-sectional view and (b) the schematic graph of the ridge waveguide.

Figure 6.10 shows the ICP etched LiNbO_3 ridge waveguide which was bonded to a LiTaO_3 substrate. Table II shows the nominal width of ridge waveguides, the etched height h , the thickness t of LiNbO_3 , the top width w_1 and the bottom width w_2 for the etching time of 60 minutes, at the ICP power of 400W, the RIE bias power of 100W, and the operating pressure of 5mTorr. The substrate is helium cooled at 25°C . Figure 6.44 is a plot of the sidewall angle as a function of the nominal width of the ridge waveguides. The etched depth is $0.8\text{ }\mu\text{m}$. The etch rate of LiNbO_3 , which was bounded on a LiTaO_3 substrate is lower comparing with that of LiNbO_3 substrate etched at the same etching

condition. The sidewall angles are small, only 40 degree at the maximum for small nominal width at 10 μm . It decreases further to a minimum 25 degree at nominal width of 20 μm , and then it decreases to 30 degree as the nominal width increases. In order to increase the sidewall angle, we can add Ar gas, and decrease CHF_3 gas, therefore decrease the sidewall polymer deposition. The sidewall angle for a nominal width of 15 μm is 37°, is much smaller comparing with the sidewall angle at 83° for the gratings of LiNbO_3 substrate. The reason is that LiTaO_3 has an even higher pyroelectricity than that of LiNbO_3 , therefore inducing a higher temperature on the substrate by ion bombardments, which results in more ion scattering, therefore a lower etch rate and a shallow sidewall angle.

Table 6.2: The sidewall angle of ICP etching LiNbO_3 ridge waveguides

| Waveguide by nominal width (μm) | h (μm) | t (μm) | w1 (μm) | w2 (μm) | Sidewall angle (deg) |
|--|---------------------|---------------------|----------------------|----------------------|----------------------|
| 10 | 0.8 | 25.6 | 8.3 | 10.3 | 38.7 |
| 15 | 0.8 | 26.7 | 15.5 | 17.6 | 37.3 |
| 20 | 0.8 | 24.4 | 17.8 | 21.1 | 25.9 |
| 25 | 0.8 | 26.3 | 23.2 | 26 | 29.7 |
| 30 | 0.8 | 26.5 | 26.7 | 29.5 | 29.7 |

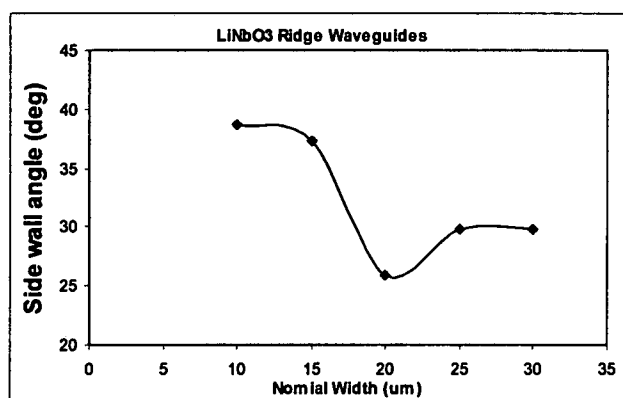


Figure 6.11: The sidewall angle as a function of the nominal width of etched LiNbO_3 ridge waveguides.

6.4 Conclusions

The etch rates of lithium niobate in all three cuts etched by CHF_3 , SF_6 and CF_4 were investigated. At a zero or a low bias power, the net polymer deposition instead of the net etching was found in CHF_3 plasma at 15 mTorr for all of three x-, y- and z-cuts. No polymer deposition was tested in CF_4 and SF_6 plasma at zero bias power, an operating pressure of 5 mTorr and 400W ICP source power. CHF_3 was chosen to etch lithium niobate gratings and LiNbO_3 ridge waveguides. A maximum etch rate of 50 nm/min was obtained in CHF_3 plasma for the LiNbO_3 gratings. An etched depth of 2.4 μm and a sidewall of 81° were achieved for 40 minutes etching.

CHAPTER VII

EXPERIMENTAL DESIGN AND MODELS

7.1 Experimental Design

The etch rate, sidewall profile are influenced by process parameters such as RIE bias power, operating pressure, etching time and ICP source power. In order to achieve excellent and required etching result and low cost, parameters must be optimized to meet a specific requirement. The experiment design is developed. RIE power, ICP power, pressure and etching time are independent variables. The etch rate and sidewall angle are the responses. The models were subsequently used to optimize the etching process. A statistical experimental design was chosen to give process response Y as main effect variables X_i and their interaction terms $X_i X_j$ with n variables in a factorial model:

$$Y = A_0 + \sum_{i=1}^n A_i X_i + \sum_{i=1}^n \sum_{j=1}^n A_{ij} X_i X_j \quad (7-1)$$

The coefficients in equation (7-1) were determined using an analysis-of-variance model in the SAS system. The SAS output from PROC GLM was analyzed.

7.2 Silicon Etch Rate

The predicted etch rate as functions of RIE power, ICP power, operation pressure and etching time for micro-optics structures etched in ICP with 25 sccm CHF₃ is

$$ER = A_0 + A_1 X_{RIE} + A_2 X_P + A_{12} X_{RIE} X_P + A_3 X_{ICP} + A_{13} X_{RIE} X_{ICP} + A_{23} X_P X_{ICP} + A_4 X_t + A_{14} X_{RIE} X_t + A_{24} X_P X_t + A_{34} X_{ICP} X_t \quad (7-2)$$

where X_{ICP} is ICP power, X_{RIE} is RIE power, X_P is operating pressure, and X_t is etching time. The coefficients in equation (7-2) are listed in table 7-1.

Table 7.1: The coefficients of the equation (7-2).

| Parameter | Estimate | Standard Error | t Value | Pr > t |
|-----------|--------------|----------------|---------|---------|
| A_0 | 0.039584706 | 0.083686 | 0.47 | 0.6383 |
| A_1 | 0.0022797 | 0.000835 | 2.73 | 0.0088 |
| A_2 | -0.010108968 | 0.004756 | -2.13 | 0.0386 |
| A_{12} | -0.000041341 | 2.09E-05 | -1.98 | 0.0533 |
| A_3 | 0.000106581 | 0.000163 | 0.65 | 0.5168 |
| A_{13} | -0.000001967 | 1.97E-06 | -1 | 0.3238 |
| A_{23} | 1.54142E-05 | 5.69E-06 | 2.71 | 0.0093 |
| A_4 | -0.001291884 | 0.001189 | -1.09 | 0.2825 |
| A_{14} | -3.1798E-06 | 5.53E-06 | -0.57 | 0.5682 |
| A_{24} | 7.58087E-05 | 3.08E-05 | 2.46 | 0.0175 |
| A_{34} | 7.828E-07 | 1.01E-06 | 0.77 | 0.4429 |

From Figure 7.1, the etch rate increases with the increase of RIE power and the decrease of operating pressure.

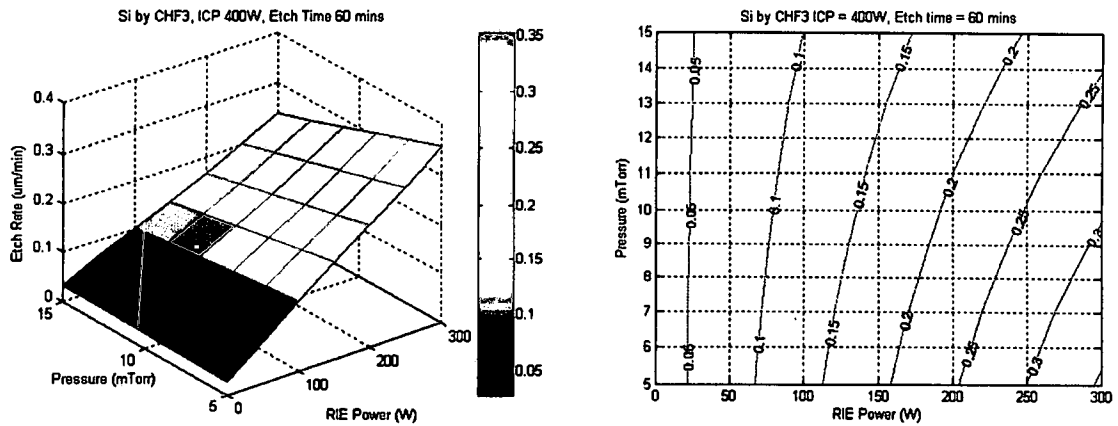


Figure 7.1: The predicted etch rate as functions of RIE power and operating pressure
(a) 3D and (b) contour plot.

7.3 The Sidewall Angle

The predicted angle as functions of RIE power, ICP power, operation pressure and etching time for micro-optics structures etched in ICP with 25 sccm CHF₃ is

$$\begin{aligned} \text{Angle} = & A_0 + A_1 X_{\text{RIE}} + A_2 X_p + A_{12} X_{\text{RIE}} X_p + A_3 X_{\text{ICP}} + A_{13} X_{\text{RIE}} X_{\text{ICP}} + A_{23} X_p X_{\text{ICP}} + \\ & A_4 X_t + A_{14} X_{\text{RIE}} X_t + A_{24} X_p X_t + A_{34} X_{\text{ICP}} X_t \end{aligned} \quad (7-3)$$

The coefficients in equation (7-3) are listed in table 7-2.

Table 7.2: The coefficients of the equation (7-3).

| Parameter | Estimate | Standard Error | t Value | Pr > t |
|-----------------|-------------|----------------|---------|---------|
| A ₀ | 90.60269092 | 14.99958 | 6.04 | <.0001 |
| A ₁ | -0.05984682 | 0.149715 | -0.4 | 0.6911 |
| A ₂ | -0.15316651 | 0.852417 | -0.18 | 0.8581 |
| A ₁₂ | 0.00025944 | 0.003742 | 0.07 | 0.945 |
| A ₃ | -0.01823454 | 0.029255 | -0.62 | 0.536 |
| A ₁₃ | 0.00019776 | 0.000354 | 0.56 | 0.5787 |
| A ₂₃ | -0.00121396 | 0.00102 | -1.19 | 0.2397 |
| A ₄ | -0.16752051 | 0.213108 | -0.79 | 0.4356 |
| A ₁₄ | -0.00010874 | 0.000992 | -0.11 | 0.9132 |
| A ₂₄ | 0.00899184 | 0.005524 | 1.63 | 0.11 |
| A ₃₄ | 0.00022562 | 0.000181 | 1.24 | 0.2194 |

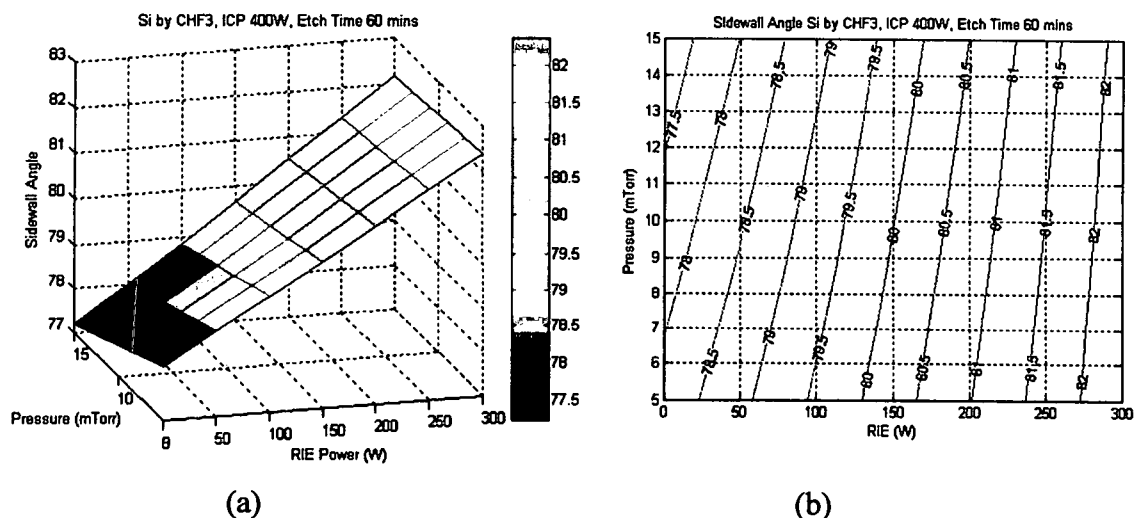


Figure 7.2: The predicted sidewall angle as functions of RIE power and operating pressure (a) 3D and (b) contour plot.

The sidewall angle increases with RIE power while the ICP power is fixed at 400W and the etching time is 60 minutes. The change of sidewall is less than a degree as the operating pressure increases from 5 to 15 mTorr. The sidewall angle is stable over a long etching time and it is not significantly affected by pressure.

Figure 7.3 is contour plots of the sidewall angles as functions of the RIE power and the operation pressure while the ICP power is fixed at 400W, the operating pressure is (a) 15 mTorr and (b) 5 mTorr. The sidewall angle increases with RIE power at 15 mTorr, the etch rate increases with the RIE power, but it is constant with the etching time. The sidewall angle increases with RIE power and the etching time. The etch rate increases with RIE power, but decreases with the etching time at 5 mTorr. The sidewall angle increases with etching time, but decreases with etching time at 5 mTorr. At a lower pressure, the fluorine radicals become deficiency to reach to the bottom of the trench as the etched depth increases, therefore the etch rate decreases, less polymer film is removed, and therefore produces a small sidewall angle.

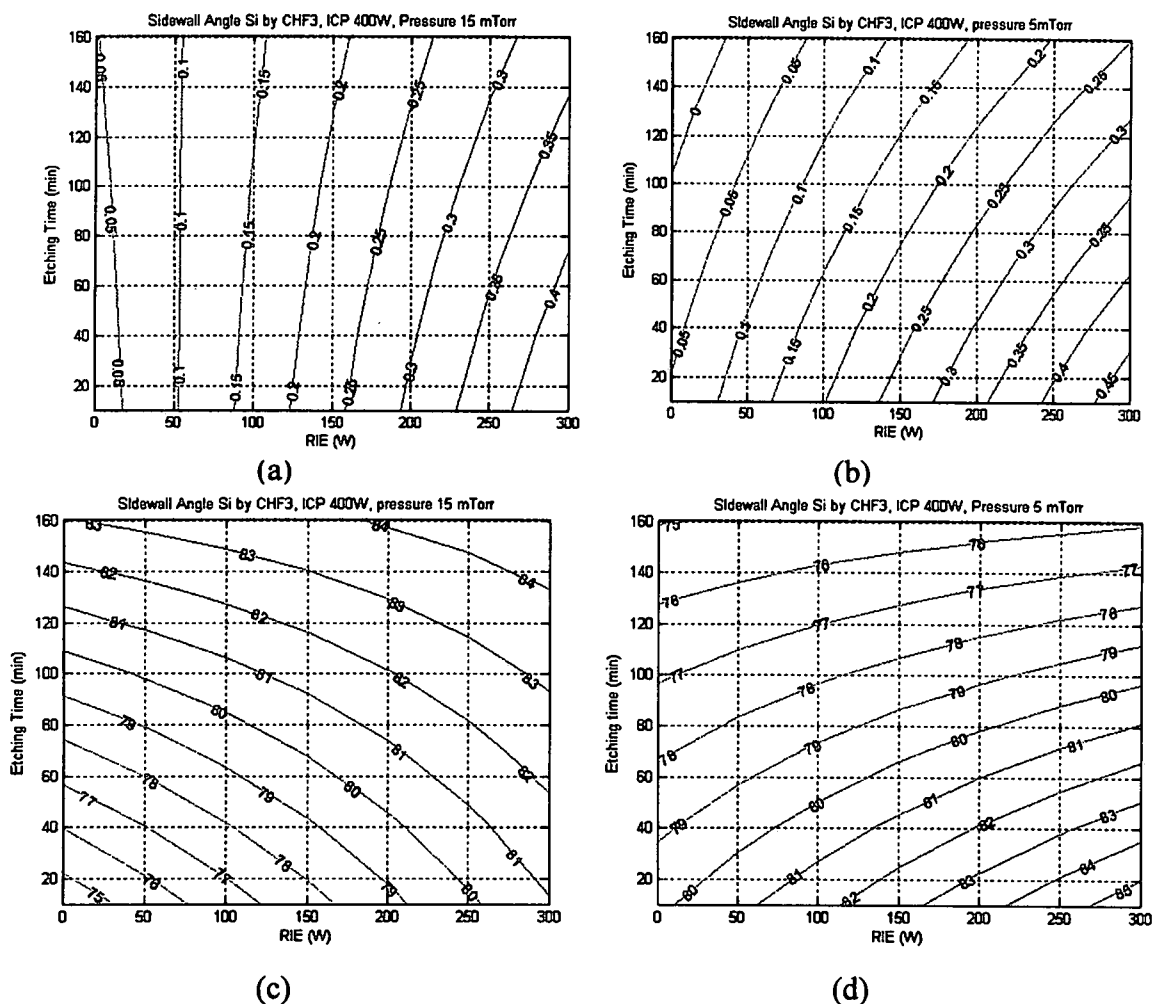


Figure 7.3: The contour plots of the predicted etch rate (a) 15 mTorr and (b) 5 mTorr and the sidewall angle (c) 15 mTorr and (d) 5mTorr as functions of RIE power and etching time.

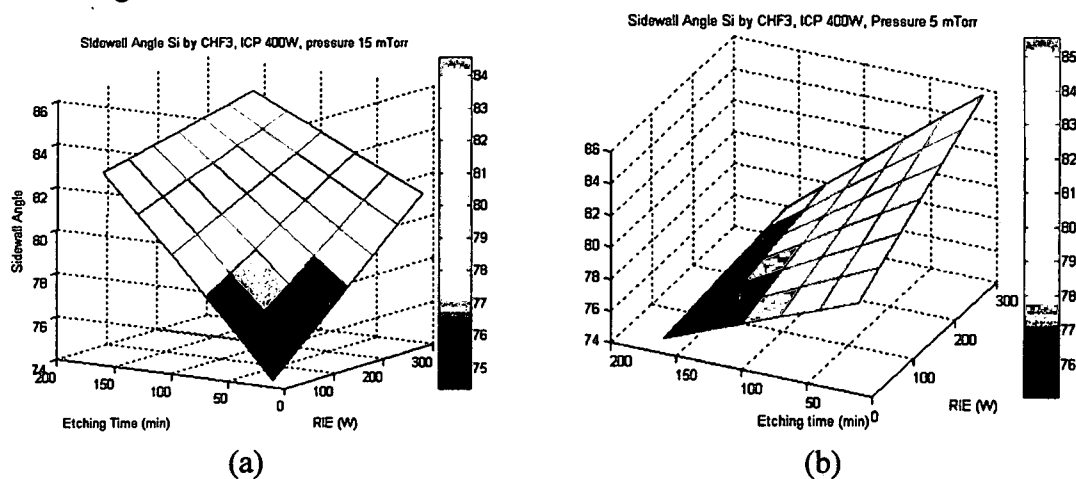


Figure 7.4: The 3D plot of the predicted sidewall angle as functions of RIE power and etching time (a) 15mTorr and (b) 5mTorr.

7.4 Conclusion

The etch rate and angle of tapered sidewall of micro-optics structure have been predicted with an analysis-of-variance model in the SAS system. A statistical experimental design is developed with independent processing parameters such as RIE power, gas pressure, ICP power and etching time. This work has demonstrated that the optimum etching process can be used for a specific processing requirement and future fabrications of a variety of devices.

CHAPTER VIII

CONCLUSIONS

The purpose of this thesis is to develop a process of sidewall profile control using low pressure high density ICP technique in fluorocarbon plasma. The V-grooved micro-optics waveguides up to 80 degree on the focal plane array detectors were realized. The etch rates of silicon, silicon dioxide and lithium niobate in SF_6 , CF_4 and CHF_3 plasma were fully investigated. The sidewall profiles of silicon micro-optics structures and lithium niobate gratings were examined and characterized with SEM, AFM and WLI. The model of experiment design was constructed for optimizing processes.

In the future, applying the experimental design model is capable to fabricate the desired depth and sidewall profile of micro and nano-optical waveguides, imprinting mold fabrication, micro fluidic and MOEMS devices.

APPENDIX

CHARACTERIZATION TECHNIQUES

In this appendix, several important characterization techniques used in this thesis will be discussed. The following is a list of important tools which are used to measure the etched depth and sidewall profile.

A.1 Stylus Interferometer

Ambios XP Series Stylus profiler was used to measure the thickness of masks and the etched depth. The Ambios Technology, Inc. XP Stylus Profiler is a computerized, high-sensitivity surface profiler that measures roughness, waviness, and step height in a variety of applications. The profiler incorporates a new optical deflection height measurement mechanism and magneto static force control system which results in a low force (loads as small as .05 mg) and low inertia stylus assembly, making it the most innovative bench top profiler on the market today. It is capable to measure precision step heights from under 10 angstroms to as large as 100 microns. The XP profiler provides an affordable, high-resolution surface measurement capability that nicely complements other analytical instruments. This is a fast and simple method to measure the step height. But it is limited to measure high aspect ratio trench and to give an accurate sidewall profile due to the needle size.

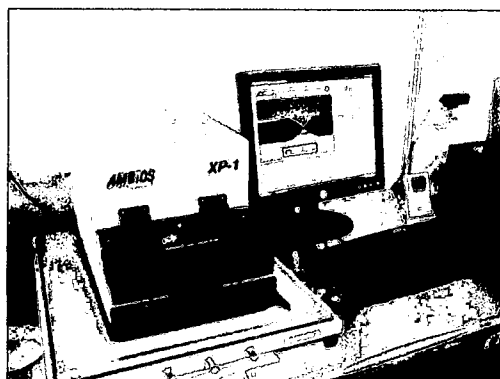


Figure A.1: Ambios Stylus interferometer

A.2 High Resolution Scanning Electron Microscope

The SEM is a dispensable characterization tool in many modern technology fields. The Hitachi S-4800 HRSEM Secondary electrons (SE) and back scattered electrons (BSE) are generated by interaction between the electron beam and specimen. The SEM scans a sample with a beam of electrons that interact with the sample. Some of those electrons generated during this process escape from the sample and reach a detector. The number of electrons that reach the detector at each point on the sample depends on the topology of the sample and the atomic weight of the atoms at the surface, and these variations in signal strength lead to image formation. The Hitachi S-4800 HRSEM can achieve an ultimate resolution of 1.0 nm at 15 kV and 2.0nm at 1KV.

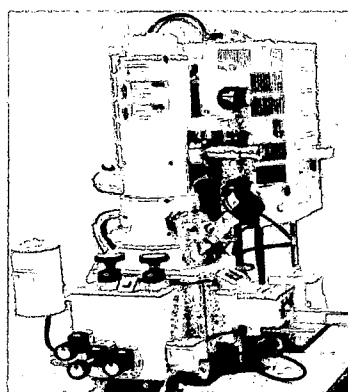


Figure A.2: The Hitachi S-4800 HRSEM

A.3 Atomic Force Microscope

The AFM consists of a microscale cantilever with a sharp tip at its end that is used to scan the specimen surface. When the tip is brought into proximity of a sample surface, forces between the tip and the sample lead to a deflection of the cantilever according to Hooke's law. The deflection is measured using a laser spot reflected from the top surface of the cantilever into an array of photodiodes.

The Park System NSOM offers a complete AFM system setup with unprecedented adaptability for these optical experiments. The high-performance Z-servo scanner of the XE-NSOM supports True Non-Contact AFM and utilizes cantilever-based closed-loop feedback technology. The AFM of NSOM was used for scanning the etched gratings of lithium niobate.

A disadvantage of AFM compared with the SEM is the image size. The SEM can image an area on the order of mm by mm with a depth of field on the order of millimeters. The AFM can only image a maximum height on the order of micrometers and a maximum scanning area of around 100 by 100 micrometers. Another inconvenience is that an incorrect choice of tip for the required resolution can lead to image artifacts. The scan of AFM is relatively slow.

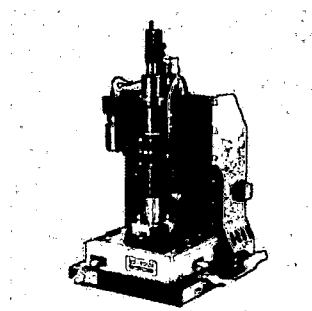


Figure A.3: Park System NSOM

A.4 White Light Interferometer

Veeco Wyko NT9100 White light interferometer is an extremely powerful measurement tool of combining white light interferometer techniques with modern electronics, computers, and software to produce a topographical image of the sample. One advantage of using the white light interferometer is that the sample will not be damaged as it is by cleaving for a cross-sectional SEM image. Another advantage is that it is very fast method to display images in all 3D, 2D cross-section, 2D and line profile for a single scan. It is suitable to measure the etched depth and profile of materials such as lithium niobate, which is hard to cleave and a special dice tool is needed to cut the sample for the cross-sectional SEM view. White light interferometer can measure conductive or dielectric material. The disadvantage is that it is difficult for characterization of undercut features or profile below overhang.

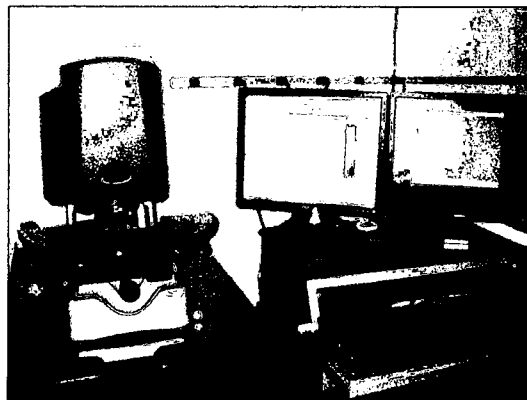


Figure A.4: Veeco Wyko NT9100 White Light Interferometer

BIBLIOGRAPHY

1. W. J. Park, J. H. Kim, S. M. Cho, S. G. Yoon, S. J. Suh and D. H. Yoon, "High aspect ratio via etching conditions for deep trench of silicon", *Surface & Coating Technology* 171 (2003) 290-295.
2. Stephen A. Campbell, "The Science and Engineering of Microelectronic Fabrication", 2nd edition, 2001.
3. Sami Franssila, "Introduction To Micro Fabrication", 2004.
4. G. Oehrlein, Y. Zhang, D. Vender and O. Joubert, "Fluorocarbon high-density plasmas. II. Silicon dioxide and silicon etching using CF_4 and CHF_3 ", *J. Vac. Sci. Technol.*, A12, 333 (1994).
5. F.G. Celii, Q. He, H. -Y. Liu and J. R. DeBord, "Process Characterization for tapered contact etch", *J. Vac. Sci. Technol. B*19, 1845 (2001).
6. K. Nakamura, M. ohwaki, S. Yoneda and H. Sugai, "Alternating ion bombardment technique for wall surface control in depositive plasma processing", *J. Vac. Sci. Technol. A*18, 137 (2000).
7. K. Richter, M. Orfert, S. Howitz and S. Thierbach, "Deep Plasma Silicon etch for microfluidic applications" *Surface And Coatings Technology* 116-119 (1999), pg. 461-467.

8. D. Weston, W. J. Dauksher, D. Rhine and T. Smeka "Plasma Etched Micromachined Silicon Stampers for plastic Biotechnology applications", Motorola Labs, Physical Sciences Research.
9. J. Devitt, R. Rawe, M. Garter, D. Endres, M. Davis, C. Martin, B. Fischer, M. Garter, A. Sarangan and L. Sun, "Micro-optic waveguides on IRFPA's with reticulated pixels for 100% fill factor", 2005 MSS conference 2005.
10. B. Jacobs and R. Zengerle, "Reactive ion etching of sloped sidewalls for surface emitting structures using a shadow mask technique", J. Vac. Sci. Technol. B14, 2537 (1996).
11. Tzyy-Jiann Wang, Chih-Feng Huang, Way-Seen Wang, and Pei-Kuen Wei, "A Novel Wet-Etching Method Using Electric-Field-Assisted Proton Exchange in LiNbO_3 ", J. Lightwave Technol. Vol. 22, 1764 (2004).
12. H. Hu, R. Ricken, W. Sohler and R. B. Wehrspohn, "Lithium niobate ridge waveguides fabricated by wet etching", IEEE Photonics Technology Letters, Vol.19 (2007), pp.417-419.
13. V. Joshkin, K. Dovidenko, S. Oktyabrsky, D. Saulys, T. Kuech and L. McCaughan, "New methods for fabricating patterned lithium niobate for photonic applications", Journal of Crystal Growth 259 (2003) 273–278.
14. H. Hu, A. P. Milenin, R. B. Wehrspohn, H. Hermann, and W. Sohler, "Plasma etching of proton-exchanged lithium niobate", J. Vac. Sci. Technol. A24, 1012 (2006).
15. B. Schwartz and H. Robbins, "Chemical Etching of Silicon: Etching Technology," J. Electrochem. Soc. 123 1903 (1976).

16. M. Nold, S. Kleditzsch and U. Riedel, "Modeling inductively coupled plasmas: a sensitivity study on plasma chemistry and surface chemistry", *Surface & Coatings Technology* 142, 531-535 (2001).
17. M. V. Bazylenko and M. Gross, "Reactive ion etching of silica structures for integrated optics applications", *J. Vac. Sci. Technol. A* 14, 2994-3003 (1996).
18. Dennis M. Manos and Daniel L. Flemm, "Plasma Etching An Introduction", (Academic, New York, 1989).
19. F. Gaboriau, M-C. Fernandez-Peignon, G. Carty and C. Cardinaud, "Etching Mechanisms of Si and SiO₂ in inductively Coupled Fluorocarbon plasmas: correlation between plasma species and surface etching", *J. Vac. Sci. Technol. A* 23, 226 (2005).
20. D. Zhang, S. Rauf, T. Sparks and P. Ventzek, "Integrated equipment-feature modeling investigation of fluorocarbon plasma etching of SiO₂ and photoresist", *J. Vac. Sci. Technol. B* 21 828 (2003).
21. I. Amirov, M. Izyumov and O. Morozov, "Etching of Silicon and Silicon Dioxide in Dense Low-Pressure Inductively Coupled Radiofrequency Discharge Fluorocarbon Plasmas", *High Energy Chemistry*, vol. 37, No. 5, 328-332 (2003).
22. A. Burtsev, Y.X. Li , H.W. Zeijl , C.I.M. Beenakker, "Anisotropic U-shaped SF₆-based plasma silicon trench etching investigation", *Microelectronic Engineering* 40 (1998) 85-97.
23. G. S. Oehrlein, Y. Zhang, D. Vender and M. Haverlag, "Fluorocarbon high density plasmas. I. Fluorocarbon film deposition and etching using CF₄ and CHF₃", *J. Vac. Sci. Technol. A* 12, 323 (1994).

24. G. Oehrlein, Y. Zhang, D. Vender and O. Joubert, "Fluorocarbon high-density plasmas. II. Silicon dioxide and silicon etching using CF_4 and CHF_3 ", J. Vac. Sci. Technol., A12, 333 (1994).
25. G. Oehrlein and Y. Kurogi, "Sidewall surface chemistry in directional etching processes", Mat. Sci. and Eng., vol. 24, 152 (1998).
26. M. Bazylenko and M. Gross, "Reactive Ion Etching of Silica Structures for Integrated Optics Applications", J. Vac. Sci. Technol. A 14, 2994 (1996).
27. K. Richter, M. Orfert, S. Howitz and S. Thierbach, "Deep Plasma Silicon etch for microfluidic applications" Surface And Coatings Technology 116-119 (1999), pg. 461-467.
28. K. Richter, "Variation of etch profile and surface properties during patterning of silicon substrates".
29. O. Kwon, B. Bai and H. Sawin, "Surface kinetic modeling of silicon and silicon oxide plasma etching, II Plasma etching surface kinetics modeling using translating mixed-layer representation", J. Vac. Sci. Technol. A 24, 1920 (2006).
30. D. Zhang, S. Rauf, T. Sparks and P. Ventzek, "Integrated equipment-feature modeling investigation of fluorocarbon plasma etching of SiO_2 and photoresist", J. Vac. Sci. Technol. B21, 828 (2003).
31. H. Sugai and K. Nakamura, "Diagnostic and control of radicals in an inductively coupled etching reactor", J. Vac. Sci. Technol. A13, 887 (1995).
32. E. Gogolides and P. Vauvert, "Etching of SiO_2 and Si in fluorocarbon plasmas: A detailed surface model accounting for etching and deposition", J. Appl. Phys. 88, 5570 (2000).

33. G. Kokkoris, "Etching of SiO₂ features in fluorocarbon plasmas: Explanation and predication of gas-phase-composition effects on aspect ratio dependent phenomena in trenches", J. Appl. Phys. 91, 2697 (2002).
34. M. Schaepkens and G. Oehrlein, "A review of SiO₂ etching studies in inductively coupled fluorocarbon plasmas", J. ElectroChemical Soc. 148, C211-C221 (2001).
35. Byungwhan Kim and Kunho Kim, "Prediction of profile roughness in CHF₃/CF₄ plasma using neutral network", Applied Surface Science 222 (2004) 17-22.
36. Douglas C. Montgomery, "Design and analysis of experiments", 6th edition, 2005.
37. D. L. Flemm, V. M. Donnelly, and J. A. Mucha, J. Appl. Phys. 52, 3633 (1981).
38. M. Kojima, H. Kato, and M. GaMorinaga, J. Appl. Phys. 70, 2901 (1991).
39. T. Standaert, M. Schaepkens, N. Rueger, P. Sebel, G. S. Oehrlein and J. M. Cook, "High density fluorocarbon etching of silicon in an inductively coupled plasma: mechanism of etching through a thick steady state fluorocarbon layer", J. Vac. Sci. Technol. A 16(1), 239 (1998).
40. J. Ding and N. Hershkowitz, "Symmetric rate model for fluorocarbon plasma etching of SiO₂", Appl. Phys. Lett. 68, 1619 (1996).
41. M. Schaepkens, R. Bosch, T Stadaert and G. Oehrlein, "Influence of reactor wall conditions on etch processes in inductively coupled fluorocarbon plasmas", J. Vac. Sci. technol. A 16, 2099 (1998).
42. K. Takahashi, M. Hori and Toshio Goto, "Fluorocarbon radicals and surface reactions in fluorocarbon high density etching plasma. I. O₂ addition to electron cyclotron resonance plasma employing CHF₃", J. Vac. Sci. Technol. A 14, 2004 (1996).

43. Y. Chinzei and T. Ichiki, "Residence time effects on SiO₂/Si selective etching employing high-density fluorocarbon plasma", J. Vac. Sci. Technol. B16, 1043 (1998).
44. P. Riley and D. Hanson, "Comparison of etch rates of silicon nitride, silicon dioxide, and polycrystalline silicon upon O₂ dilution of CF₄ plasmas", J. Vac. Sci. Technol. B7, 1352 (1989).
45. D. Humbird and D. Graves, "Mechanism of silicon etching in the presence of CF₂, F, and Ar⁺", J. Appl. Phys., vol. 96, 2466 (2004).
46. D. Humbird and D. Graves, "Atomistic simulations of spontaneous etching of silicon by fluorine and chlorine", Appl. Phys., vol. 96, 791 (2004).
47. O. Kwon and H. Sawin, "Surface kinetics modeling of silicon and silicon oxide plasma etching. I. Effect of neutral and ion fluxes on etching yield of silicon oxide in fluorocarbon plasmas", J. Vac. Sci. Technol. A24, 1906 (2006).
48. O. Kwon and Sawin, "Surface kinetics modeling of silicon and silicon oxide plasma etching. III", J. Vac. Sci. Technol. A24 (2006).
49. A. Sarangan, "Unaxis Shuttleline",
<http://homepages.udayton.edu/~sarangam/nanofab/>>
50. Wikipedia, September 9, 2007, "Turbomolecular Pump",
<http://en.wikipedia.org/wiki/Turbomolecular_pump>
51. Meng Lieh Sheu, Mon Chau Shie, Tai Ping Sun, Far Wen Jih, "A Cross-Check Test Scheme for Infrared Focal Plane Array", FPA2C-3.pdf
52. Rohm & Hass Megaposit SPR955-CM Datasheet

53. MicroChem LOR Datasheet.
54. Naoki Mitsugi and Hirotoshi Nagata, "Challenges in electron cyclotron resonance plasma etching of LiNbO_3 surface for fabrication of ridge optical waveguides", J. Vac. Sci. Technol. A16, 2245 (1998).
55. Sarah Benchabane, Laurent Robert, Jean-Yves Rauch, Abdelkrim Khelif, and Vicent Laude, "Highly selective electroplated nickel mask for lithium niobate dry etching", J. Appl. Phys. 105, 094109 (2009)

VITA

- 1982 B.A., Northwest Telecommunication Engineering Institute
 Xian, China
- 1990 M.S., University of New Mexico
 Albuquerque, New Mexico
- 2009 Ph.D., University of Dayton
 Dayton, Ohio

PUBLICATIONS

Lirong Sun and Andrew M. Sarangan, "ICP Etching Lithium Niobate", submit to Journal of Micro/Nanolithography, MEMS, and MOEMS.

Lirong Sun and Andrew M. Sarangan, "Controlling Sidewall Angles by Inductively Coupled Plasma Etching for Silicon Micro-Optic Structures", submit to Journal of Micro/Nanolithography, MEMS, and MOEMS.

FIELDS OF STUDY

Major Field: Micro and Nano Fabrication

Studies of Inductively Coupled Plasma Etching, Professor Andrew M. Sarangan.

R702035601